

PACIFIC EARTHQUAKE ENGINEERING RESEARCH CENTER

Three-Dimensional Beam-Truss Model for Reinforced-Concrete Walls and Slabs Subjected to Cyclic Static or Dynamic Loading

Yuan Lu

Marios Panagiotou

Department of Civil and Environmental Engineering
University of California, Berkeley

Ioannis Koutromanos

Department of Civil and Environmental Engineering
Virginia Polytechnic Institute and State University

PEER Report 2014/18

Pacific Earthquake Engineering Research Center
Headquarters at the University of California, Berkeley

December 2014

Disclaimer

The opinions, findings, and conclusions or recommendations expressed in this publication are those of the author(s) and do not necessarily reflect the views of the study sponsor(s) or the Pacific Earthquake Engineering Research Center.

Three-Dimensional Beam-Truss Model for Reinforced-Concrete Walls and Slabs Subjected to Cyclic Static or Dynamic Loading

Yuan Lu

Marios Panagiotou

Department of Civil and Environmental Engineering
University of California, Berkeley

Ioannis Koutromanos

Department of Civil and Environmental Engineering
Virginia Polytechnic Institute and State University

PEER Report 2014/18
Pacific Earthquake Engineering Research Center
Headquarters at the University of California, Berkeley

December 2014

ABSTRACT

The three-dimensional (3D) beam-truss model (BTM) for reinforced concrete (RC) walls, which was developed by the first two authors in a previously published paper, is modified to better represent flexure-shear interaction and more accurately compute diagonal shear failures under static cyclic or dynamic loading. The modifications pertain to the element formulations and the determination of the inclination angle of the diagonal elements. Moreover the BTM is extended to allow the simulation of RC slabs. The modified BTM is validated using the experimental test data of eight RC walls subjected to static cyclic loading, including two non-planar RC walls under multi-axial cyclic loading, a slab specimen, and a 5-story non-planar RC coupled wall-slab specimen under triaxial dynamic base excitation. Six of the walls considered experienced diagonal shear failure after reaching their flexural strength, while the other two walls had a flexural dominated response. The numerically computed lateral force-lateral displacement and strain contours are compared to the experimental recorded response and damage state for each of the walls. The effects of different model parameters on the computed results are examined by means of parameteric analyses.

ACKNOWLEDGMENTS

The authors would like to thank Mohammadreza Moharrami for his help with Open2GiD – the ability to plot strain contours and deflected shapes of Opensees models has been invaluable.

Publication of this report was funded by the Pacific Earthquake Engineering Research Center (PEER). Any opinions, findings, and conclusions or recommendations expressed in this material are those of the authors, and do not necessarily reflect those of PEER.

CONTENTS

ABSTRACT	iii
ACKNOWLEDGMENTS	v
TABLE OF CONTENTS	vii
LIST OF TABLES	ix
LIST OF FIGURES	xi
1 INTRODUCTION	1
1.1 Literature Review	3
2 BEAM-TRUSS MODELING APPROACH	5
2.1 Overview	5
2.2 Material Models	7
2.3 Biaxial Concrete Compressive Stress Reduction Factor and the Calculation of Normal Tensile Strain	8
2.4 Determination of Inclination Angle for Diagonal Elements	9
2.4.1 Walls Uniform over their Height	10
2.4.2 Coupled Walls.....	11
2.5 Modeling of Tension for Concrete in the Horizontal Direction	12
2.6 Nonlinear Analysis Program	13
3 VALIDATION FOR STATIC LOADING	15
3.1 Specimen Overview and BTM Results	15
3.2 Effect of In-Plane Flexural Resistance of Vertical Lines	25
3.3 Effect of Concrete Tension in Horizontal Elements	26
3.4 Effect of Inclination Angle of Diagonal Elements	27
3.5 Modeling of Large Boundary Elements	29
4 BEAM-TRUSS MODEL FOR SLABS	33
5 VALIDATION FOR A 5-STORY COUPLED WALL SUBJECTED TO TRI-AXIAL BASE EXCITATIONS	37
5.1 Specimen Overview	37
5.2 Determination of Beam-Truss Model for Specimen SLO	40

5.3	BTM Results	42
5.4	Effect of Coupling	46
5.5	Effect of Concrete Tensile Strength with Horizontal Elements.....	48
5.6	Effect of Mesh Refinement.....	49
5.7	Effect of Bar Fracture	52
6	CONCLUSIONS	57
	REFERENCES.....	59
APPENDIX A	COMPUTED STRAIN CONTOURS AND DEFLECTED SHAPES FOR CASE STUDIES WITH STATIC LOADING	61

LIST OF TABLES

Table 1.1	Nonlinear finite element studies that computed shear or out-of-plane failure for RC wall specimens.....	4
Table 3.1	Characteristics of eight experimentally tested specimens and beam-truss model parameters.....	20
Table 5.1	Experimentally recorded and numerically computed periods of translational modes for 5-story specimen SLO.....	44

LIST OF FIGURES

Figure 1.1	Photographs of diagonal tension and compression failures taken after major earthquake events: (a) M6.8 1995 Kobe, Japan earthquake (from Maffei and Yuen [2007]); (b-c) M6.3 2009 L’Aquila, Italy earthquake (from Dazio [2009b]); and (d) M8.8 2010 Chile earthquake (courtesy of J. Restrepo).	2
Figure 2.1	Schematic description of the beam-truss model approach for a T-shaped section wall.	6
Figure 2.2	Uniaxial stress-strain laws for the (a) concrete and (b) steel material models.	8
Figure 2.3	(a) Concrete compressive strength reduction factor, as proposed in Vecchio and Collins [1986], compared to the trilinear relation used in this report for an element length of 600 mm; and (b) schematic of normal strain calculation for one of the diagonal trusses of the 4-node rectangular element.	9
Figure 2.4	Schematics including coupling forces for a coupled wall.	12
Figure 3.1	Experimentally measured and numerical computed force-drift ratio response for specimens (a) Unit 1.0, (b) Unit 2.0; (c) WSH6; (d) B6; (e) F1; and (f) TW2.	21
Figure 3.2	Numerically computed strain contour and deformed shape for specimens (a) Unit 1, (b) F1, and (c) TUB (E-W segment) at the point of first diagonal crushing compared to the damage state of the experimental specimen at the end of each test.	22
Figure 3.3	Experimentally measured and numerical computed force-drift ratio response for specimen NTW1 in the N-S, E-W, and skew cycles.	23
Figure 3.4	Experimentally measured and numerical computed force-drift ratio response for specimen TUB.	24
Figure 3.5	Experimentally measured and numerically computed lateral force-displacement response for specimens (a) Unit 1.0, (b) Unit 2.0, and (c) WSH6 with in-plane flexural rigidity in all vertical lines of the BTM.	25
Figure 3.6	Experimentally measured and numerically computed lateral force-displacement response for specimens (a) Unit 1.0, (b) Unit 2.0, and (c) WSH6 with truss model (zero in-plane flexural resistance in all vertical elements).	26
Figure 3.7	Numerically computed lateral force-displacement response for specimens (a) Unit 1.0, (b) F1, and (c) TW2 with BTM-HT that includes the horizontal concrete tension resistance and aggregate interlock model as defined in Moharrami et al. [2014] compared to experimentally measured results.	27

Figure 3.8	Photos of specimen Unit 2.0 (from Mestyaneck [1986]) with annotations to show angle of compression struts.	28
Figure 3.9	Experimentally measured and numerically computed lateral force-displacement response for specimen Unit 2.0 with diagonal angle equal to (a) 64.4°, (b) 56°, and (c) 44.4°.	29
Figure 3.10	Numerically computed strain contour and deformed shape (magnification factor = 5) at -1.92% drift for specimen Unit 2.0 with diagonal angle equal to (a) 64.4°, (b) 56°, and (c) 44.4°.	29
Figure 3.11	Elevation and cross-section views of two methods for modeling specimen B6: (a) average properties and (b) rigid offsets.	31
Figure 3.12	Experimentally measured and numerically computed lateral force-displacement response for specimen B6 modeled with (a) without considering the width of the boundary elements; (b) with average properties for the width of the boundary elements; and (c) with rigid offsets of the boundary elements.	31
Figure 3.13	Numerically computed strain contour and deformed shape (magnification factor = 5) at the second cycle of 1.7% drift for specimen B6 modeled with (a) BTM-web, (b) BTM-avg, and (c) BTM-off, compared to (d) the experimental failure mode at the end of the test.	32
Figure 4.1	(a) Three-dimensional view and dimensions of the column-slab specimen 2C [Robertson 1990] and (b) the corresponding BTM for the specimen.	34
Figure 4.2	Experimentally measured and numerically computed lateral force-displacement response for column-slab specimen 2C with (a) perfect bond and (b) strain penetration modeled at the column-slab interface.	35
Figure 4.3	Hysteretic behavior of bond slip material including pinching.	35
Figure 5.1	Description of 5-story coupled wall specimen SLO and beam-truss model.	38
Figure 5.2	Recorded acceleration time history of the shaking table in the three directions during ground motion T6.	39
Figure 5.3	Damage pattern of the bottom floor (a) web and (b) coupling beam (viewed from the negative x direction) and (c) flange in the negative y direction after ground motion T6 (from Coelho et al. [2006]).	40
Figure 5.4	(a) Coupling beam forces on the walls and resulting reaction at the base for roof drift in the negative y direction; (b) strut-and-tie model for coupled wall of specimen SLO showing the predicted load path for lateral load in the y-direction; and (c) resulting beam-truss model for the coupled wall accounting for geometric constraints.	42
Figure 5.5	Statically imposed displacement history (normalized to peak displacement) used to simulate damage from ground motions T1 to T5.	43
Figure 5.6	Experimentally measured and numerically computed base shear force and roof drift response histories for ground motion T6.	44

Figure 5.7	Experimentally measured and numerically computed base shear versus roof drift response hysteretic shapes during ground motion T6.	45
Figure 5.8	Numerically computed strain contour at $t = 3.3$ sec (a) global view and (b) zoom at the web of the bottom story (magnification factor = 10).	45
Figure 5.9	Response history of (a) shear force and (b) axial force resisted by the coupling beams and slabs at the interface with Wall A.	47
Figure 5.10	(a) Response history of normalized base shear force and (b) normalized base shear force versus roof drift ratio for the two T-section walls, as defined in Figure 5.1(a).	47
Figure 5.11	(a) Response history of axial load variation and (b) axial load variation versus roof drift ratio for the two T-section walls, as defined in Figure 5.1(a).	47
Figure 5.12	Experimentally measured and numerically computed base shear force and roof drift response histories of BTM-HT during ground motion T6.	49
Figure 5.13	BTM with mesh refinement in the bottom story (BTM-fineMesh); the additional elements of BTM-fineMesh are shown in orange over the original BTM mesh (shown in black).	50
Figure 5.14	Experimentally measured and numerically computed response time histories during ground motion T6 using BTM-fineMesh (BTM with mesh refinement in the bottom story).	51
Figure 5.15	Numerically computed strain contour at $t = 3.3$ sec (a) global view and (b) zoom at the web of the bottom story for BTM-fineMesh (BTM with mesh refinement in the bottom story).	52
Figure 5.16	Uniaxial stress-strain behavior for the steel material model including the effect of rupture.	53
Figure 5.17	Experimentally measured and numerically computed response time histories for ground motion T6 using BTM-fineFrac (BTM with mesh refinement and bar fracture).	54
Figure 5.18	(a) Global view and (b) zoom at the web of the bottom story of the computed strain contour immediately before diagonal crushing and bar fracture at $t = 3.29$ sec, and (c) zoom at the web of the bottom story after diagonal crushing and bar fracture at $t = 3.31$ sec (magnification factor = 10).	55
Figure A1.1	Strain contour and displaced shape (magnification factor = 10) for specimen Unit 1.0 at selected drift ratios. Triangular elements at the top of the wall model the loading beam.	63
Figure A1.2	Strain contour and displaced shape (magnification factor = 5) for specimen Unit 2.0 at selected drift ratios. Triangular elements at the top of the wall model the loading beam.	64
Figure A1.3	Strain contour and displaced shape (magnification factor = 5) for specimen WSH6 at selected drift ratios.	64

Figure A1.4	Strain contour and displaced shape (magnification factor = 5) for specimen B6 at selected drift ratios. Triangular elements at the top of the wall model the loading beam.....	65
Figure A1.5	Strain contour and displaced shape (magnification factor = 5) for specimen F1 at selected drift ratios.....	66
Figure A1.6	Strain contour and displaced shape (magnification factor = 5) for specimen TW2 at selected drift ratios.....	67
Figure A1.7	Strain contour and displaced shape (magnification factor = 5) for specimen NTW1 at selected drift ratios. Note: strain contours (a) through (e) are shown in the order which the specimen reaches each drift.....	68
Figure A1.8	Strain contour and displaced shape (magnification factor = 5) for specimen TUB at selected drift ratios.....	69

1 Introduction

Reinforced concrete (RC) structural walls are a common type of earthquake load-resisting systems. The computation of the nonlinear response, lateral load and displacement capacity, and failure mechanism of such structures is of primary importance for both practicing engineers and researchers. The computation of nonlinear response of RC walls is particularly challenging due to the effect of flexure-shear interaction (FSI) associated with multi-axial stress states that affect the behavior of concrete in compression. The challenge may increase in walls with non-planar cross sections, coupled with beams or slabs, or under multi-axial loading due to three-dimensional (3D) effects such as the non-uniform response and warping of wall segments perpendicular to the direction of loading (flanges). Experimental tests of RC wall specimens, (e.g., Oesterle et al. [1976]), have shown that the lateral load capacity and onset of strength degradation depend on the load history; thus, cyclic or dynamic loading is needed to fully investigate the behavior of RC walls under earthquake excitation.

Reinforced concrete walls designed according to modern seismic code provisions develop their flexural strength before they fail. Computation of the force-displacement behavior of RC walls including the response at and after initiation of failure is essential for seismic design and assessment. Common failure modes for RC walls include:

1. buckling and fracture of longitudinal steel bars;
2. loss of confinement due to rupture or loss of anchorage of confinement reinforcement and crushing of boundary elements in compression;
3. crushing of the web concrete in the diagonal direction including propagation of failure in vertical, horizontal, or diagonal direction after the initial diagonal strut fails (termed diagonal compression failure);
4. accumulation of significant horizontal strains over a narrow diagonal band that spans at least 50% of the length of the wall segment (termed diagonal tension failure);
5. formation of a horizontal sliding plane (termed shear sliding); and
6. out-of-plane global buckling of the wall section.

Diagonal failure modes (failure modes 3 and 4) are strongly related to FSI and may result in sudden losses of lateral load capacity; Figure 1.1 shows photographs of buildings with RC walls that experienced diagonal failures during earthquakes.



Figure 1.1 Photographs of diagonal tension and compression failures taken after major earthquake events: (a) M6.8 1995 Kobe, Japan earthquake (from Maffei and Yuen [2007]); (b-c) M6.3 2009 L'Aquila, Italy earthquake (from Dazio [2009b]); and (d) M8.8 2010 Chile earthquake (courtesy of J. Restrepo).

This report uses the beam-truss modeling approach developed in Lu and Panagiotou [2014] for RC walls to explicitly account for the effects of FSI under cyclic or dynamic loading. Compared to the beam-truss model (BTM) used in Lu and Panagiotou, this report proposes changes to the elements used in the BTM, the angle of inclination of the diagonal elements, and the concrete material behavior in the horizontal direction in order to better represent the diagonal compressive field of concrete and capture diagonal tension failure. This report focuses on modeling the effect of FSI and the diagonal compression and tension failure modes (failure modes 3 and 4 listed above) for RC walls. Bar buckling (failure mode 1), shear sliding (failure mode 5), and out of plane buckling of walls (failure mode 6) are not modeled here. Moreover hoop fracture and loss of confinement (failure mode 2) is modeled in a simplified manner based on the uniaxial material model of Mander et al. [1988].

The objective of this report is: (a) to refine and improve the beam-truss modeling approach of Lu and Panagiotou [2014] to better represent the diagonal compressive field and capture the diagonal tension failure mode; (b) provide a comprehensive study of the beam-truss modeling technique; and (c) extend the beam-truss modeling technique to model slabs and structural systems including walls and slabs. The model is validated using four planar and four non-planar RC walls subjected to cyclic static (uniaxial or multiaxial) loading, as well as a static cyclically loaded two bay slab-column specimen and a 5-story coupled T-walls-beam-slab specimen with triaxial base excitation. Shear-critical (defined herein as members that fail in

shear before they develop their flexural strength) RC walls are not considered here. All walls considered in this report develop their nominal flexural strength before failure. The global lateral force-lateral displacement and failure mode as well as strain contours and deformed shapes, as computed by the beam-truss model (BTM), are compared with the experimentally recorded response and damage state for each of the specimen. In addition, the effects of model parameters are discussed.

1.1 LITERATURE REVIEW

Lu and Panagiotou [2014] provide a literature review on nonlinear modeling approaches for non-planar RC walls and describe the main modeling approaches for RC walls:

1. fiber-section beam-column element models
2. wide column models, known also as equivalent frame models
3. two-dimensional (2D) truss models
4. three-dimensional (3D) truss models
5. beam-truss models ; and
6. finite element (FE) models with plane stress or solid elements.

Studies have used modeling approaches (1) and (2) to model FSI explicitly by incorporating 2D material models, e.g., Jiang and Kurama [2010] and Kolozviri [2013]. However, these authors are not aware of any such model capturing diagonal failures of RC walls under cyclic or dynamic loading. Approaches (3) to (6)—inherently—model FSI explicitly. This section focus on models that have captured diagonal failures of RC walls under cyclic (static or dynamic) loading.

Panagiotou et al. [2012] used 2D truss models to compute the instance and location of first diagonal crushing for two planar squat walls (height-to-length ratio = 0.9 and 1.3) and a perforated wall, all of which were subject to static cyclic loading. For the squat walls, significant loss of lateral strength was computed. The authors are not aware of any 3D truss model for RC walls that have modeled the diagonal failure of walls. Lu and Panagiotou [2014] developed the beam-truss modeling method and validated it with three cyclically loaded slender (height-to-length ratio grater or equal to 2) non-planar RC walls. Of the three case studies, two experienced diagonal compression failure, one of which experienced a significant loss of lateral strength. None of the aforementioned studies modeled diagonal tension failure in RC walls; however, the 2D truss model has been used to model diagonal tension failure of shear-critical RC columns [Moharrami et al. 2014].

Nonlinear FE models using plane stress elements or shell elements that use smeared crack and/or plasticity models have analyzed the cyclic behavior of experimentally tested RC walls that did not experience diagonal failure. A full literature review on this topic will not be presented. Ile et al. [2002] and Kotronis et al. [2009] used smeared fixed-crack plane stress models to analyze the shaking table tests of 5-story RC wall with slabs under dynamic loading. Ile et al. [2002] studied three 5-story wall specimens that consist of two parallel RC planar walls without openings linked together by slabs at every floor; of the three specimens, the first failed at the bar cut-offs and the latter two had a flexural-dominated behavior. The study used 2D

dynamic analysis and was in good agreement with the experimentally measured response including the failure mode. Kotronis et al. [2009] studied a 5-story coupled T-section wall specimen (identical in shape to that studied in Chapter 5) with flexure-dominated behavior. The study used 3D dynamic analysis and underestimated the displacement response in both horizontal directions.

Table 1.1 lists studies that used FE models to study the response of experimentally tested RC walls subjected to cyclic loading that experienced a shear failure (diagonal, horizontal sliding, or vertical sliding). All of the listed studies utilized smeared crack models (rotating or fixed crack) and plane stress or shell elements. The authors are not aware of any studies that have used solid elements and/or discrete crack methods to compute diagonal failures of RC walls subjected to cyclic loading. Of the studies listed in Table 1.1, only Palermo and Vecchio [2007] was able to capture diagonal tension failure with some success by using 2D analysis and plane stress elements. Out of the three wall specimens (height-to-width ratio of 2) they studied where diagonal tension or combined diagonal tension/compression failure was experimentally recorded, only one case computed the failure mode accurately. For the other two cases, the model computed crushing of the boundary zone. Sittipunt and Wood [1993] studied three slender perforated planar walls that experienced diagonal tension failure in the experimental test using plane stress elements and 2D analysis; they noted that, due to the smeared crack model used, diagonal tension failure could not be captured.

Table 1.1 Nonlinear finite element studies that computed shear or out-of-plane failure for RC wall specimens.

Reference	Analysis type	RC wall specimens	Computed failure modes ¹
Sittipunt and Wood [1993]	2D and 3D cyclic analysis with plane stress elements	Slender planar walls Slender perforated planar walls Squat L-shaped section walls	Diagonal compression
Ile and Reynouard [2000]	2D and 3D dynamic analysis with plane stress elements	Squat U-shaped section wall	Diagonal compression
Palermo and Vecchio [2002]	2D cyclic analysis with plane stress elements	Squat I-shaped section walls	Sliding shear Vertical slip planes
Palermo and Vecchio [2007]	2D cyclic analysis with plane stress elements	Slender and squat planar walls Slender I-shaped wall Slender perforated planar wall	Diagonal compression Diagonal tension ² Sliding shear

¹ Crushing of confined boundary and bar buckling and fracture failures modes are not included.

² Only captured in one out of the three studied specimens considered that experienced diagonal tension failure in the experimental test.

2 Beam-Truss Modeling Approach

2.1 OVERVIEW

This section describes the beam-truss modeling approach using the T-section RC wall, shown in Figure 2.1. Compared to the beam-truss modeling approach proposed in Lu and Panagiotou [2014], five changes have been made: (1) the angle of the diagonals is calculated based on the shear demand and the transverse reinforcement ratio; (2) nonlinear fiber-section Euler-Bernoulli beam elements are used in both the vertical and horizontal directions; (3) all vertical beams except those at the ends of each wall segment (including where the wall segment intersections another segment) and all horizontal beam elements are pinned (zero flexural rigidity) in the direction parallel to the length of the wall segment (in-plane direction); (4) the computation of the strain normal to the diagonal truss elements is improved for large angles of the diagonals; and (5) the tension strength of concrete in the horizontal direction is ignored. Changes 1, 4, and 5 are discussed in Sections 2.3, 2.4, and 2.5, respectively. The modeling approach is termed the default BTM when compared to an enhanced model in later sections where the effects of different model parameters are investigated.

Consider the T-section wall shown in Figure 2.1(a); the wall segment parallel to the x -axis is termed the web and the wall segment parallel to the y -axis is termed the flange. Figure 2.1(b) shows the BTM for this wall, which consists of vertical, horizontal, and diagonal elements. There are nine vertical lines: five represent the web and five represent the flange; line BF is common to both the web and the flange segments and is termed an intersection line. The points where the vertical and horizontal lines intersect comprise the nodes of the model. Each node has six degrees-of-freedom (DOFs); all DOFs are fixed at the base of the specimen. Figure 2.1(d) shows the placement of nodes for sub-segment S of the wall.

The types of elements used in the model are: (1) nonlinear fiber-section Euler-Bernoulli beam elements (called beams); (2) nonlinear fiber-section Euler-Bernoulli beam elements that are pinned in-plane (called pinned beams); and (3) nonlinear truss elements in the diagonals of the panels formed by the horizontal and vertical elements (see Section 2.3). Beams are used only for the vertical lines at the ends of a wall segment or at intersection line, as shown with thick lines in Figure 2.1(b); the remaining vertical lines and all horizontal elements are pinned beams, as shown with thin lines in Figure 2.1(b). Note that the pinned beams have flexural rigidity in the out-of-plane direction [Detail 1 of Figure 2.1(b)]. All elements used in this report use linear geometry and do not account for large displacements.

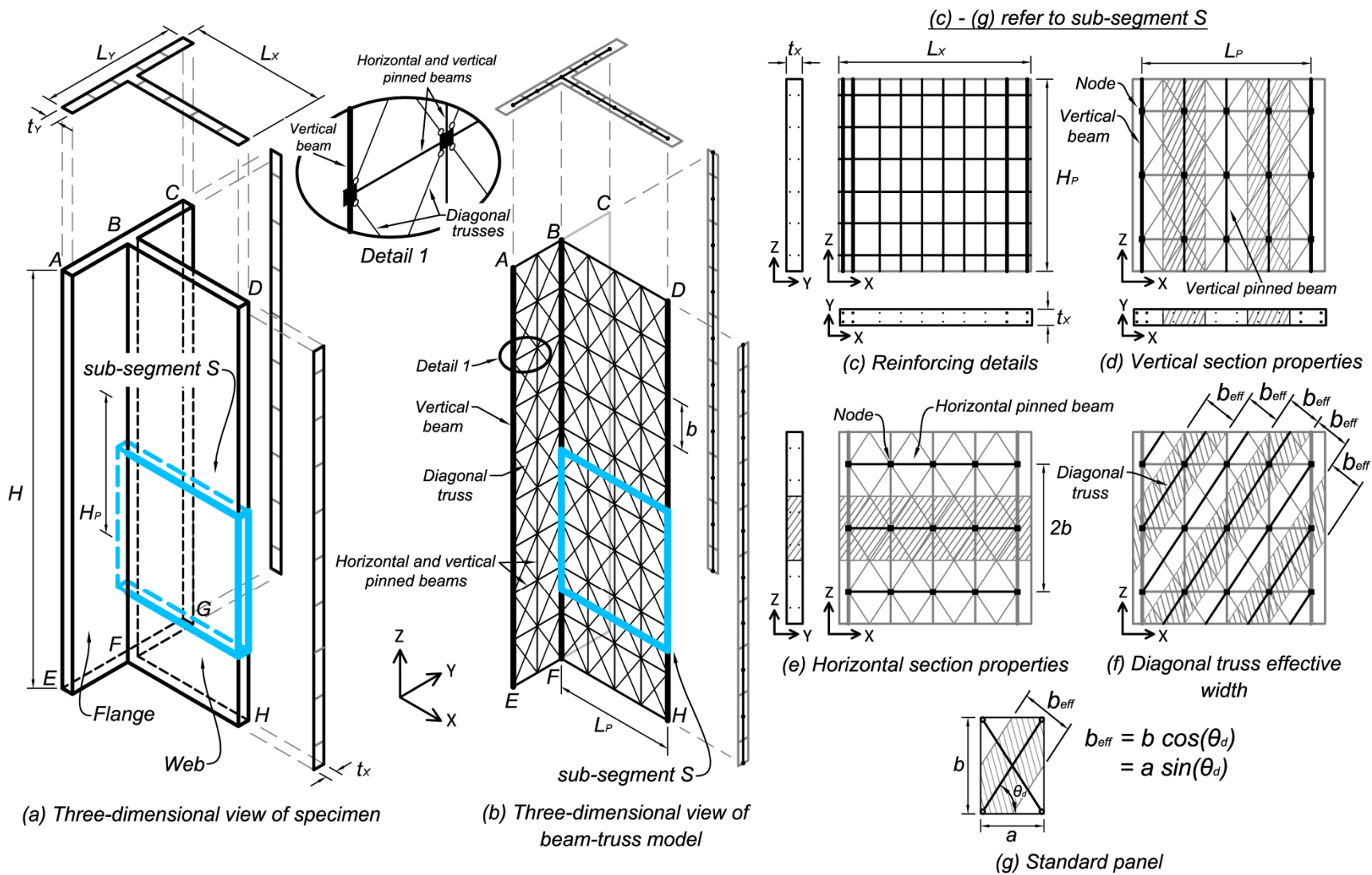


Figure 2.1 Schematic description of the beam-truss model approach for a T-shaped section wall.

The vertical and horizontal elements model the concrete and steel included in the section areas each element represents. Consider sub-segment S of the wall with reinforcing details shown in Figure 2.1(c). Figure 2.1(d) and (e) show a schematic of the section properties (area of concrete, area and layout of steel) of each of the vertical and horizontal elements, respectively. In these elements, a fiber section with 24 fibers in a 6×4 grid is used to represent the concrete and a single fiber to represent each steel bar. The diagonal truss elements model the diagonal compression field of concrete. The area of the diagonal element is the effective width multiplied by the average thickness of the wall in the panel considered; see Figure 2.1(f). The effective width of the concrete modeled by each diagonal is $b_{eff} = a \sin(\theta_d)$, as shown in Figure 2.1(g) for sub-segment S, where a is the length of the panel and θ_d is the inclination angle of the diagonal with respect to the horizontal elements. θ_d is referred to as the diagonal angle in this report. The material constitutive models are discussed in Section 2.2 and the determination of θ_d is discussed in Section 2.3.

2.2 MATERIAL MODELS

The uniaxial material model for concrete [*ConcretewBeta* in Opensees (http://opensees.berkeley.edu/wiki/index.php/ConcretewBeta_Material)] used in the BTMs is developed in Lu and Panagiotou [2014]; the stress-strain relationship is shown in Figure 2.2(a). The concrete material models the strength and stiffness degradation due to inelastic strains as well as the effect of tension stiffening of reinforced concrete. The material model, when used in the diagonal direction, accounts for the effect of normal tension on the behavior in compression. For the BTM discussed herein, the concrete material model uses the values of compressive strength of unconfined concrete, f'_c , given by cylinder tests; the initial stiffness is $E_c = 5000\sqrt{f'_c}$ (MPa) and f'_c occurs at a strain of $\varepsilon_c = 0.2\%$. The model accounts for the increased compressive strength and ductility due to concrete confinement using the parameters f_{cc} (peak confined strength), ε_{cc} (strain at f_{cc}), and ε_{cs} (strain which softening initiates); the values of these parameters are calculated per Mander et al. [1988]. The degrading branch of concrete in compression is regularized to provide mesh objectivity; the process is described in Lu and Panagiotou [2014] and a limit of $\varepsilon_u \leq (\varepsilon_o - 0.2\%)$ is used to prevent an excessively steep slope for the degrading branch. The reference length used for regularization of vertical and horizontal elements is 600 mm.

When used in the vertical direction, the concrete behaves uniaxially and includes the effects of tension stiffening. In the horizontal direction, the concrete is also uniaxial, but the tensile strength of the concrete is ignored; the reason for this choice is discussed in Section 2.5, and the effects of it are illustrated in Section 3.3. In the diagonal direction, the tensile strength of the concrete is ignored and the concrete material model takes into account the effect of normal tensile strain on the compressive strength based on Vecchio and Collins [1986] with modifications to account for size effects as described in Section 2.3. In this case, the diagonal compressive stresses are multiplied by the concrete compressive stress reduction factor β , which reduces the compressive stress based on the normal tensile strain. This relationship between β and the normal tensile stress is discussed in Section 2.3.

The steel material model used in this report, called parallel GMP, has a multi-linear monotonic envelope that approximates the post-yield nonlinear hardening, as shown in Figure

2.2(b), while capping the ultimate stress. The material is implemented using three Giuffre-Menegotto-Pinto (GMP) materials (*Steel02* in Opensees) joined in parallel. Each of the parallel GMP models used in the BTMs of this report are calibrated to the points: (1) yield stress f_y , (2) $f = 0.5(f_y + f_u)$ and (3) f_u , where f_u is the ultimate stress. In the case where point (2) is not available based on steel coupon tests, the post-yield tangent modulus is assumed to be equal to $0.03E_s$ between points (1) and (2). The parallel GMP model does not model the effects of bar buckling. The effect of bar fracture is not considered in the case studies with static loading presented in the report; it is discussed in Section 5.7 for the coupled wall specimen under dynamic loading.

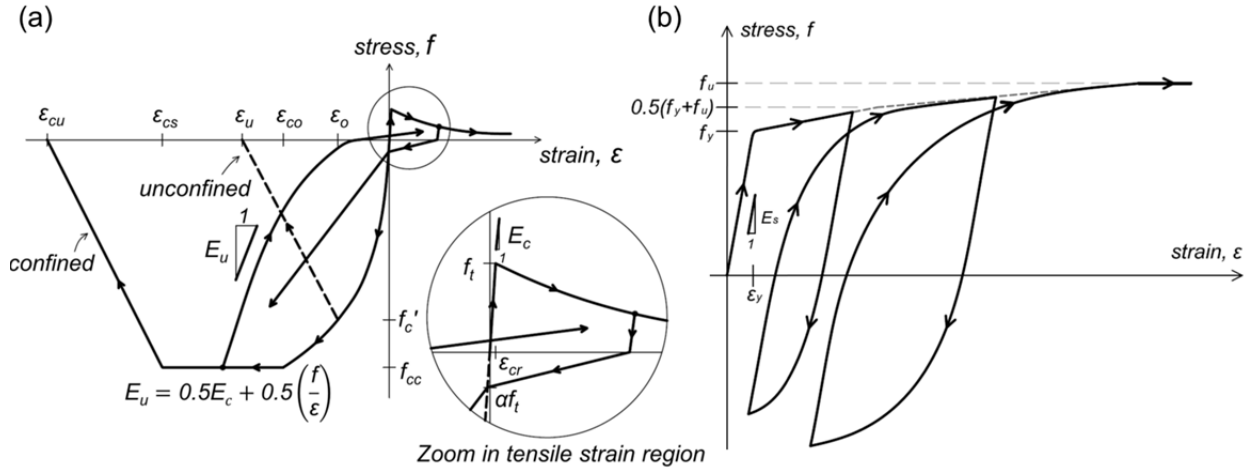


Figure 2.2 Uniaxial stress-strain laws for the (a) concrete and (b) steel material models.

2.3 BIAxIAL CONCRETE COMPRESSIVE STRESS REDUCTION FACTOR AND THE CALCULATION OF NORMAL TENSILE STRAIN

The concrete material model used in the diagonal truss elements accounts for the effect of the biaxial strain field on the concrete compressive behavior in accordance with the Modified Compression Field Theory [Vecchio and Collins 1986]. The equations describing this effect have been modified to account for size effects, as described in Panagiotou et al. [2012]. For the concrete material model used in this report, the biaxial effect is modeled by multiplying the diagonal compressive stresses at each time step by the concrete compressive stress reduction factor β , which is calculated based on the normal tensile strain ϵ_n computed at every computation step. The β - ϵ_n relationship is regularized to provide mesh objectivity; a reference length of 849 mm is used, which corresponds to the diagonal length of the panels over which strain was measured in the experimental tests of Vecchio and Collins [1986]. The relationship between β and ϵ_n used for the diagonal trusses is triaxial, passing through the points (β, ϵ_n) : (1, 0), (0.4, 0.01), and (0.1, 0.04); the points are chosen to be similar to that proposed by Vecchio and Collins [1986] and the comparison is shown in Figure 2.3(a).

Compared to the diagonal truss elements of Lu and Panagiotou [2014], where the normal tensile strain ϵ_n was computed using a zero-stiffness gage element, the diagonal trusses used

herein are implemented as a four-node rectangular element that consists of two diagonal truss elements. The value of ε_n is taken as the strain normal to the direction of the truss element computed at the center of the element using the standard linear strain-displacement interpolation functions for a four-node bilinear quadrilateral element [Hughes 2000]. This is shown in Figure 2.3(b) for one of the diagonal truss elements that comprise the rectangular element. This method allows the normal strain to be computed more accurately when θ_d is significantly different than 45° ; for $\theta_d = 45^\circ$, the calculated ε_n is the same as that calculated with the method described in Lu and Panagiotou [2014].

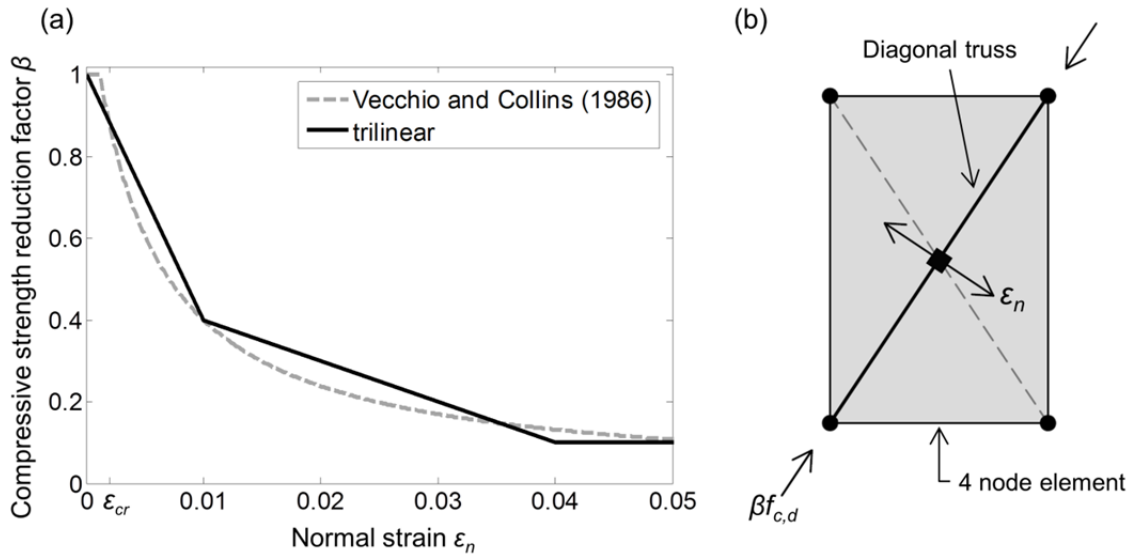


Figure 2.3 (a) Concrete compressive strength reduction factor, as proposed in Vecchio and Collins [1986], compared to the trilinear relation used in this report for an element length of 600 mm; and (b) schematic of normal strain calculation for one of the diagonal trusses of the 4-node rectangular element.

2.4 DETERMINATION OF INCLINATION ANGLE FOR DIAGONAL ELEMENTS

Panagiotou et al. [2012] and Lu and Panagiotou [2014] considered RC wall specimens and suggested an inclination angle, θ_d , of 45° for the diagonal elements. The case studies considered in Panagiotou et al. [2012] included two squat walls, with a continuous diagonal strut spanning from the top corner to the opposite bottom corner and a slender perforated wall. Lu and Panagiotou [2014] used vertical beams that had flexural rigidity in the in-plane direction, which contributed to the lateral strength reducing the dependency on diagonal angle.

Because the BTM uses a fixed angle for the diagonal truss elements, the determination θ_d may affect the computed strength, ductility, and failure mode. Moharrami et al. [2014] considered slender shear-dominated RC columns and determined the diagonal angle θ_d based on the stress state at first cracking assuming uniform compressive and shear stress. This way of determining θ_d may not be appropriate for members RC walls that have adequate amount of transverse reinforcement to develop their flexural strength. For RC beams and piers that have

adequate shear reinforcement to develop their flexural strength, θ_d depends on the amount of transverse reinforcement [Hines and Seible 2004]. Additionally, the angle suggested by Moharrami et al. [2014] may lead to an unrealistic flow of forces for specimens where geometry governs the diagonal angle, such as walls that are squat or non-uniform over the height. Section 3.4 investigates the effect of the diagonal angle on the computed response and shows that a BTM with an angle smaller than suggested in this section may underestimate of lateral strength or compute a premature diagonal tension failure. Lu and Panagiotou [2014] has shown that a BTM with larger diagonal angle may compute the onset of diagonal crushing failure at a smaller drift ratio.

Nine RC wall specimens are studied in this report, all of which have a transverse reinforcement ratio $\rho_t \geq 0.16\%$; all specimens considered in this report develop their flexural strength before failure. Four of the specimens are squat (height-to-width ratio ≤ 2) or non-uniform over the height. The diagonal angle used for the BTM herein corresponds to the inclination of the compressive struts formed in the wall at the maximum resisted lateral load, as computed using a strut-and-tie model. For RC walls uniform over their height, the equation relating diagonal angle to transverse steel ratio and applied lateral load is discussed in Section 2.4.1. For RC wall specimens that have irregular shape or steel placement, the strut-and-tie model should be used to determine the load path, inclination of compression struts, and subsequent diagonal angles in the wall piers. In the case where there are multiple angles, the angle corresponding to the most amount of shear (such as at the bottom corner of the specimen where the majority of the shear is expected to be resisted) should be used. Section 2.4.2 discusses the determination of diagonal angle for coupled walls.

2.4.1 Walls Uniform over their Height

For RC walls that are uniform over their height, diagonal angle is determined such that:

$$\theta_d = \tan^{-1} \left(\frac{V_{max}}{f_{y,t} \rho_t t_w d} \right) \leq 65^\circ \quad (2.1)$$

where V_{max} is the maximum resisted lateral force, t_w is the thickness of the wall, and d is the distance between the outer vertical lines in the direction of loading. For walls with asymmetric lateral load resistance, the diagonal angle corresponding to absolute maximum resisted lateral force is used. The upper bound for the diagonal angle θ_d agrees with ACI 318 [2011] restrictions on strut-and-tie procedures. In addition, it is suggested that θ_d be greater than or equal to 45° for walls uniform over height that have an aspect ratio larger than 1, except for the case of walls subjected to large tension forces (which is beyond the scope of this report). The maximum resisted lateral force is not known prior to the analysis, and it is suggested to use the shear corresponding to $1.2M_n$ as a first guess for V_{max} ; M_n is the nominal moment, defined as the moment at the first instance where either the extreme steel fiber reaches 1% strain or the concrete reaches -0.3% strain. After running the BTM with the determined angle, the user can check the relation in Equation (2.1) and adjust the diagonal angle to the computed V_{max} if necessary. In most cases, zero or one iteration is sufficient to satisfy Equation (2.1) to an acceptable degree (all specimens in this report satisfy this equation within $\theta_d \pm 2^\circ$).

For specimens where $H \leq d \tan(\theta_d)$, where θ_d is defined by Equation (2.1) and H is the height of the specimen, it is suggested to use an angle such that a continuous diagonal strut spans from the top corner to the opposite bottom corner (e.g., the BTM mesh of specimen Unit 1.0 in Chapter 3). However, this suggestion is only validated based on statically loaded individual walls with a stiff loading beam at the top.

2.4.2 Coupled Walls

This section will discuss the determination of load path and diagonal angle for the case of coupled walls as that shown in Figure 2.4(a). The effect of the coupling beam on each wall is quantified. For the cases where the coupling mechanism is “weak,” the diagonal angle of each wall is determined individually. Figure 2.4(b) shows the forces from the coupling beam on the walls. The term “compression wall” refers to the wall that experiences compression forces due to coupling, and “tension wall” refers to the wall that experiences tension forces due to coupling. For coupling beam without diagonal reinforcement, the nominal moments in each direction M_A and M_B , and associated shear V_{cpl} can be readily determined. For coupling beams with diagonal reinforcement, Figure 2.4(c) shows the forces at the ends including the effect of horizontal reinforcement. The diagonal steel reinforcement is assumed to be at yield stress, while the horizontal reinforcement varies from zero to yield stress over the length of the coupling beam. Taking moments around the compression zone on each face, the moment capacity of the coupling beam on each face is given by:

$$M_A = (T_d \cos \alpha + T_{h,b})z_b = (A_{sd}f_{y,d} \cos \alpha + A_{sh,b}f_{y,h})z_b \quad (2.2)$$

$$M_B = (T_d \cos \alpha + T_{h,t})z_b = (A_{sd}f_{y,d} \cos \alpha + A_{sh,t}f_{y,h})z_b \quad (2.3)$$

where A_{sd} is the area of steel in the diagonal direction, $f_{y,d}$ is the yield stress of the diagonal steel, $A_{sh,t}$ and $A_{sh,b}$ is the area of horizontal steel in the top and bottom of the coupling beam, respectively, $f_{y,h}$ is the yield stress of the horizontal steel, and z_b is the moment arm for the tension forces in each face. Note that $A_{sh,t}$ or $A_{sh,b}$ includes the area of steel in the effective flange width if a slab attached to the top or bottom of the coupling beam, respectively. The shear strength corresponding to this stress state of the beam is:

$$V_{cp} = \frac{(M_A + M_B)}{L_{cp}} = [2A_{sd}f_{y,d} \cos \alpha + (A_{sh,t} + A_{sh,b})f_{y,h}] \frac{z_b}{L_{cp}} \quad (2.4)$$

where L_{cp} is the length of the coupling beam. Note that Equations (2.2 – 2.4) assume that the coupling beam is not under any axial load; however, the coupling beam can have net axial compression, which will result in larger shear strength (see Section 5.4). The contribution of concrete in shear at the compression zone $V_{c,cb}$ and $V_{c,ct}$ can be defined to obtain equilibrium on the faces of the coupling beam. The total shear resisted at the compression zone at bottom corner of the coupling beam is $V_{c,b} = V_{cp} - T_d \sin \alpha$. Figure 2.4(c) and Equation (2.4) are based on a similar diagram from Paulay and Priestley [1992]. Figure 2.4(d) shows the base shear that results for $V_{c,cp}$ of the bottommost coupling beam transferred directly to the compression zone of the wall, $V_{b,cp} = V_{c,cp} \cot \gamma$. The following describes two characteristic cases of behavior for the coupled walls:

1. If $V_{b,cp}$ is greater than or equal to the base shear required to develop the nominal moment of the single wall, the coupling effect is strong: the coupled walls should be treated as a single, uniformly perforated wall, and the load path should be modeled as such. The strut running from the bottommost coupling beam to the base corner should be used to determine the diagonal angle.
2. If $V_{b,cp}$ is smaller than that required for case (1), the coupled walls should be treated as individual walls uniform over their height when determining the diagonal angle [i.e., using Equation (2.1)]. The effect of the coupling forces M_{AB} , M_{CD} , and V_{cp} should be taken into account when calculating M_n for the first guess of diagonal angle. The diagonal angle corresponding to the absolute maximum resisted lateral force should be used.

For coupled and perforated walls, appropriate engineering judgment should be used to determine the dominant load path; it is suggested to test the diagonal angles corresponding to both of the cases above. In this report, only the first case will be used for a BTM – specimen SLO in Section 5.2.

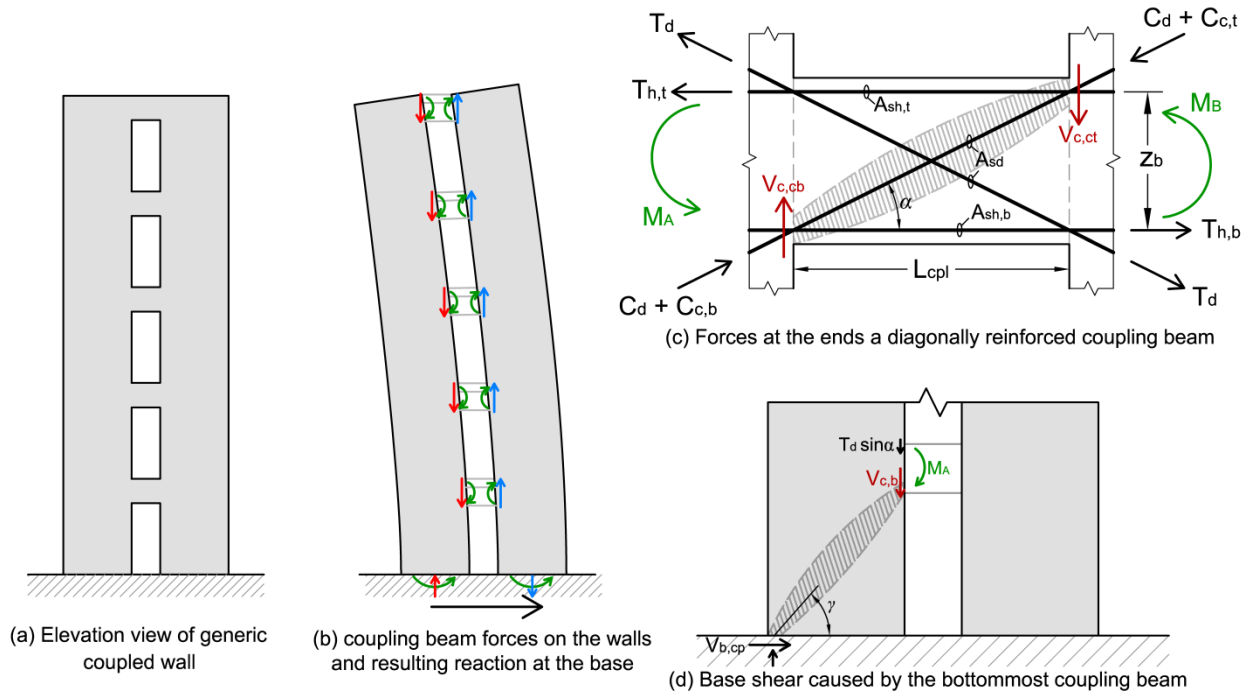


Figure 2.4 Schematics including coupling forces for a coupled wall.

2.5 MODELING OF TENSION FOR CONCRETE IN THE HORIZONTAL DIRECTION

For the default BTM used in this report, the tensile strength of concrete in the horizontal direction is ignored (i.e., $f_t = 0$). This section discusses the reason for this choice, and the effects of it are presented in Section 3.3 for three specimens. In previous research, Panagiotou et al. [2012] and Lu and Panagiotou [2014] modeled tension stiffening in the horizontal direction the

same way as for the vertical direction, and Moharrami et al. [2014] combined the effects of aggregate interlock and tension resistance in the concrete material used in the horizontals.

The modeling of horizontal tension affects the computed response for the following three cases: (1) the wall experiences diagonal tension failure without any diagonal crushing; (2) softening in compression of a diagonal truss element occurs before diagonal tension failure; and (3) distributed shear cracking occurs before reaching nominal flexural strength.

The first case occurs for shear-critical specimens that are too slender for a continuous diagonal strut to span from the top corner to the opposite bottom corner; the modelling of aggregate interlock is important for computing the peak lateral strength and instance of failure. None of the specimens considered in this report fall into this case. However, the case is exemplified by the shear critical columns studied by Moharrami et al. [2014].

The second case occurs for squat walls that are shear-critical or have low transverse reinforcement. This case is exemplified by specimen Unit 1.0 discussed in Chapter 3 and the 5-story coupled wall specimen discussed in Chapter 5. For this case, modeling the effects of tensile concrete strength and aggregate interlock in the horizontal direction reduces the horizontal strains computed, resulting in a larger computing lateral displacement at the onset of compression softening of the diagonals compared to the default BTM. Modeling of horizontal tension does not affect the peak lateral strength or the development of diagonal tension failure after the onset of softening in compression.

The third case is observed most prominently in the T-shaped section walls considered herein: specimens TW2 and NTW1 (discussed in Chapter 3) which have moderate transverse reinforcement and a larger flexural strength for the direction with the flange in tension. In these cases, modeling the effects of tensile concrete strength and aggregate interlock causes the BTM to compute larger stiffness up to the nominal flexural strength compared to the experimentally measured response. This is because the behavior of concrete in the horizontal directions is not coupled with these in the vertical and diagonal directions; therefore, the horizontals may remain uncracked while the diagonal elements compute widespread distributed cracking.

Because the specimens in this report fall into behavior types 2 and 3, ignoring the tension strength of concrete in the horizontal direction results in more accurate computed response and failure mode of the specimen.

2.6 NONLINEAR ANALYSIS PROGRAM

The nonlinear analysis program OpenSees [McKenna et al. 2000] was used for all the analysis described in this report. The material models for concrete and steel are available in OpenSees as *ConcretewBeta* and *Steel02* in combination with the *Parallel* material. For the beam elements, the existing OpenSees nonlinear force-based beam-column elements were used with linear geometric transformation. Gauss-Lobatto quadrature with two points was used for the beam elements. The four-node element used for the diagonals to account for the biaxial effect on concrete strength was programmed in OpenSees by the authors. A computer with a 3.47-GHz Intel Core i7 CPU was used to compute the response.

3 Validation for Static Loading

3.1 SPECIMEN OVERVIEW AND BTM RESULTS

In this section, eight case studies (four planar and four non-planar walls) of RC walls subject to static cyclic loading are presented. Two of the non-planar walls were multi-axially loaded. All RC walls specimens considered in this section are uniform over the height with no openings and were subjected to a concentrated force at their top in a single bending (cantilever) configuration. Table 3.1 lists the specimen name, cross-section shape, axial load ratio ($N/f'_c A_g$ where N is the axial force and A_g is the gross cross-section area), longitudinal reinforcing steel ratio ρ_l , transverse reinforcing steel ratio ρ_t , shear span-to-depth ratio (defined as M/VL_w , where M is the bending moment at the base, V is the base shear force, and L_w is the length of the wall in the direction of loading), and failure mode for each of the specimens. All of the specimens except the first have a shear span-to-depth ratio of 2.0 or greater, and all of the specimens developed their nominal flexural strength prior to failure. The reader is referred to the paper or report referenced in Table 3.1 for further information about each specimen.

Each case study is referred to by the specimen name described in Table 3.1. For specimens subject to uniaxial loading, the segment of the wall in the direction of loading is termed the “web”; segments perpendicular to the web are termed “flanges.” For specimens loaded multi-axially, the segments of the walls are termed based on their orientation with respect to North-South and East-West directions as defined in Table 3.1 (i.e., the N-S segment is parallel to the N-S direction). For each case study, a beam-truss model (BTM) is constructed and subjected to the same loading as the experimental specimen; the number of vertical lines and diagonal angle for each model is listed in Table 3.1. For all BTMs, the single-iteration procedure for determining diagonal angle described in Section 2.4 was followed; the diagonal angle is constant throughout a specimen BTM. The material properties used are these reported in the references describing the experimental results. Appendix A shows the strain contour and displaced shape for each specimen at selected drift ratios.

Unit 1.0: Specimen Unit 1.0 [MestyaneK 1986] is a squat planar wall with confined boundary columns at the ends subject to static reverse cyclic loading. The average longitudinal steel ratio is 0.8%, and 83% of the total amount of longitudinal steel is in the boundary columns. For the unconfined part of the wall, $\rho_l = 0.16\%$ and $\rho_t = 0.16\%$. No external axial load was applied to the wall. Figure 3.1(a) shows the experimental shear force-drift ratio response for the specimen, which experienced a 24% loss of lateral strength at the peak drift of the second cycle with 0.8% peak drift ratio. Specimen Unit 1.0 failed with the kinking of the boundary element and crushing at the base along with the formation of a major diagonal crack extending from end

to end of the specimen in the diagonal direction; high strains were observed in the horizontal web reinforcement near the main diagonal, resulting in fracture of two horizontal bars and kinking of vertical web bars along the main diagonal. Figure 3.2(a) shows the damage pattern at the end of the experimental test.

The BTM of specimen Unit 1.0 has six vertical lines, of which the two outer lines represent the confined boundary elements. The effect of using beams to model the boundary elements is discussed in Section 3.5. The diagonal angle was determined based on the geometry of the wall: because of the large amount of reinforcement in the loading beam and foundation of the specimen, the diagonal angle was determined to allow the formation of a major diagonal strut from end to end of the specimen in each loading direction. The computed shear force-drift ratio response is shown in Figure 3.1(a) and is in good agreement with the experimental response. The BTM computed a 46% loss of lateral strength at 0.67% drift ratio of the first cycle with 0.8% peak drift ratio. The kinking of the boundary reinforcement was not captured. Figure 3.2(a) shows the deformed shape and strain contour at this point; the computed failure mode is a localized diagonal crushing in the web followed by strain accumulation in the horizontal elements adjacent to the main diagonal. The effect of modeling the concrete tension resistance in the horizontal direction for this specimen is discussed in Section 2.5.

Unit 2.0: The only difference between specimens Unit 1.0 and Unit 2.0 [Mestyanek 1986] is the aspect ratio of the wall: specimen Unit 2.0 has a shear span-to-depth ratio of 2.0, making it a more slender wall in comparison. Figure 3.1(b) shows the experimental shear force-drift ratio response for the specimen, which experienced a 15% drop of lateral strength near the end of the first cycle with 1.3% peak drift ratio. In the final cycle, which has a peak drift ratio of 2%, the specimen has 69% of the peak lateral strength. The experimental failure mode was a mixture of crushing of the diagonals, kinking of boundary elements, and high horizontal strains along diagonal cracks. Section 3.4 discusses the failure mechanism of Unit 2.0 in more detail.

The BTM of Unit 2.0 has six vertical lines; the outer two lines are modeled as beams that represent the confined boundary elements. Because of the low transverse reinforcement ratio in the web, the diagonal angle for the BTM is determined by the geometry. Section 3.4 discusses the effects of the choice of diagonal angle on this specimen and its failure mechanism. The computed shear force-drift ratio response is shown in Figure 3.1(b) and is in good agreement with the experimental response, but computes only a diagonal crushing failure mode at 1.9% drift. The peak horizontal strain at this point is 0.35%. The inability of the BTM to compute the diagonal tension failure mode of the specimen is probably because the fixed diagonal angle does not correspond to the angle of the diagonal crack (about 50° as discussed in Section 3.4) associated with failure of this specimen.

WSH6: Specimen WSH6 [Dazio et al. 2009a] is a rectangular wall with confined boundary elements at the two ends. In the unconfined part of the web section, the wall has $\rho_l = 0.52\%$ and $\rho_t = 0.25\%$. The specimen has an axial load ratio of 10.8%. Figure 3.1(c) shows the experimental shear force-drift ratio response for the specimen, which failed due to buckling of longitudinal bars in the boundary element, crushing of the compression zone, and fracture of a number of confining hoop at 1.9% drift of the last cycle. The BTM has eight vertical lines; the outer two lines are modeled with beams that represent the confined boundary elements. Figure 3.1(c) shows the computed shear force-drift ratio response. The BTM underestimates the strength for the cycle with 0.6% peak drift ratio by a maximum of 7.6% due to localization in the vertical

members during cracking, but has good agreement with the experimental response for all other cycles until the failure of the specimen, which was not modeled.

B6: Specimen B6 [Oesterle et al. 1979] is a planar wall with large heavily reinforced boundary elements: each boundary element is 16% of the total length of the wall with 3.7% longitudinal steel ratio. In the unconfined part of the wall, $\rho_l = 0.3\%$ and ratio $\rho_t = 0.62\%$. The specimen has an axial load ratio of 13.4%. Figure 3.1(d) shows the experimental shear force-drift ratio response of the specimen. Oesterle et al. [1979] reported signs of spalling and flaking in the diagonal direction as early as the last cycle with 1.1% peak drift ratio. The specimen failed at 1.4% drift ratio during the second cycle with 1.7% peak drift ratio due to concrete diagonal crushing of the diagonal concrete compressive struts near the base, which propagated upwards along the height of the wall. The damage state of the specimen is shown and discussed in Section 3.5. Although the web of the specimen was heavily damaged, the boundary elements were in good condition.

The BTM has six vertical lines; the outer lines use beams to represent the confined boundary elements. Because the boundary elements of the specimen are large, the horizontal and diagonal elements adjacent to the boundary element account for the thickness of the boundary element where it overlaps with the mesh; this method of accounting for the large boundary element is described in detail and discussed in Section 3.5. The computed shear force-drift ratio response is shown in Figure 3.1(d) and is in good agreement with the experimental response. Failure is computed during the first cycle with max drift of 1.7% and consists of crushing of the concrete in the diagonal direction and a vertical propagation of the crushing (shown in Section 3.5), and is in excellent agreement with the experimental response. Additionally, the boundary element sustained very little damage.

F1: Specimen F1 [Oesterle et al. 1976] is a I-section wall with shear span-to-depth ratio of 2.4 and heavily reinforced flanges ($\rho_l = 3.4\%$ in the flanges). In the unconfined part of the wall, $\rho_l = 0.3\%$ and $\rho_t = 0.71\%$. The axial load is only from self-weight of the wall and the loading beam. The experimental shear force-drift ratio response is shown in Figure 3.1(e); the specimen experienced significant loss of the lateral strength at -1.9% drift during the first cycle with 2.2% peak drift ratio due to diagonal crushing of the web. Figure 3.2(c) shows the damage pattern at the end of the experimental test.

The BTM has a total of eleven vertical lines, seven of which form the web. The diagonal angle for the web (the wall segment in the direction of loading) and the flanges (the wall segments parallel to the direction of loading) are determined separately based on the single-iteration procedure described in Section 2.4. Figure 3.1(e) shows the computed shear force-drift ratio response, which is in excellent agreement with the experimental response until the failure of the specimen. The BTM computes failure at 1.9% drift during the first cycle with max drift ratio of 2.2%, but earlier than that observed in the test specimen. The computed failure mode, shown in Figure 3.2(b), is crushing of concrete in the diagonal direction that propagates horizontally; it is in good agreement with the experimentally observed failure mode.

TW2: Specimen TW2 [Thomsen and Wallace 1995] is a T-section wall with a shear span-to-depth ratio equal to 3 and confined boundary elements at the ends of the web and flange, as well as in the intersection. In the web, $\rho_l = 0.45\%$ and $\rho_t = 0.45\%$; in the unconfined part of the flange, $\rho_l = 0.33\%$ and $\rho_t = 0.33\%$. The specimen has an axial load ratio of 7.4%. Figure 3.1(f) shows the experimental shear force-drift ratio response as reported in Thomsen and

Wallace [1995] after being corrected for rotation and uplift of the foundation during testing. The positive load direction corresponds to flange in compression, and the negative load direction corresponds to flange in tension. For the negative direction, specimen TW2 reaches the nominal moment at 1% drift and experiences a loss of lateral load capacity during the last cycle at -1.7% drift due to out-of-plane instability of the tip of the web that buckled over several hoop spaces; although extensive spalling was observed at the tip of the web, there was no loss of confinement during the out-of-plane instability failure.

The BTM has a total of thirteen vertical lines, seven of which forms the wall segment in the direction of load application. Due to the large size of the confined boundary element at the end of the web, the boundary element is represented by two vertical lines: the horizontal and diagonal elements between these lines represent the transverse reinforced and confined concrete of the boundary element in the respective directions. Of the two lines that encompass the confined boundary element at the end of the web, only the vertical line at the end of the web uses beams with in-plane flexural rigidity. The boundary elements at the end of the flanges are represented by one vertical line. The computed shear force-drift ratio response is shown in Figure 3.1(e). For the positive direction of loading, the BTM computes a 10% overestimation of lateral force up to 1% drift ratio, but the computed peak lateral force is in very good agreement with the experimentally measured response. In the negative direction of loading, the BTM overestimates the lateral force by 8% up to 1.25% drift ratio, and overestimates the peak lateral force by 6%; the 2% decrease of the computed lateral strength for the cycle with max drift ratio of 1.7% in the negative direction is due to spalling and minor crushing of the vertical element at the web tip. For the BTM results presented in this section, the out-of-plane instability of the end of the web are not modeled.

NTW1: Specimen NWT1 [Brueggen 2009] is a T-section wall with a shear span-to-depth ratio of 3.2 in the N-S direction and 4 in the E-W direction. The wall has confined boundary elements at the ends of both segments. The average ρ_l over the section is 1.6%. In both the N-S (called the web) and E-W (called the flange) segments, ρ_l of the unconfined regions is 0.3%; $\rho_t = 0.61\%$ and 0.26% in the web and flange, respectively. The specimen is loaded multi-axially with cycles in the N-S, E-W, and skew (including diagonal and hour-glass shaped cycles) directions, and has an axial load ratio of 3.3%. Figure 3.3 shows the experimental shear force-drift ratio response for the specimen for the three directions of loading. During the first cycle in the N-S direction at -2% drift ratio, buckling of longitudinal reinforcement, opening of confining hoops legs, and crushing of the concrete core was observed at the confined boundary element at the tip of the web. Following the web failure, testing in the N-S direction was stopped and the specimen was loaded in the E-W direction up to 4% drift; buckling and fracture of longitudinal reinforcement and crushing of the boundary areas at the flange tips in the first cycle at 4% drift caused a loss of lateral load capacity. The final cycle was in the N-S direction up to 2% drift and resulted in the fracture of two bars at the end of the web, resulting in a 20% loss of lateral load capacity.

The BTM of specimen NTW1 has 13 vertical lines in total, 7 of which forms the web (the wall segment in the N-S direction) and 7 forms the flange (wall segment in the E-W direction). Figure 3.3 shows the computed shear force-drift ratio response of the BTM in comparison to the experimentally measured response. For the N-S cycles, the computed response shows very good agreement with the experimental response up to the point of failure, with 6% overestimation of

the peak lateral strength in the negative (flange in tension) direction. However, the effect of bar buckling and loss of confining hoops at the web tip was not modeled; thus the failure mode and associated loss of strength was not captured. For the E-W cycles, the difference between the monotonic and cyclic response is due to the accumulated strain in the flange from the N-S and SKEW cycles; the BTM computes a 10% underestimation of the response for the cycles at 3% drift. In the SKEW cycles, the computed response ranges from excellent agreement to decent agreement (with a maximum of 13% underestimation of the strength) prior to the last cycle; the last SKEW cycle in the N-S direction shows overestimation of the response because the BTM did not capture the failure mode due to bar buckling.

TUB: Specimen TUB [Beyer et al. 2008] is a U-section wall with a shear span-to-depth ratio of 2.8 and 2.6 in the N-S and E-W direction, respectively, with confined boundary elements at the ends of all wall segments. For this specimen, the segment of the wall parallel to the E-W direction is called the web, while the two segments parallel to the N-S direction are called the flanges. ρ_l and ρ_t in the unconfined portions of the wall are 0.38% and 0.45%, respectively. The specimen has an axial load ratio of 4.0% and is loaded in four alternating cycles: loading in the N-S direction (N-S), loading in the E-W direction (E-W), loading in the diagonal direction (DIAG), and a cycle which loads the wall in an hourglass shape (SWEEP). Figure 3.4 shows the experimental response of the specimen for the four types of cycles. Specimen TUB failed due to crushing of the diagonal in compression in the unconfined part of the web using the last SWEEP cycle; the damage state of the web is shown in Figure 3.2(c). The failure is attributed to spalling of the concrete in the web, which reduced the wall section in that area [Beyer et al. 2008]. The diagonal crushing failure resulted in a 36% reduction of the lateral load capacity in the E-W direction.

The BTM has thirteen vertical lines in total: five of which form the web (the wall segment in the E-W direction) and five form each of the two flanges (wall segments in the N-S direction). The boundary elements at each corner are modeled with a single vertical line which has flexural rigidity in both horizontal directions. Figure 3.4 shows the computed shear force-drift ratio response of the BTM in comparison to the experimentally measured response. For the N-S, E-W, and SWEEP cycles, the computed response shows excellent agreement with the experimental response. In N-S and E-W cycles, the computed maximum lateral strength has less than 3% difference from the experimentally recorded strength, while in the SWEEP cycles, the computed maximum lateral strength has less than 13% difference from the experimentally recorded strength. The computed response underestimates the response for the DIAG cycles, especially in the negative E-W direction, which corresponds to loading in the south-west direction toward the tip of the web. The BTM computes failure due to crushing of diagonal concrete in the web of the wall at 2% drift of the last E-W cycle, resulting in a 9% drop of lateral load capacity in the E-W direction; this E-W cycle precedes the SWEEP cycle in which the experimental failure was observed, but the location and mode of failure is in good agreement with the experimental results. The strain contour at the point of web crushing is shown in Figure 3.2(c) in comparison to the experimental failure mode.

Table 3.1 Characteristics of eight experimentally tested specimens and beam-truss model parameters.

Specimen	Cross-section shape (confined areas shaded)	Axial load ratio	f'_c (MPa)	ρ_l (average)	Steel ratio for unconfined area ¹		Shear span-to-depth ratio ¹	Beam-truss model parameters		Predicted failure mode (reported failure mode) ²
					ρ_l	ρ_t		Total # of vert. lines	Diagonal angle ¹	
Unit 1.0 [Mestyaneck 1986]		0.3%	27.0	0.8%	0.16%	0.16%	1.0	6	44.4°	DC, DT (DT)
Unit 2.0 [Mestyaneck 1986]		0.3%	26.5	1.6%	0.16%	0.16%	2.0	6	64.4°	DC (DC, DT)
WSH6 [Dazio et al. 2009a]		10.8%	45.6	0.8%	0.52%	0.25%	2.0	8	58°	None (BBF, VC)
B6 [Oesterle et al. 1979]		13.4%	24.0	2.3%	0.30%	0.62%	2.4	6	54.4°	DC (DC)
F1 [Oesterle et al. 1976]		0.3%	38.4	2.1%	0.30%	0.71%	2.4	11	49°	DC (DC)
TW2 [Thomsen and Wallace 1995]		7.4%	41.4	1.2%	0.45%	0.45%	3.0	13	59°	None (CSB)
NTW1 [Brueggen 2009]	N-S 	3.3%	49.3	1.7%	0.30%	0.61%	3.2	13	47°	None (BBF, VC)
	E-W 				0.30%	0.26%	4.0		54.4°	
TUB [Beyer et al. 2008]	N-S 	4.0%	54.7	1.0%	0.38%	0.45%	2.8	13	49.5°	DC (DC)
	E-W 				0.38%	0.45%	2.6		59°	

¹ Given for the direction of applied load only.

² BBF = Bar buckling and fracture, CSB = Buckling of the confined section, VC = vertical concrete crushing, DC = diagonal concrete crushing, DT = diagonal tension failure.

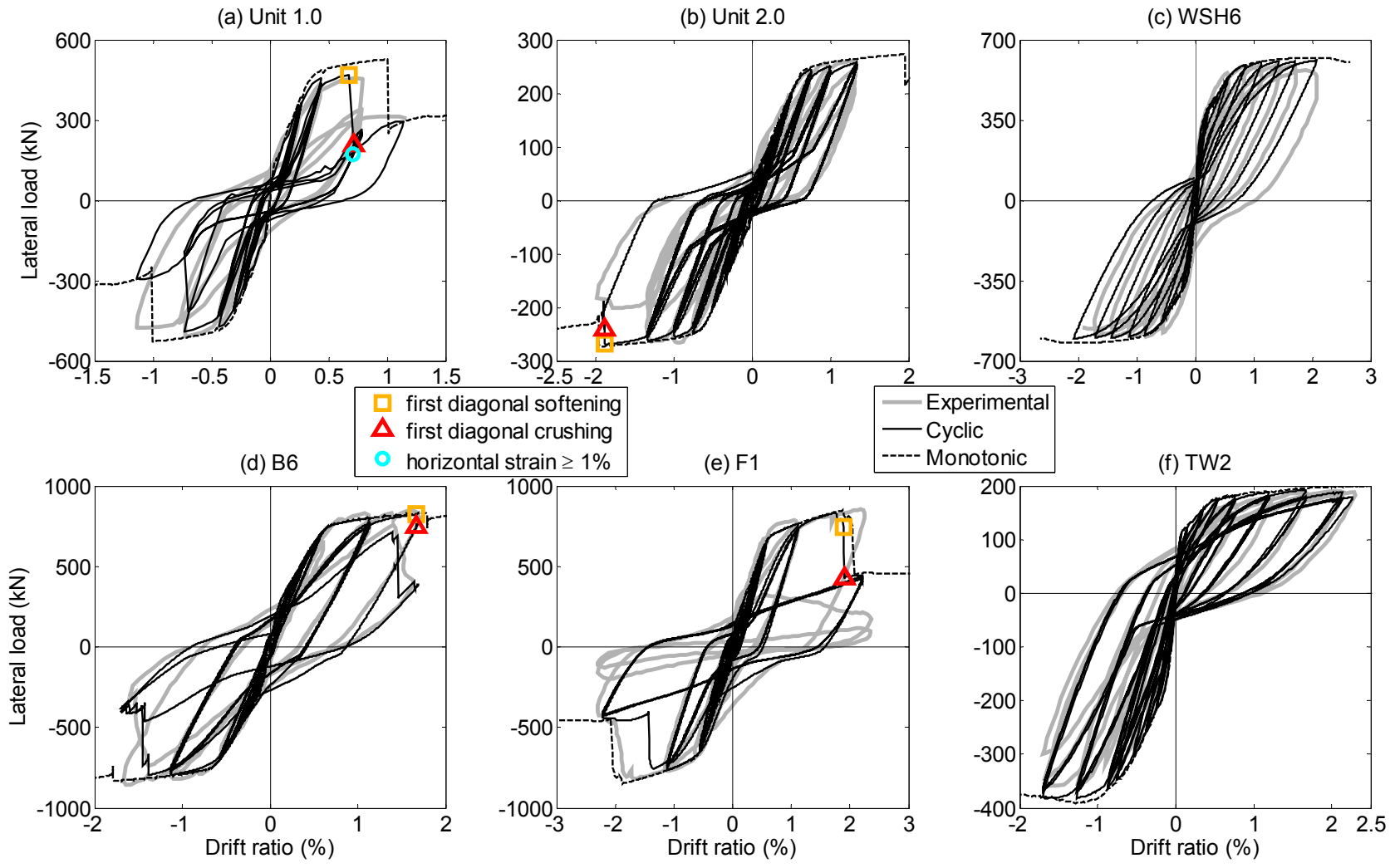


Figure 3.1 Experimentally measured and numerical computed force-drift ratio response for specimens (a) Unit 1.0, (b) Unit 2.0; (c) WSH6; (d) B6; (e) F1; and (f) TW2.

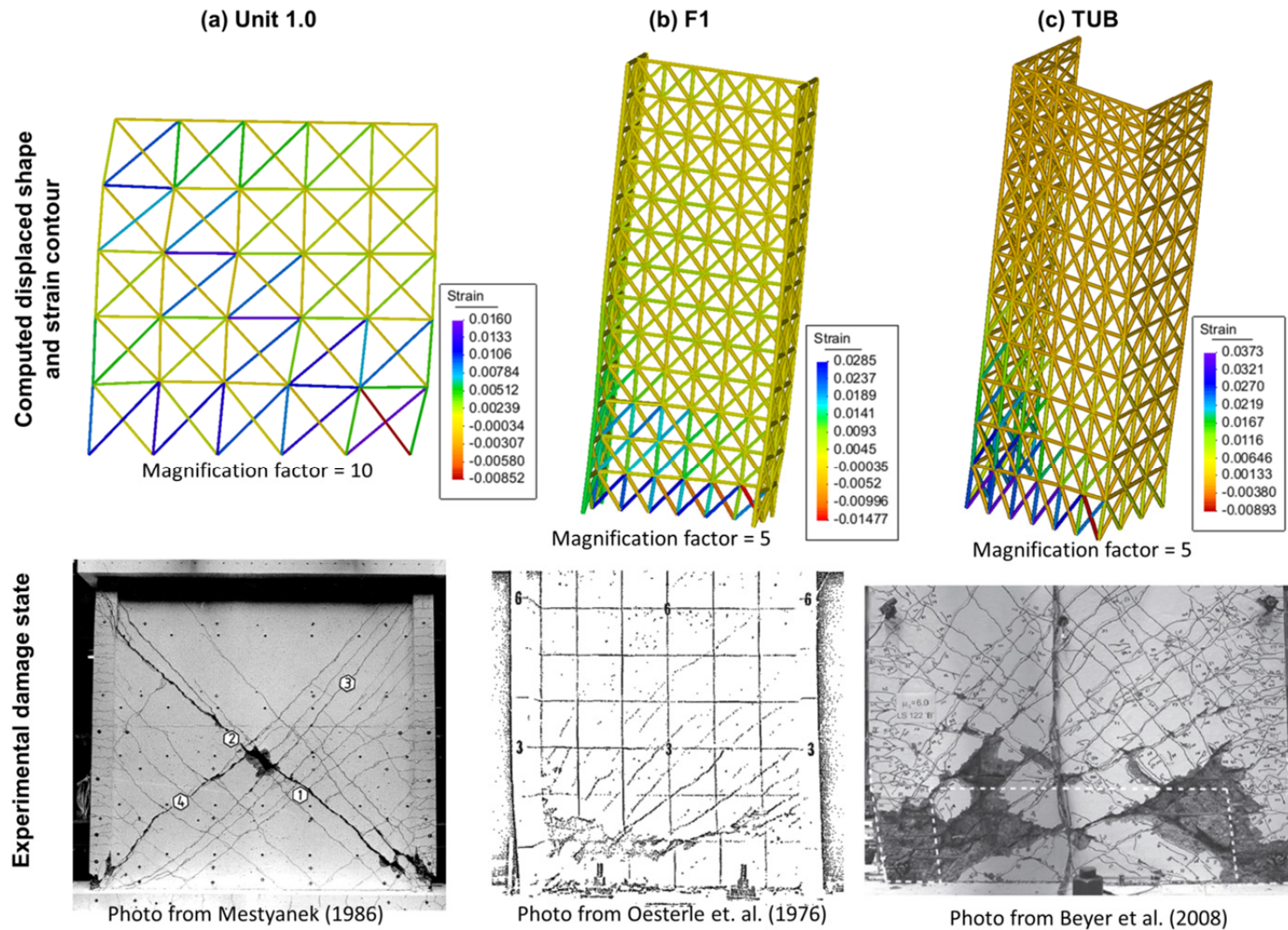


Figure 3.2 Numerically computed strain contour and deformed shape for specimens (a) Unit 1, (b) F1, and (c) TUB (E-W segment) at the point of first diagonal crushing compared to the damage state of the experimental specimen at the end of each test.

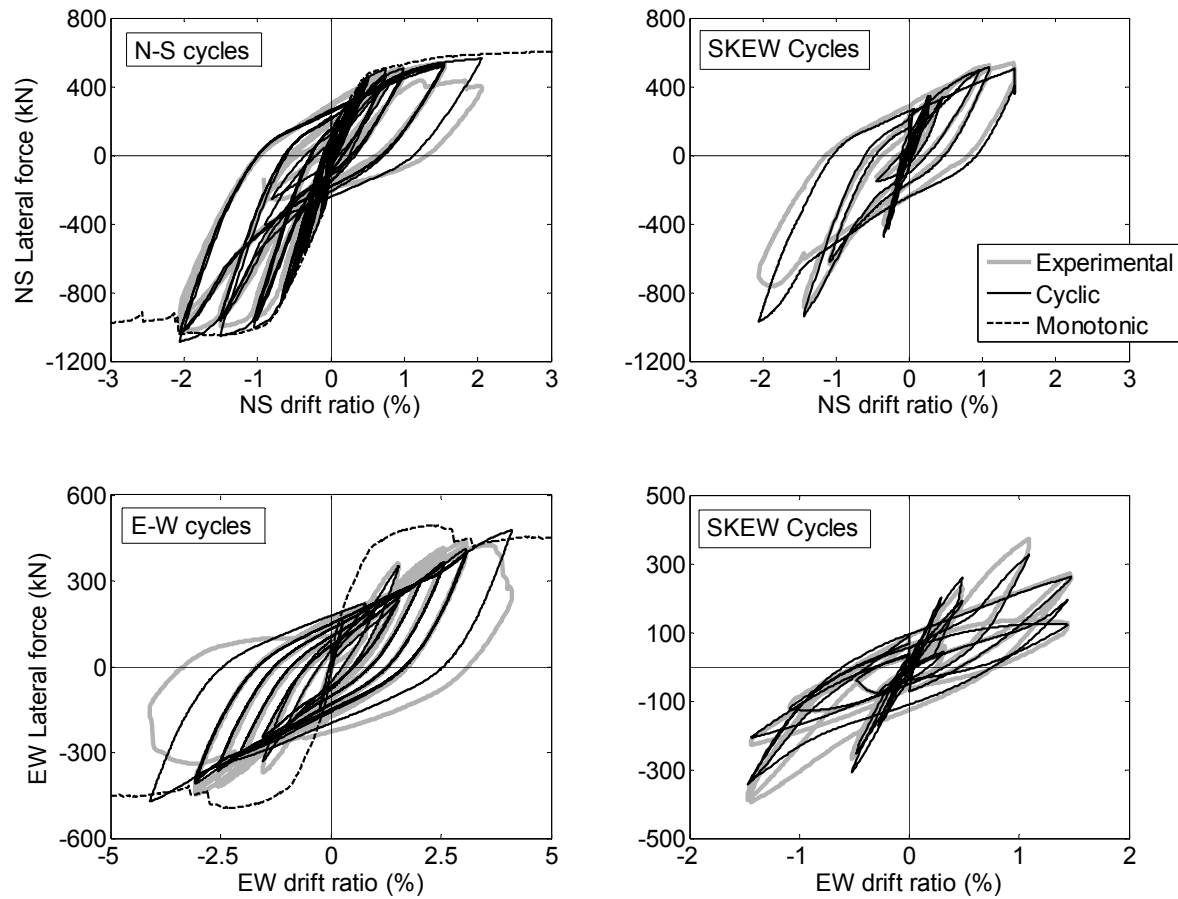


Figure 3.3 Experimentally measured and numerical computed force-drift ratio response for specimen NTW1 in the N-S, E-W, and skew cycles.

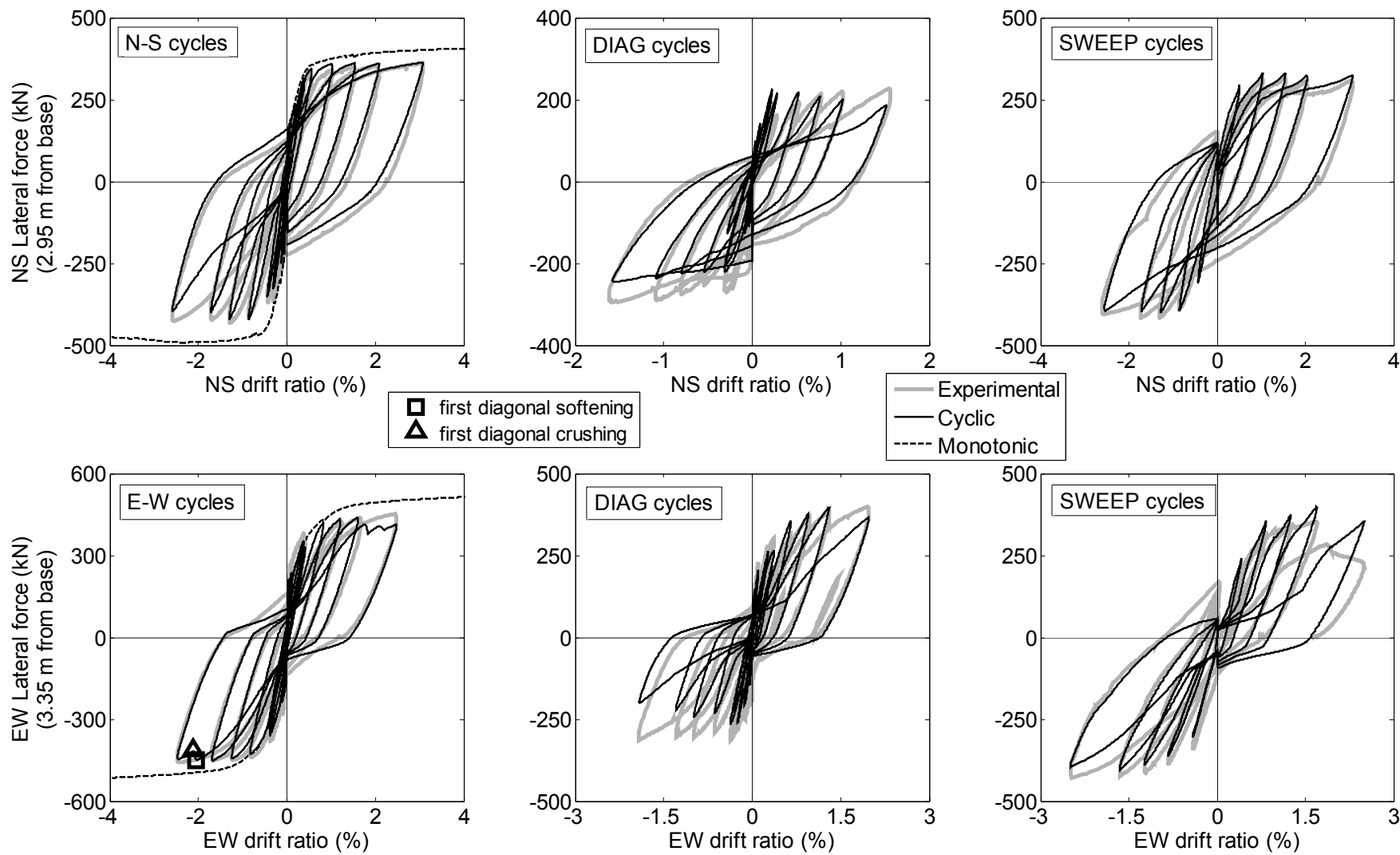


Figure 3.4 Experimentally measured and numerical computed force-drift ratio response for specimen TUB.

3.2 EFFECT OF IN-PLANE FLEXURAL RESISTANCE OF VERTICAL LINES

For the default BTM, all vertical beams (except those at the ends of each wall segment or those at the intersection of two wall segments segment) and all horizontal beams are pinned in-plane. This differs from the 2D truss model used in Panagiotou et al. [2012], which has zero in-plane flexural resistance in all vertical elements, and the beam-truss model described in Lu and Panagiotou [2008] in which all vertical lines were beams (termed BTM-beam).

Figure 3.5 shows the computed lateral force-drift ratio response for specimens Unit 1.0, Unit 2.0, and WSH6 using BTM-beam; for all walls, BTM-beam computed a peak lateral strength within 1% of that computed by the default BTM. For Unit 1.0, the failure is computed at 30% larger drift ratio than for the default BTM. The failure mode is that of diagonal crushing, but the maximum computed horizontal tension strain is 1% (compared to more than 3% computed by the BTM), and the localization of horizontal strain along the main diagonal is not as prominent. For Unit 2.0, the maximum compressive strain in the diagonals is 0.16% and diagonal crushing is not computed. Because of the in-plane flexural rigidity of the vertical beams, the BTM-beam cannot compute diagonal tension failure accurately.

Figure 3.6 shows the lateral force-drift ratio for specimens Unit 1.0, Unit 2.0, and WSH6 modeled using the truss model. The truss model computed diagonal crushing in specimen Unit 1.0 at -0.66% drift ratio (compared to 0.67% in the default BTM) after reaching -0.73% drift ratio. Compared to the default BTM, the truss model computed diagonal crushing at a 37% smaller lateral displacement for Unit 2.0. Also, the truss model computed a peak lateral strength 5%, 14%, and 4% less than that computed by the default BTM. The beam elements at the ends of the wall section allow the BTM to account for the flexural strength of the confined boundary element, which is important for computing accurately the strength and drift ratio at onset of failure.

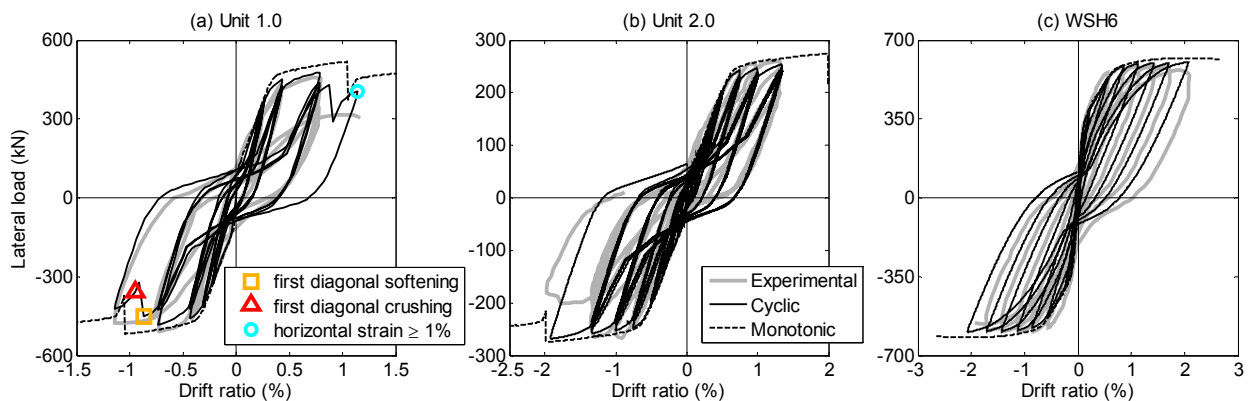


Figure 3.5 Experimentally measured and numerically computed lateral force-displacement response for specimens (a) Unit 1.0, (b) Unit 2.0, and (c) WSH6 with in-plane flexural rigidity in all vertical lines of the BTM.

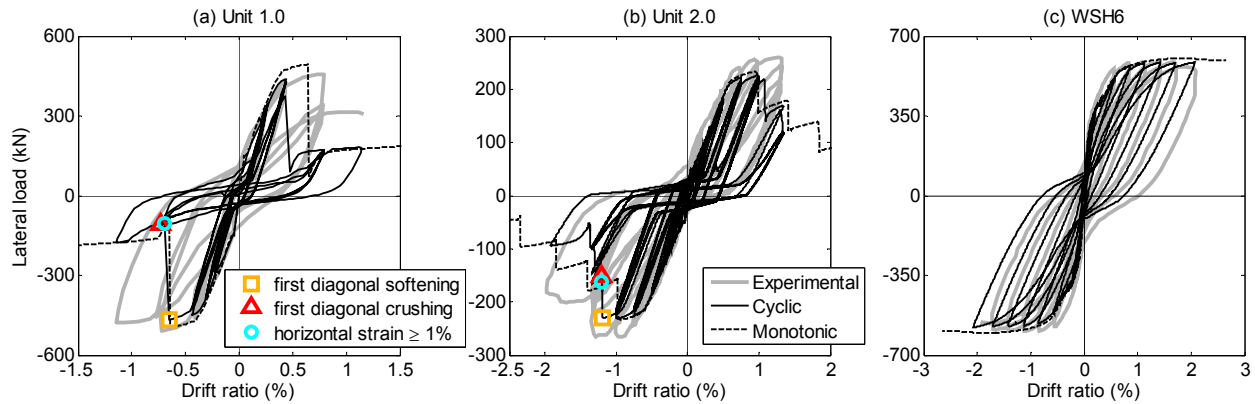


Figure 3.6 Experimentally measured and numerically computed lateral force-displacement response for specimens (a) Unit 1.0, (b) Unit 2.0, and (c) WSH6 with truss model (zero in-plane flexural resistance in all vertical elements).

3.3 EFFECT OF CONCRETE TENSION IN HORIZONTAL ELEMENTS

This section discusses the effects of modeling the horizontal concrete tension resistance and aggregate interlock (per Moharrami et al. [2014]) for three of the walls. BTMs including these effects of horizontal concrete in tension and aggregate interlock per Moharrami et al. [2014] are termed BTM-HT.

Figure 3.7 shows the response of BTM-HT for Unit 1.0, F1, and TW2. For specimen Unit 1.0, BTM-HT results in a 50% increase of drift ratio at which failure occurs and a 2% increase of maximum lateral load capacity compared to the default BTM; the overestimation of secant stiffness at 0.25% drift is 11% and 21% for BTM and BTM-HT, respectively. However, for specimen F1, which also had a diagonal compression failure, BTM-HT results in less than 2% change for the maximum lateral load capacity and drift ratio, at which failure occurs compared to the default BTM; this is because the diagonal crushing failure of specimen Unit 1.0 is caused by the large horizontal strains, while the failure in specimen F1 is due to the shear deformation at the bottom corner. The BTM-HT of specimen F1 computed a 21% larger secant stiffness at 0.25% drift ratio compared to the default BTM.

For specimen TW2, BTM-HT results in no change of maximum lateral strength but computes a 15%, 12%, and 9% overestimation of strength for drift ratios of 0.5%, 0.8%, and 1.3%, respectively; the default BTM does a better job in this region with a 7%, 6%, and 7% overestimation, respectively. For both of the T-shaped section walls TW2 and NWT1 (which is not shown), BTM-HT results in overestimation of strength and stiffness for drift ratios between 0.3% and 1%, which corresponds to cracking and the point in which the nominal flexural strength is reached, respectively. In this region, the stiffness of the wall is affected by shear cracking and thus is susceptible to the issue discussed in Section 2.5.

The effect of modeling concrete tension strength and aggregate interlock in the horizontal elements depends on the behavior and the failure mode of the specimen. For example, the failure mode of Unit 1.0 is affected by the horizontal strains: modeling of the horizontal concrete tension strength and aggregate interlock reduces the horizontal strains, thus reducing the strains

normal to the compressive diagonals. This delays the onset of softening of the diagonals at the bottom corner, thereby computing the onset of failure at a larger lateral displacement compared to the default BTM. In comparison, the diagonal crushing failure for specimen F1 is compression-controlled, indicating insignificant change in the maximum lateral strength or the computed point of failure. In specimens where distributed shear cracking was observed (specimens F1 and TW2), BTM-HT computed larger stiffness and strength up to the nominal flexural strength.

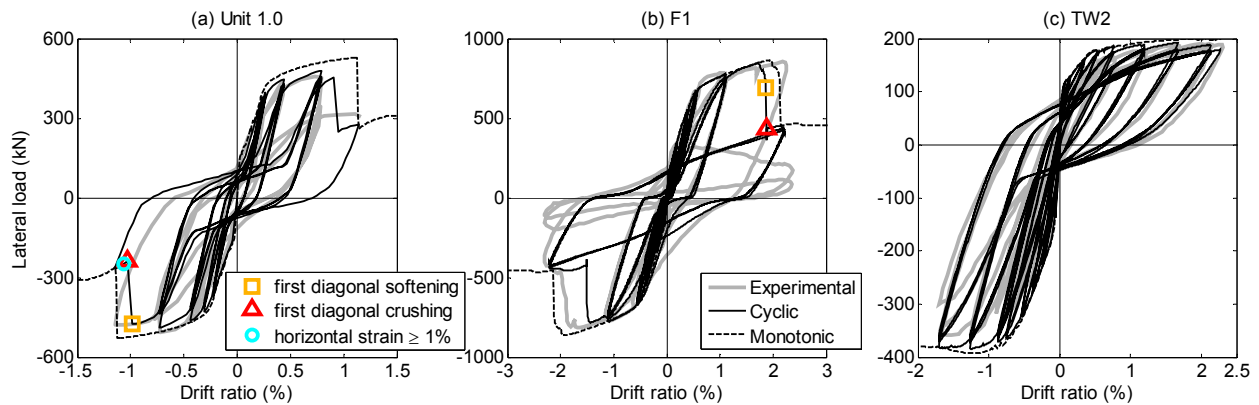


Figure 3.7 Numerically computed lateral force-displacement response for specimens (a) Unit 1.0, (b) F1, and (c) TW2 with BTM-HT that includes the horizontal concrete tension resistance and aggregate interlock model as defined in Moharrami et al. [2014] compared to experimentally measured results.

3.4 EFFECT OF INCLINATION ANGLE OF DIAGONAL ELEMENTS

This section uses specimen Unit 2.0 to highlight the importance of diagonal angle determination (as described in Section 2.4) on the computed response of a BTM. Figure 3.8 shows the experimental crack patterns of specimen Unit 2.0 [Mestyanek 1986] at 0.26% drift ratio and 1.34% drift ratio, corresponding to an applied lateral force of 120 and 241 kN (47% and 94% of the calculated nominal flexural strength of the specimen). As marked in the figure, when the specimen is at 0.26% drift, the diagonal cracks form at a 47° angle. At 1.34% drift, the diagonal cracks had fanned out, so that the steepest crack runs from the top corner to the opposing bottom corner of the specimen at a 64° angle, thus allowing the specimen to resist the entire lateral load through arch action.

The angle determination used for the default BTM (described in Section 2.4) ensures that the angle of the diagonals is such that the engaged horizontal steel can resist the shear force demand. To illustrate the importance of the diagonal angle, three BTMs for Unit 2.0 are considered: (1) Unit 2.0 BTM with a diagonal angle of 64.4°, which is the angle computed based on Section 2.4 and used in Section 3.1, (2) Unit 2.0 BTM with a diagonal angle of 56°, and (3) Unit 2.0 BTM with a diagonal angle of 44.4°, which is close to the angle that would be suggested by Moharrami et al. [2014] for this specimen. The computed force-drift ratio responses for the three BTMs are shown in Figure 3.9. The BTM with a diagonal angle of 64.4° resists the lateral force by arch action similar to what is shown for the experimental specimen at 1.34% drift in Figure 3.8(b); the BTM computes the maximum lateral force in excellent agreement with the

experimental response. The computed failure mode is crushing of the compression strut at the base, shown in the strain contour at maximum drift in Figure 3.10(a). The BTMs with 56° and 44.4° compute a maximum lateral force resistance that is dependent on the amount of horizontal reinforcement a diagonal engages. In these two models, the horizontal strains exceed 1% and the lateral force is bounded by the ultimate stress of the horizontal steel; the BTMs with 56° and 44.4° underestimate the maximum lateral force by 12% and 32%, respectively. The strain contours at maximum drift ratio are shown in Figure 3.10(b) and (c) for the BTMs with 56° and 44.4° , respectively, and both have large horizontal strains, while the BTM with 56° also computes crushing of a concrete diagonal in the last cycle. Note that modeling aggregate interlock only affects the early part of the response (less than 0.6% drift ratio) of the BTMs with 56° and 44.4° , with no change in the failure mode as shown in Figure 3.10(b) and (c).

As shown in the experimental damage patterns from specimen Unit 2.0 in Figure 3.8(c), the specimen failure was a mixture of crushing of the diagonals, kinking of boundary elements, and high horizontal strains along diagonal cracks. The failure involved diagonal cracks ranging from 45° to 64° that were formed during the loading. Because the BTM has a fixed angle determined by the diagonal compression strut, it is not possible to capture the cracks formed at lower angles; thus it is not possible to represent their effects and contributions on the diagonal tension part of the failure mode.

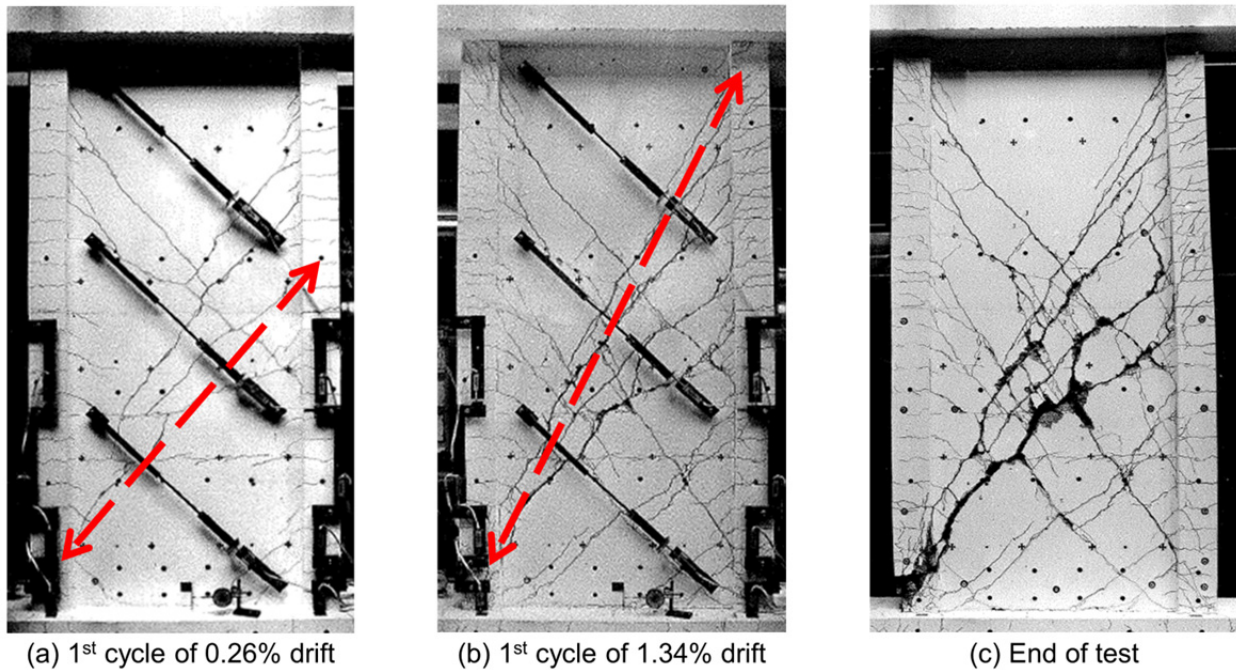


Figure 3.8 Photos of specimen Unit 2.0 (from Mestyanek [1986]) with annotations to show angle of compression struts.

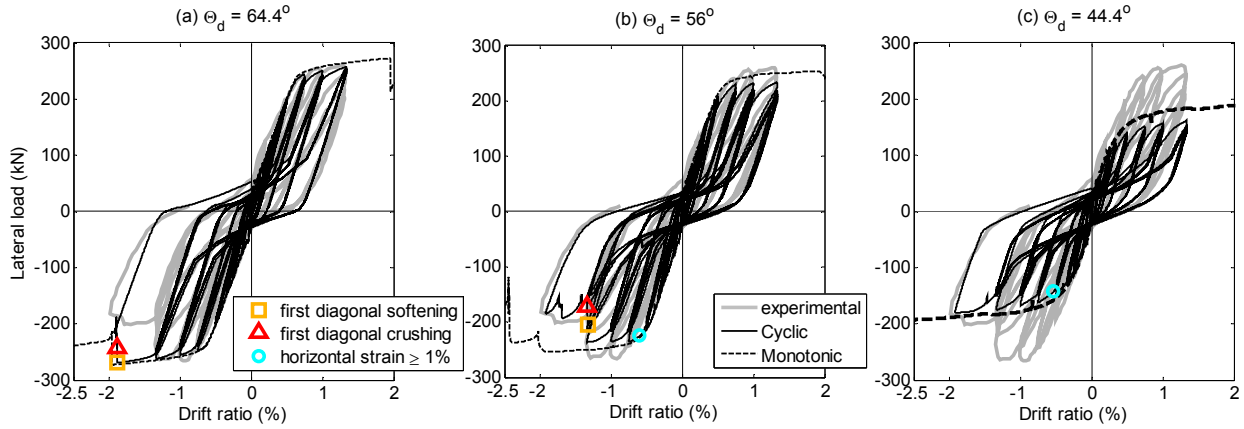


Figure 3.9 Experimentally measured and numerically computed lateral force-displacement response for specimen Unit 2.0 with diagonal angle equal to (a) 64.4°, (b) 56°, and (c) 44.4°.

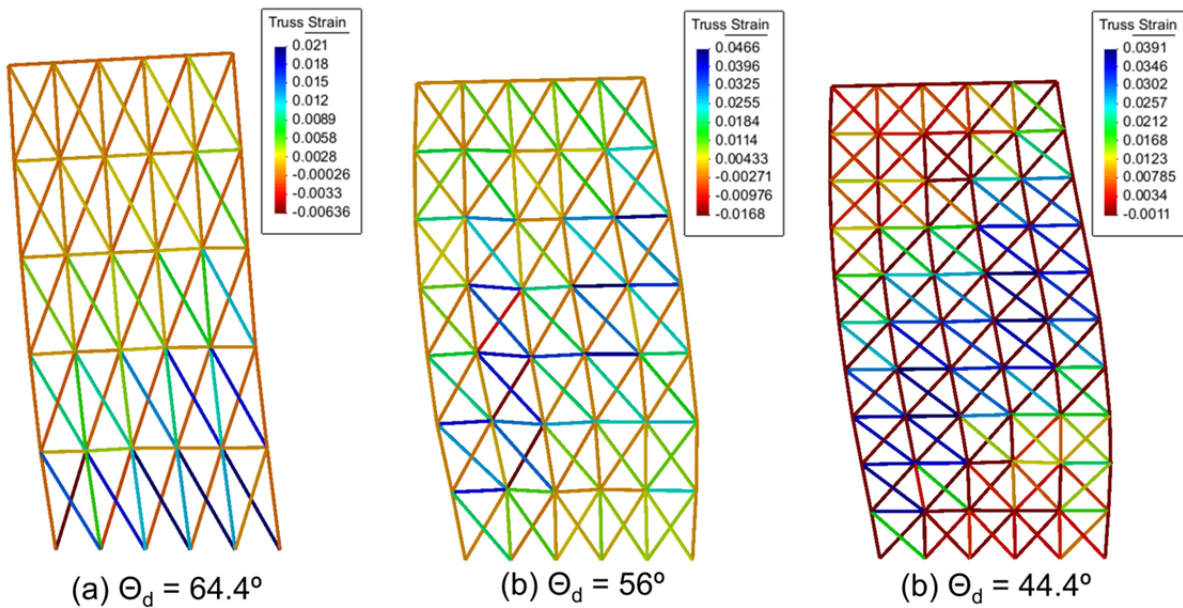


Figure 3.10 Numerically computed strain contour and deformed shape (magnification factor = 5) at -1.92% drift for specimen Unit 2.0 with diagonal angle equal to (a) 64.4°, (b) 56°, and (c) 44.4°.

3.5 MODELING OF LARGE BOUNDARY ELEMENTS

This section describes and compares two methods for modeling large boundary elements and uses specimen B6 as an example. Each boundary element in specimen B6 is a 305 × 305 mm square column with $\rho_l = 3.7\%$; the boundary element length is 16% of the total length of the wall and has three times the thickness of the web. Figure 3.11 shows two methods of representing the boundary elements of specimen B6: (a) average properties in the horizontal and diagonal elements adjacent to the boundary elements (termed BTM-avg), which is used for the results

shown in Table 3.1; and (b) rigid offsets accounting for the length of the boundary element (termed BTM-offset). In both methods, the boundary element is modeled as a single vertical line. A third method, which models the boundary element using more than one vertical line, should be used to model long boundary elements (such as in specimen TW2 at the tip of the web); this method is not discussed in this section but is used in specimens TW2 and NTW1.

Figure 3.12(a) shows the response of specimen B6 modeled without accounting for the width of the boundary elements in the diagonal and horizontal elements: all of the diagonal and horizontal elements have the thickness and material properties of the web (termed BTM-web). Figure 3.12(b) and (c) shows the response of specimen B6 modeled with BTM-avg and BTM-offset, respectively. All three models compute nearly identical response up to 1% drift and are in good agreement with the experimental response up to that point.

BTM-web computes the softening and crushing of the concrete diagonal at the base of the wall at 1% drift ratio with less than 6% loss of lateral load capacity during that cycle. The diagonal crushing propagates upward vertically during the cycle with 1.7% max drift ratio, resulting in further degradation of the lateral strength of the model. BTM-avg computes the crushing of the diagonal during the first cycle with 1.7% max drift ratio but immediately reverses without significant strength degradation in the positive direction. At -1.4% drift ratio, BTM-avg fails due to diagonal crushing, which propagates vertically up the wall adjacent to the boundary elements, resulting in a loss of more than 50% of lateral load capacity. BTM-avg computes the crushing of the diagonal at 1.6% drift ratio along with vertical propagation of the diagonal crushing, resulting in more than a loss of more than 50% of lateral load capacity during the first cycle at 1.7% max drift ratio. Figure 3.13 shows the strain contour of the three BTMs at the second cycle of 1.7% maximum drift ratio compared to the damage state of the experimental specimen at the same point; all three models agree well with the experimentally observed failure mode. BTM-avg and BTM-off predict the point of failure in good agreement with the experimental results.

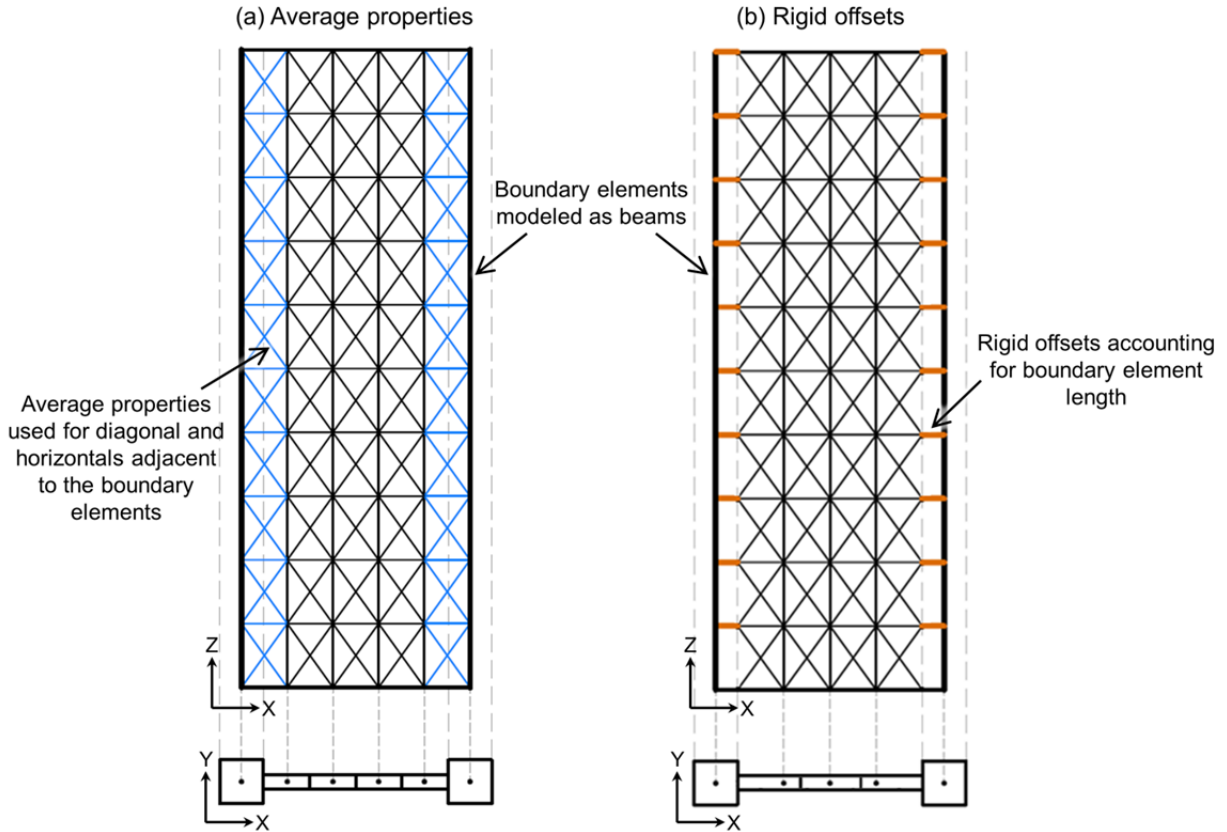


Figure 3.11 Elevation and cross-section views of two methods for modeling specimen B6: (a) average properties and (b) rigid offsets.

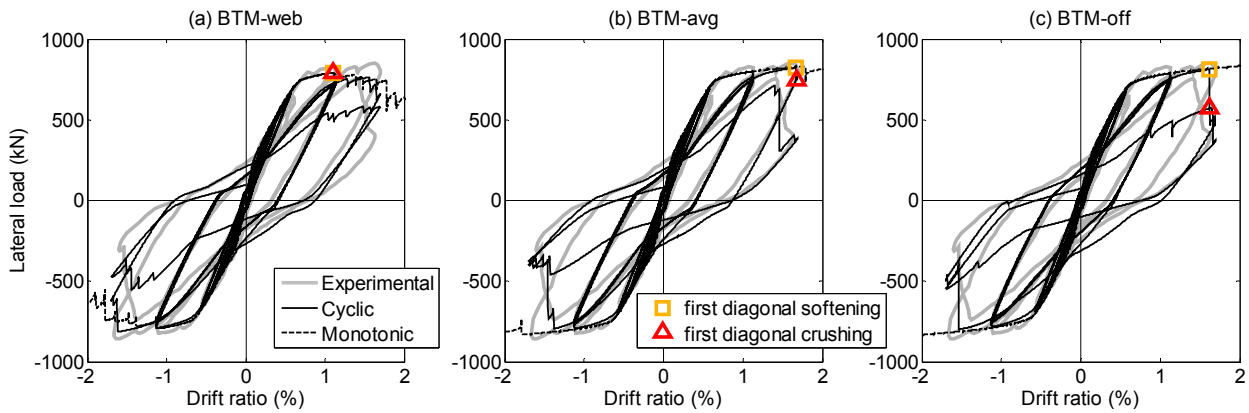


Figure 3.12 Experimentally measured and numerically computed lateral force-displacement response for specimen B6 modeled with (a) without considering the width of the boundary elements; (b) with average properties for the width of the boundary elements; and (c) with rigid offsets of the boundary elements.

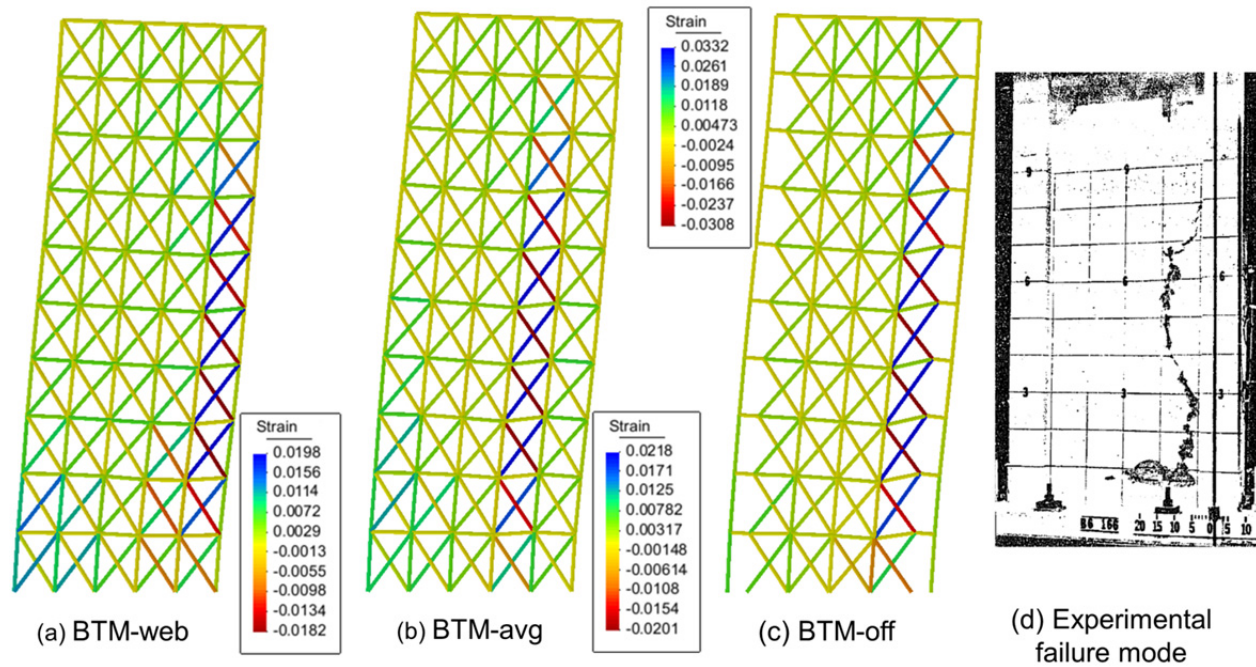


Figure 3.13 Numerically computed strain contour and deformed shape (magnification factor = 5) at the second cycle of 1.7% drift for specimen B6 modeled with (a) BTM-web, (b) BTM-avg, and (c) BTM-off, compared to (d) the experimental failure mode at the end of the test.

4 Beam-Truss Model for Slabs

In this section, the beam-truss model for slabs is presented. The response computed using the BTM is compared with the experimentally measured response of a column-slab specimen, shown in Figure 4.1. The BTM for slabs consists of beam elements without in-plane flexural rigidity (pinned in plane) running in the two principal horizontal directions of the slab, with diagonal truss elements in each of the panels formed by the beams. The beams in the longitudinal directions model the concrete and steel included in the section areas each element represents, while the diagonal trusses model the diagonal compression field of concrete. Tension stiffening is modeled in both principal horizontal directions. The effect of aggregate interlock is not modeled for RC slabs. The lateral load resistance in and out of the plane is identical to that for a wall segment of a RC wall. Confined edge beams in the slab, such as that shown in Figure 4.1(a), are modeled similarly to the boundary elements of the RC walls considered in the previous chapters. For the slab BTM, the torsional rigidity of each beam is modeled as bilinear-perfectly-plastic, with the gross elastic torsional stiffness up to the torsional cracking strength as calculated based on the space truss model for torsion [Park and Paulay 1975]. Modeling torsional softening in the confined edge beam through calibrating strength degradation in the torsion-twist relation for the beam elements is beyond the scope of this section.

Specimen 2C [Robertson 1990] is a two bay slab-column specimen consisting of a $6\text{ m} \times 2\text{ m}$ slab, 0.11-m-thick, supported on three columns along the long direction of the specimen; see Figure 4.1(a). The 0.25-m-square columns are 1.5 m tall, and the slabs are connected mid-height of each column; the columns are pinned at the base and top and connected to a loading assembly that applies the same displacement to the top of all three columns. The columns were designed to remain nominally elastic during the entire test. The longitudinal steel ratio at the top and the bottom of the slab was 1% in both directions. Extra reinforcement was used in the x -direction for the strip of the slab surrounding the columns, as well as in the y -direction for the strip of the slab surrounding the center column. At the ends of the slab in the y -direction, confined edge beams are used to enhance torsional resistance; see Figure 4.1(a). A gravity load of 80 kN is applied uniformly by suspending weights from the slab, and the specimen is loaded cyclically in the x -direction. Figure 4.2 shows the experimental applied lateral load and drift (defined as the displacement at the top of the column divided by the height of the column). The experimental test included a cycle at 5% drift ratio, which was not included in Figure 4.2 because this cycle was dominated by a torsional failure of the confined edge beams, which was not modeled.

Figure 4.1(b) shows the BTM constructed for specimen 2C; a $0.25\text{-m} \times 0.25\text{-m}$ square mesh is used for the model. Each column is modeled using an elastic beam element using 50% of the column gross section flexural rigidity. The width of the column is modeled using rigid offsets connected to the slab BTM.

Figure 4.2(a) shows the numerically computed lateral force-drift ratio response for the slab BTM in which no bond slip/strain penetration is modeled. The computed strength is in excellent agreement with the experimental results, but the computed hysteretic behavior shows more energy dissipation and less pinching than the experimental results. Figure 4.2(b) shows the computed results when the effect of strain penetration is modeled at the interfaces between the columns and slab BTM. The strain penetration is modeled using a zero length element with the same section properties as the adjacent beam, except the steel in the section is replaced with a bond slip material. The bond slip material has a stress-deformation envelope equivalent to that of the steel material with a length of 13 cm (based on a strain profile linearly decreasing to zero strain over the width of the column); the hysteretic behavior of bond slip material includes pinching (pinching parameters 0.4 and 0.2 in the *Hysteretic* material of Opensees, as shown in Figure 4.3). In comparison to the BTM with perfect bond, the maximum lateral load resistance computed by the BTM with strain penetration for the column interfaces differs less than 2%; however, the BTM with strain penetration computes more pinching in the hysteretic response and better agrees with the experimental results in terms of hysteretic energy dissipation.

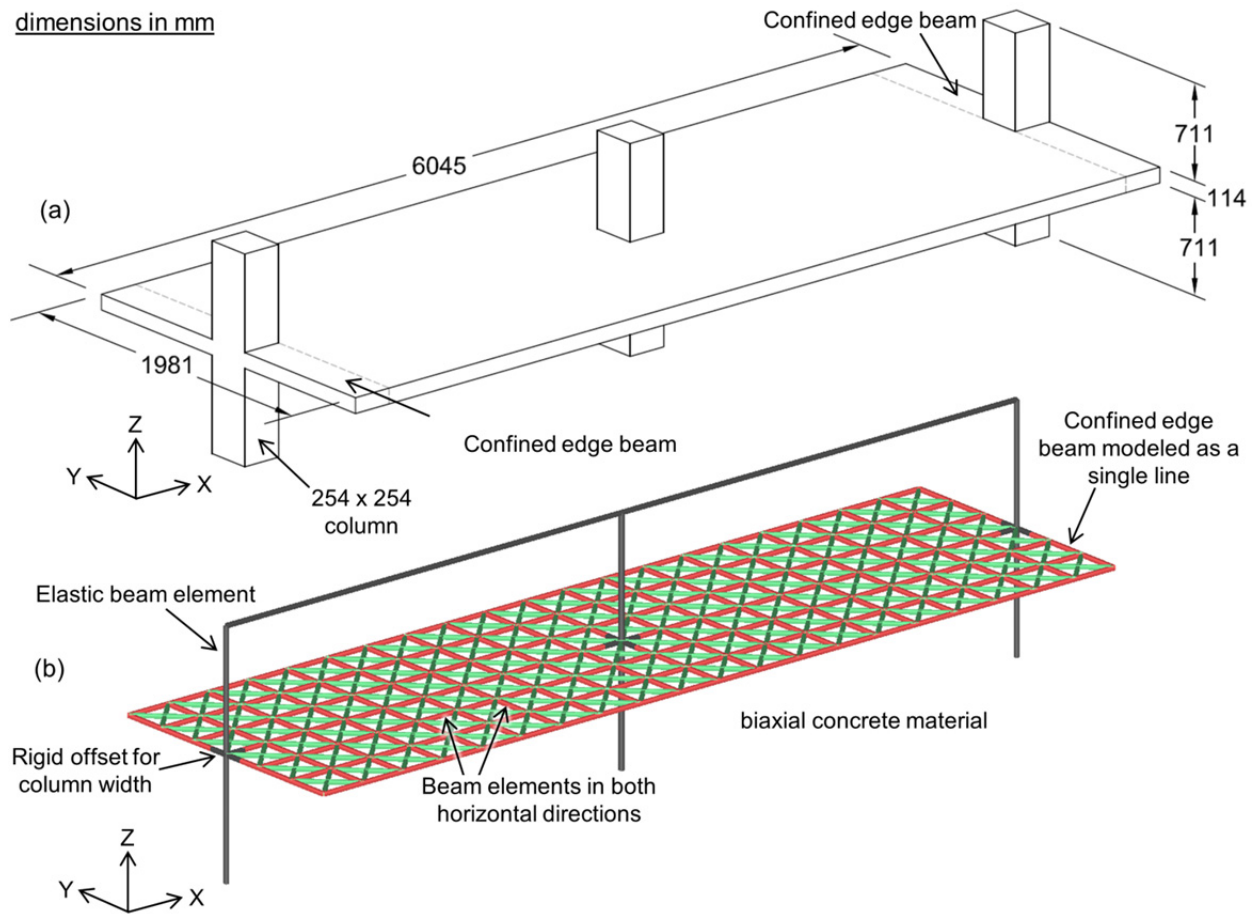


Figure 4.1 (a) Three-dimensional view and dimensions of the column-slab specimen 2C [Robertson 1990] and (b) the corresponding BTM for the specimen.

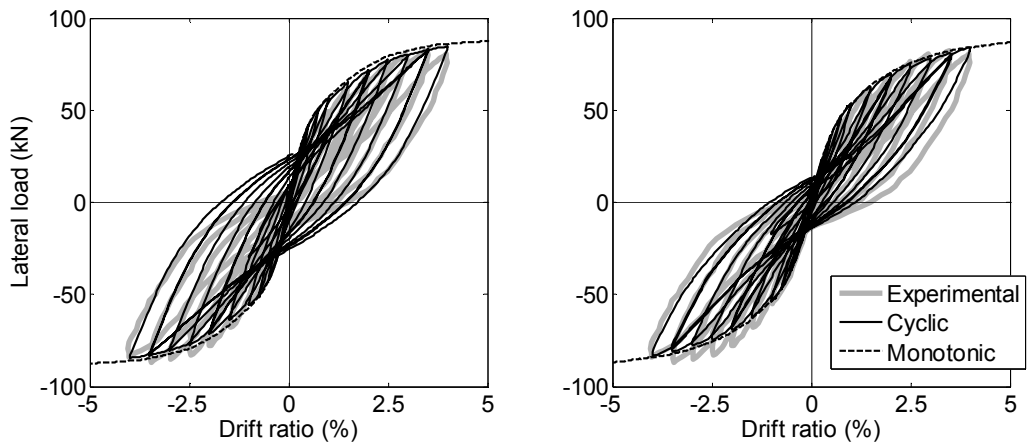


Figure 4.2 Experimentally measured and numerically computed lateral force-displacement response for column-slab specimen 2C with (a) perfect bond and (b) strain penetration modeled at the column-slab interface.

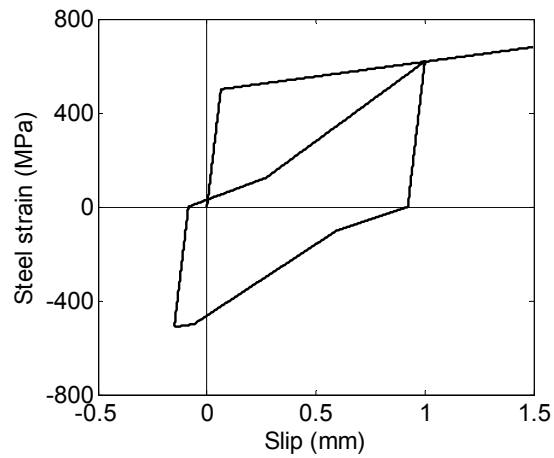


Figure 4.3 Hysteretic behavior of bond slip material including pinching.

5 Validation for a 5-Story Coupled Wall subjected to Tri-Axial Base Excitations

5.1 SPECIMEN OVERVIEW

This section presents a case study of specimen SLO, a 5-story reinforced concrete wall building slice, tested at LNEC, Lisbon, Portugal, within the Project ECOLEADER-LIS [Kante 2005; Coelho et al. 2006]. Figure 5.1(a) shows the elevation view of the specimen: the specimen consists of two coupled T-shaped walls, joined by a coupling beam to form an H-shaped section at each of the five floors. The height of each floor is 0.9 m. The two wall segments parallel to the x -direction (termed the flanges) are 1.6 m long and 0.06 m thick; the coupled wall segment parallel to the y -direction (termed the web) is 1.44 m long and 0.06 m wide, with an opening 0.27 m tall and 0.67 m wide in the center of the wall segment. Each floor has a 1.6×1.56 m slab that is 0.08 m thick. Figure 5.1(c) and (d) show the details of the coupling beams and the wall section, respectively. The average longitudinal reinforcement ratio for the coupled walls is 0.42%; away from the ends of the wall segments, the walls have a longitudinal and reinforcing ratio of 0.24% in all wall segments. The slab has a confined edge beam on each of the free edges; the reader is referred to Kante [2005] for reinforcing details for the slab. The walls had a concrete compressive strength of 38.8 MPa on average (measured with standard prescribed cube). The 3mm diameter reinforcing steel used in the wall was a steel wire with low ductility (yield strength $f_y = 786$ MPa, ultimate strength $f_u = 826$ MPa, and failure strain $\epsilon_u = 1.5\%$), while the 6 mm reinforcing steel had $f_y = 483$ MPa, $f_u = 631$ MPa, and $\epsilon_u = 8.8\%$. The weight of the specimen is 58.1 kN per floor, of which 48 kN is applied through metallic masses placed on the slabs of each floor, shown in Figure 5.1(c). The slab on each side of the wall carried a mass block with dimensions of 0.84 m \times 0.84 m, with a total thickness of 0.6m (0.3m above and below the slab). The specimen has an axial load ratio of 3.1%.

The specimen was subjected to six triaxial ground motions (T1 through T6) of increasing intensity. After ground motion T4, Kante [2005] reports only minor cracking in the flange and no damage in the web; up to that point, the wall has attained a maximum drift ratio of 0.24% and 0.08% in the x - and y -directions, respectively. Ground motion T5 had peak ground acceleration (PGA) equal to 0.42g and 0.73g and resulted in a maximum roof drift ratio of 0.32% and 0.29% in the x - and y -directions, respectively. During ground motion T5, shear cracks opened up in the web near the opening, and further cracking in the flanges was observed. Ground motion 6 had PGA of 0.52g and 1.02g, and resulted in a maximum roof drift ratio of 0.60% and 0.77% in the x - and y -directions, respectively; the base shear and roof drift ratio response time history for this motion is shown in Figure 5.2. In ground motion T6, the web sustained a diagonal shear failure, which resulted in the web punching through part of the flange at the corner of the web and

fracture of at least two horizontal reinforcing bars in the web; see Figure 5.3. Also, one of the edges of the flange crushed in the vertical direction. No damage was observed in the coupling beams, shown in Figure 5.3(b).

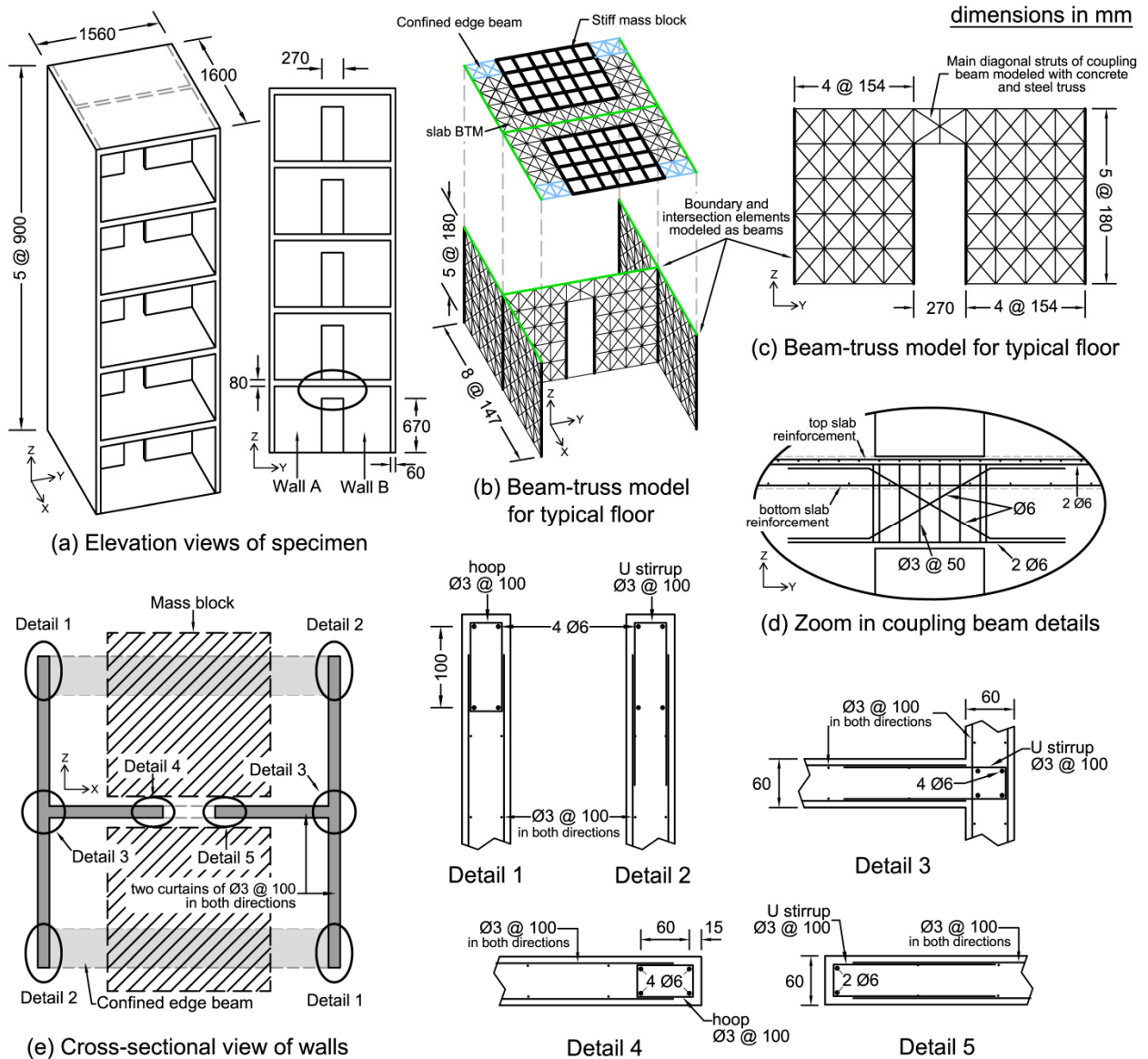


Figure 5.1 Description of 5-story coupled wall specimen SLO and beam-truss model.

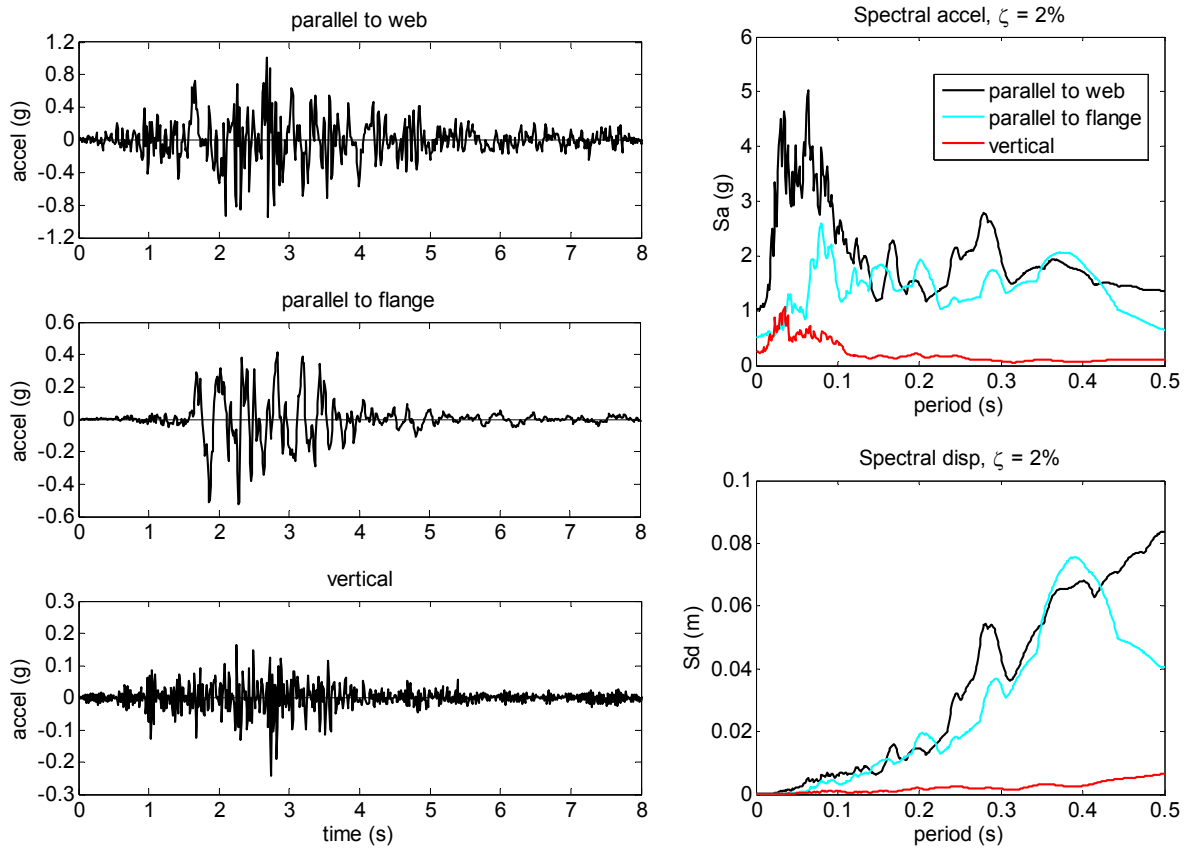


Figure 5.2 Recorded acceleration time history of the shaking table in the three directions during ground motion T6.

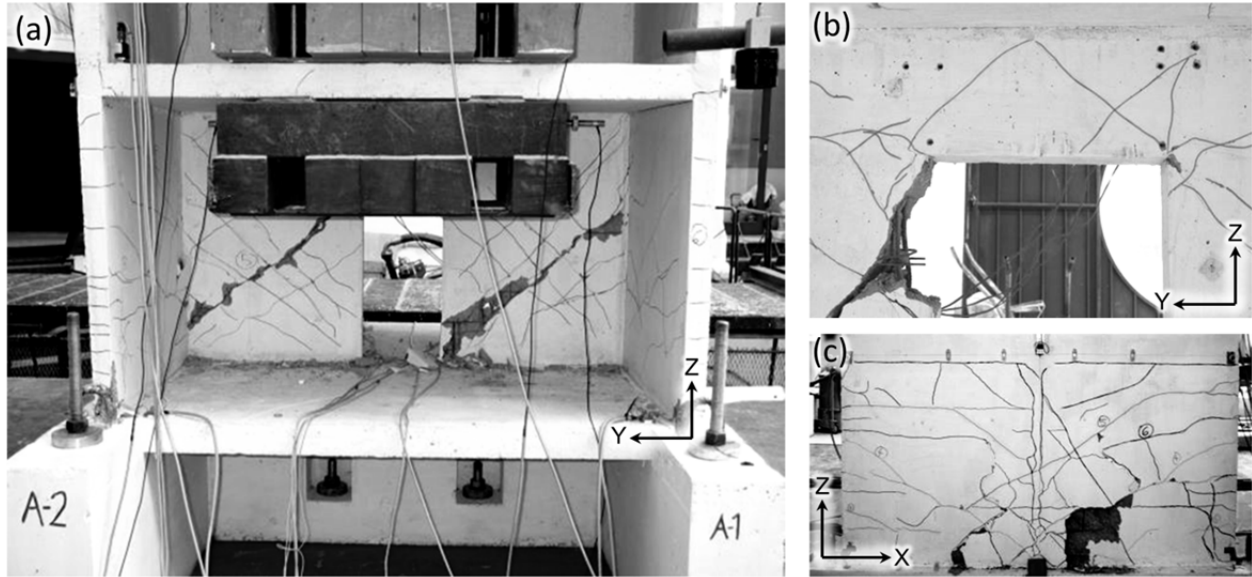


Figure 5.3 Damage pattern of the bottom floor (a) web and (b) coupling beam (viewed from the negative x direction) and (c) flange in the negative y direction after ground motion T6 (from Coelho et al. [2006]).

5.2 DETERMINATION OF BEAM-TRUSS MODEL FOR SPECIMEN SLO

The BTM of the coupled wall specimen SLO consists of eleven vertical lines in each of the flanges and five vertical lines in each of the two parts of the web, shown in Figure 5.1(b) and (c), resulting in a total of thirty vertical lines at the base. Each vertical line in the flanges, including the line at the intersection of the flange and web, represents a cross-sectional area of $17.8 \text{ cm} \times 6 \text{ cm}$ and the corresponding steel area. The two vertical lines of the web immediately adjacent to the coupling beam represents a cross-sectional area of $9 \text{ cm} \times 6 \text{ cm}$ and the corresponding steel as described in Details 4 and 5, while the remaining cross-sectional area is represented equally among the six vertical lines representing the web (the intersection line is excluded). The coupling beam is modeled with a pair of crossing diagonals representing the diagonal reinforcement in the beam and diagonal concrete compressive struts with an area of $16.7 \text{ cm} \times 6 \text{ cm}$, calculated based on Figure 2.1(g) for the representative panel. A model with a finer mesh in the bottom story is discussed in the following sections; the mesh size is found to have minimal impact on the global response and the peak strains of the coupling beam. The vertical reinforcement of the coupling beam is modeled in the two vertical elements at the end of the coupling beam as well as the one in the middle. The slab at each level is modeled using the beam-truss model for slabs described in Chapter 4. Confined edge beams along the free edge of the slab are modeled with two lines parallel to the y -direction, shown in blue in Figure 5.1(b). Because the metallic masses placed on the slab are stiff and cover a large portion of the slab, the portion of the slab covered by the masses are modeled as linear elastic with the appropriate stiffness and mass; see Figure 5.1(b). The elements in the intersection between the wall and the slab, shown in green color in Figure 5.1(b), have flexural rigidity in both directions; note that, because the element sections are not large, removing the flexural rigidity does not effect the global results.

A concrete compressive strength of 38.8 MPa was measured with standard prescribed cube tests, so the compressive strength for a standard cylinder f'_c is assumed to be 34.8 MPa. The

reinforcing steel is modeled as per Section 2.2; the effect of rupture for the low ductility 3-mm-diameter reinforcing steel wire is only modeled and discussed in Section 5.7.

To determine the angle of the diagonals, the nominal moment M_n is calculated for one T-section wall for bending about the x - and y -axis (assuming half of the gravity load is resisted by each wall): $M_{n,fl} = 400$ kN-m for bending around the y -axis, and $M_{n,w+} = 251$ and $M_{n,w-} = 75$ kN-m for bending around the x -axis with the flange in tension and flange in compression, respectively. The shear force associated with M_n due to first mode of response for all directions of bending is used; the first mode effective height $h_{eff,1} = 3.6$ m (80% of the total height). For bending around the y -axis, the specimen is considered uniform over the height, and a diagonal angle of 37° for the flanges is computed based on $1.2M_{n,fl}$; a diagonal angle of 45° is the minimum suggested and, in the specimen presented, a diagonal angle of 50.8° is used in the flange to achieve a nearly square mesh for the slab. The response of a model with a diagonal angle of 45° in the flange was found to result in very similar response to that from a model with a diagonal angle of 50.8° . Note that, for loading in the y -direction where the coupled wall is engaged, the coupling beam transfers a compressive force to the wall with the flange in compression and tensile force to the wall with flange in tension; see Figure 5.4(a).

The shear force transferred by one diagonally reinforced coupling beam is estimated [using Equation (2.4)] to be $V_{cpl} = 52$ kN without accounting for the slab. While the effective flange cannot be determined accurately, an effective flange width of 1.34 m (8 times the thickness of the slab on each side of the beam) is used as an upper bound estimate, resulting in $V_{cpl} = 219$ kN. For the case without slab contribution, this results in base shear due to the bottommost coupling beam of $V_{b,cpl} = 38$ kN and 146 kN, respectively. $V_{b,cpl} \geq (M_{n,w-}) \cdot (h_{eff,1})$ for the wall compression wall regardless of slab contribution; therefore, the wall assumed to be strongly coupled. Due to the level of coupling here, the compression wall is expected to resist the majority of the total shear force despite that its flange is in compression. This is confirmed in Section 5.4: the tension wall resists a peak shear force of 76 kN, which results in a minimum diagonal angle of 47.5° [from Equation (2.1)]. For the case of strong coupling, the struts are controlled by location of the compression region of the bottommost coupling beam. Figure 5.4(b) and (c) show the strut-and-tie diagram and BTM for the web accounting for that load path. The diagonal angle is 49.5° , which allows for a direct strut between the compression zone of the coupling beam to the compression zone of the wall.

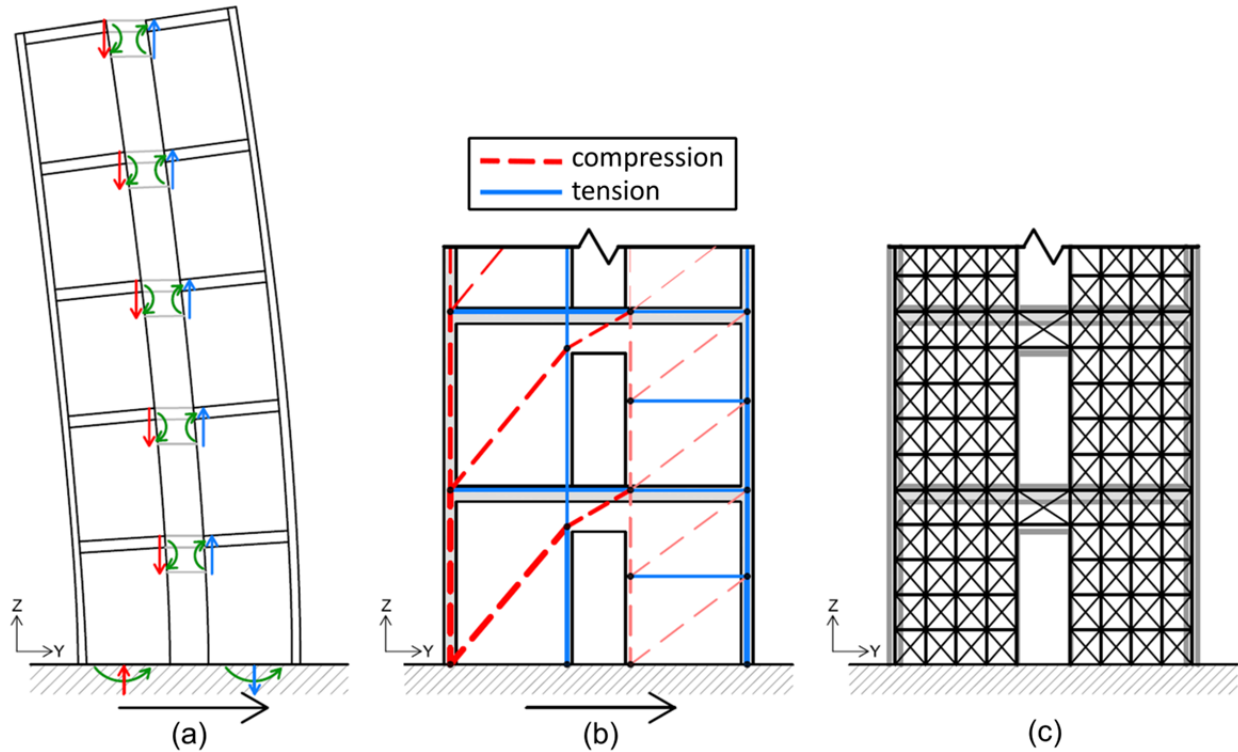


Figure 5.4 (a) Coupling beam forces on the walls and resulting reaction at the base for roof drift in the negative y direction; (b) strut-and-tie model for coupled wall of specimen SLO showing the predicted load path for lateral load in the y -direction; and (c) resulting beam-truss model for the coupled wall accounting for geometric constraints.

5.3 BTM RESULTS

The experimental specimen was tested using a sequence of six triaxial ground motions with increasing intensity of which only the first five ground motions resulted in nominally elastic behavior of the specimen (0.32% and 0.29% peak drift ratio in the x - and y -directions, respectively). For the analysis presented here, the effects of the first five ground motions T1–T5 were approximately considered by subjecting the BTM to a static cyclic displacement history, shown in Figure 5.5, with peak drift equal to that observed during ground motion T5 in the experimental specimen: 0.29% roof drift ratio parallel to the web and 0.32% roof drift ratio parallel to the flange. For these cycles, each direction is loaded independently, and load is applied in an inverse triangle distribution to each of the floors' slabs, while the roof drift ratio is maintained using displacement-controlled analysis. Following these static cycles, the model was subjected to the triaxial base excitation T6, shown in Figure 5.2.

Table 5.1 lists the experimentally measured and computed structural periods for 5-story specimen in each of the two principal directions. The BTM computed the initial structural periods to be much stiffer than observed experimentally; however, the computed values are in good agreement with that computed using the multiple-vertical-line-element macro model in Coelho et al. [2006]. Coelho et al. [2006] attribute the discrepancy to initial cracking in the specimen due to being hit by the crane during construction. After the static loading cycles, the

BTM computed the structural period to be 26% greater in the flange direction and 66% greater in the web direction. The period of the BTM after ground motion T6 is computed after the structure reaches static equilibrium; the large period in the web direction reflects the damaged state of the BTM.

Figure 5.6 shows the experimentally recorded and numerically computed base shear force and roof drift ratio response histories for ground motion T6; Figure 5.7 shows the corresponding hysteretic loops in the x - and y -directions. The numerically computed base shear force agrees well with that recorded experimentally. Although the BTM overestimates peak roof displacement in the flange direction, the agreement for the web direction is excellent. The overestimation of displacement in the flange direction is especially pronounced from $t = 3$ -4 sec and after 6 sec. This may have been due to a flexible or underdamped torsional mode or the underestimation of lateral strength under skew loading (shown for specimens NTW1 and TUB in Chapter 3).

Softening of a concrete diagonals in compression first occurs in the bottom corner of the web at $t = 3.26$ sec and is quickly followed by crushing of the same diagonal and localization of horizontal tension strains along a diagonal band (diagonal tension failure) in Wall B; Figure 5.7 shows a drop of base shear force when the softening and crushing of the diagonal occur. The strain contour at $t = 3.3$ sec, which is the point of peak drift ratio during the cycle where diagonal crushing is computed, is shown in Figure 5.8 along with the diagonal tension failure. The computed failure mode agrees well with the experimentally observed failure shown in Figure 5.3(a). While the BTM does not model punching failure of walls explicitly, the displaced shape shows significant bulging near the crushed diagonal, reflecting the experimentally observed punching failure in the flange shown in Figure 5.3(c). The BTM computes a nominally elastic response of the coupling beams, which is in good agreement with the experimentally observed lack of damage in the coupling beams.

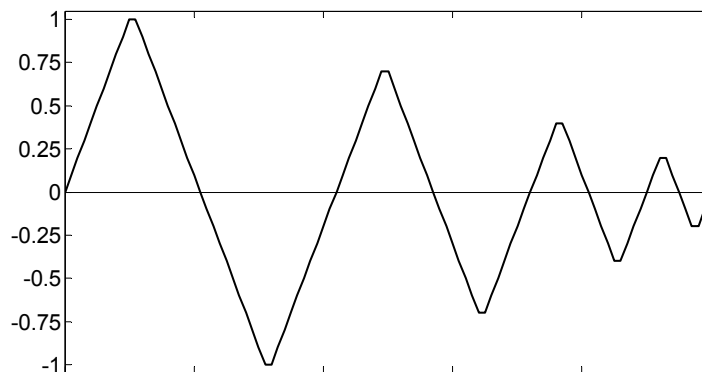


Figure 5.5 Statically imposed displacement history (normalized to peak displacement) used to simulate damage from ground motions T1 to T5.

Table 5.1 Experimentally recorded and numerically computed periods of translational modes for 5-story specimen SLO.

	Wall segment	Experimentally recorded period (s)		BTM period (s)		BTM-HT period (s)		BTM-fineMesh period (s)	
		1 st mode	2 nd mode	1 st mode	2 nd mode	1 st mode	2 nd mode	1 st mode	2 nd mode
Before S1	Flange	0.167	-	0.101	0.024	0.093	0.023	0.099	0.022
	Web	0.141	0.032	0.095	0.022	0.080	0.020	0.096	0.024
Before T6	Flange	0.244	-	0.306	0.068	0.316	0.072	0.296	0.068
	Web	0.213	0.045	0.350	0.059	0.333	0.052	0.348	0.058
After T6	Flange	0.262	-	0.480	0.123	0.473	0.120	0.473	0.121
	Web	0.44	0.095	0.578	0.098	0.547	0.082	0.590	0.095

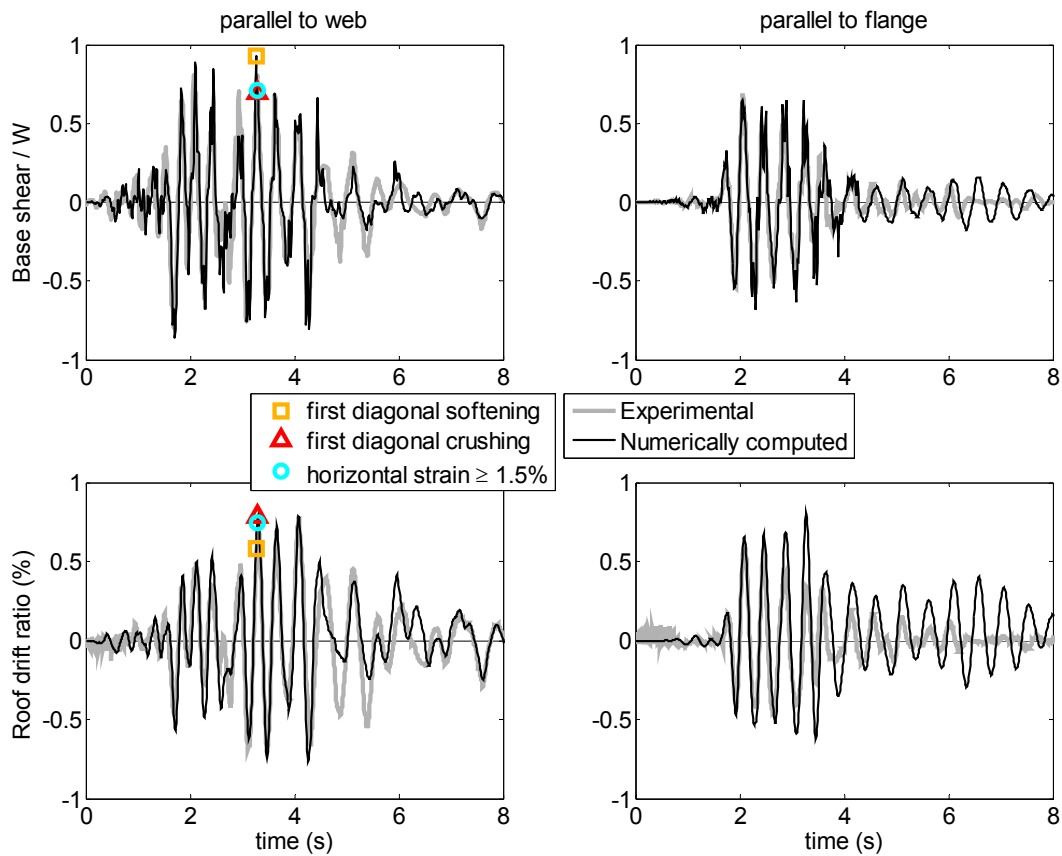


Figure 5.6 Experimentally measured and numerically computed base shear force and roof drift response histories for ground motion T6.

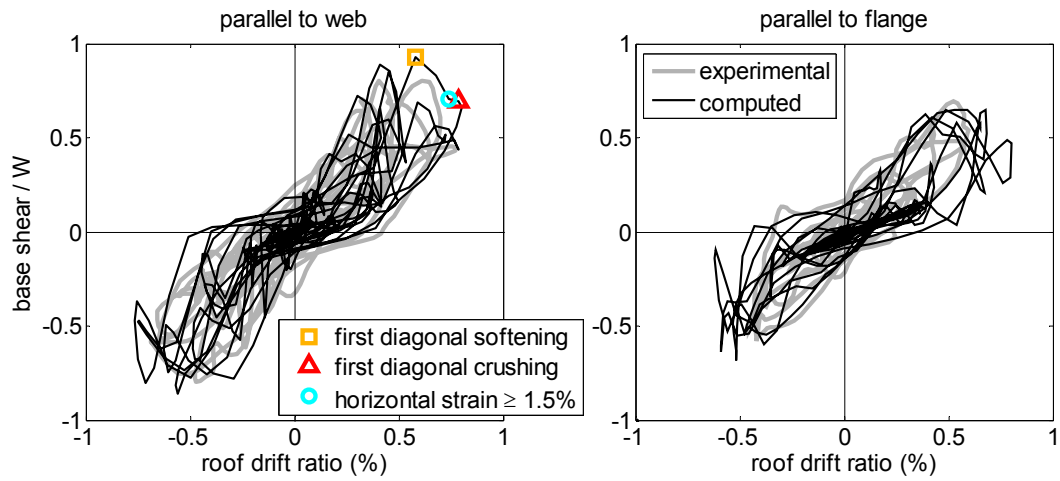


Figure 5.7 Experimentally measured and numerically computed base shear versus roof drift response hysteretic shapes during ground motion T6.

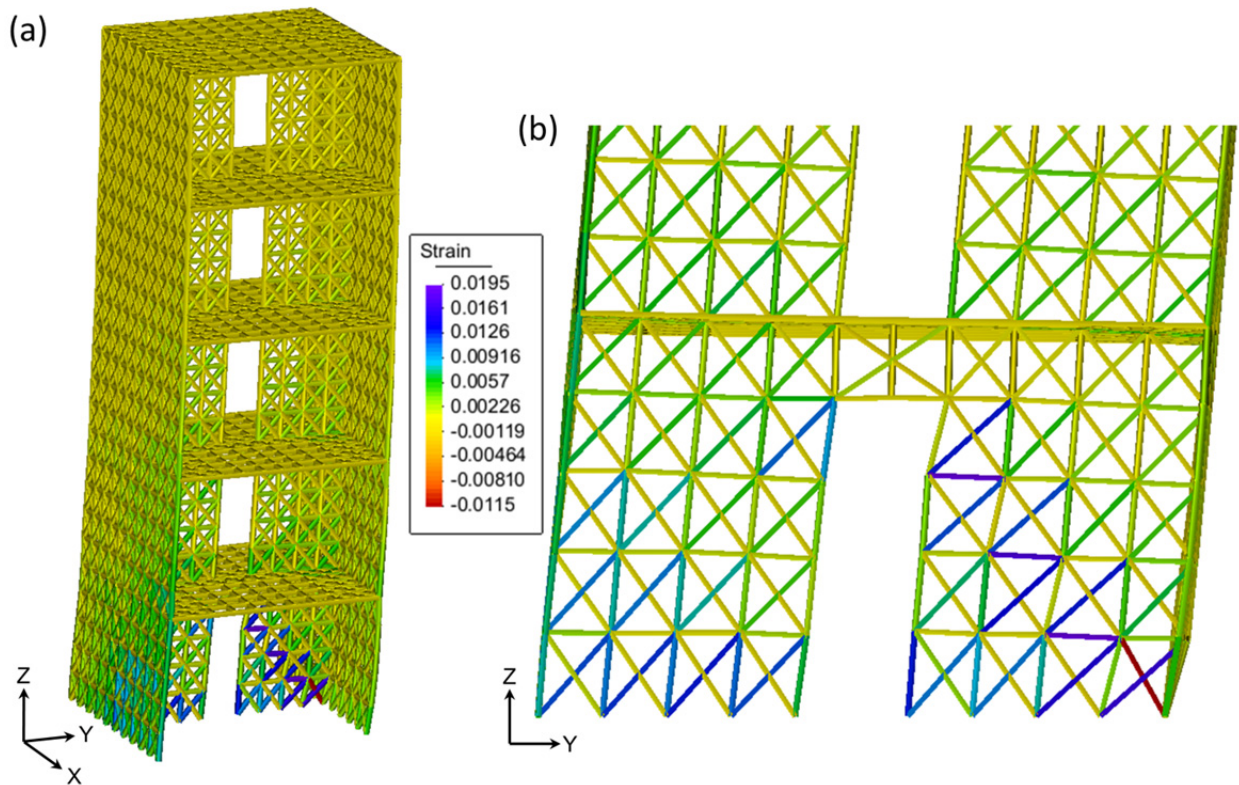


Figure 5.8 Numerically computed strain contour at $t = 3.3$ sec (a) global view and (b) zoom at the web of the bottom story (magnification factor = 10).

5.4 EFFECT OF COUPLING

This section discusses the influence of coupling on the specimen for loading in the direction parallel to the web. To quantify the coupling forces between the walls, the axial and shear forces recorded along the height of the wall at the interface of the coupling beam with Wall A are discussed. The shear and axial forces resisted by the coupling beam and slab is termed coupling shear and axial force, respectively. Figure 5.9(a) shows the coupling shear force at the first story and over the building height, respectively. The slab contributes up to 18% of the peak coupling shear force at first story and 30% of the peak coupling shear force over the entire height. The peak coupling shear force of the first story is on average 36% of the sum of the coupling shears over the entire height by Equation (2.4) for an effective flange width of 0.88 m. Figure 5.9(b) shows that the peak net coupling axial forces at the first story and over the building height are 0.35 and 0.73 times the total building weight W , respectively. The axial force is due to the compression strut running from the bottommost coupling beam to the base of the compression wall [see Figure 5.4(b)], providing a nearly unobstructed compression strut through both walls. The horizontal elements of the bottommost coupling beam were in tensile strain over the entire analysis, while shear deformations in the coupling beam caused compression of the diagonal concrete struts. The effect of large net axial compression force on the coupling beam and slab is not accounted for in Equation (2.4). It is additionally noted that, for the case where the mass block is not modeled with stiff elements, the coupling beam forces and axial load variation is nearly identical to that observed in the default BTM used.

Figure 5.10 shows the base shear force resisted by the two T-section walls separately, where Wall A and Wall B are the T-shaped section walls in the negative and positive y -direction, respectively, as shown in Figure 5.1(a). Wall A resists 88% of the peak shear force in the negative y -direction, and Wall B resists 80% of the peak shear force in the positive y -direction. The shear force-drift ratio hysteresis shown in Figure 5.10(b) has an asymmetric shape in which Walls A and B resists significant shear only for negative and positive drift ratios, respectively. Note that the direction in which each wall resists the most shear is the direction where the flange is in compression and when the axial compression they resist increases due to coupling. The reason for the imbalance of shear force distribution between the walls is due to the axial load variation in the walls, as shown in Figure 5.11; the axial load variation is defined as the difference between the instantaneous axial load and the axial load resisted at the undeformed state ($W/2$ for each wall and W for the entire structure). While the maximum axial load variation for the specimen as a whole is $0.67W$, each wall had an axial load variation up to $1.65W$. Prior to diagonal softening at $t = 3.26$ sec, Wall A experienced a tension force of $1.0W$, while Wall B experienced a compression force of $2.1W$.

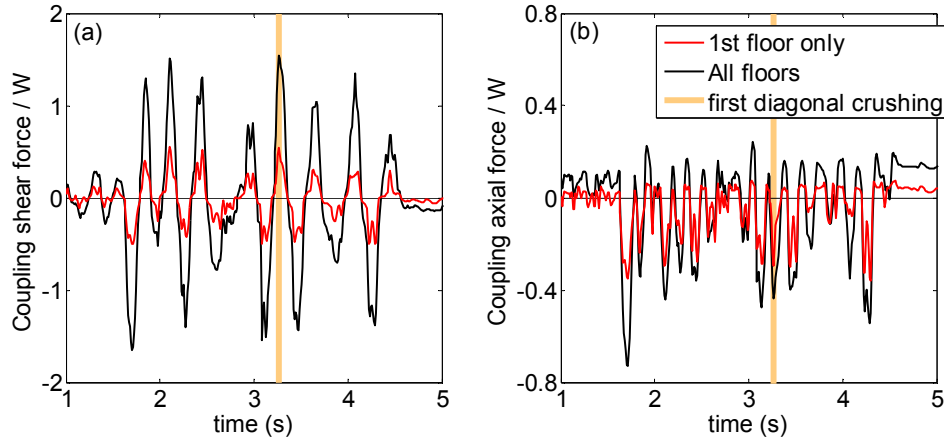


Figure 5.9 Response history of (a) shear force and (b) axial force resisted by the coupling beams and slabs at the interface with Wall A.

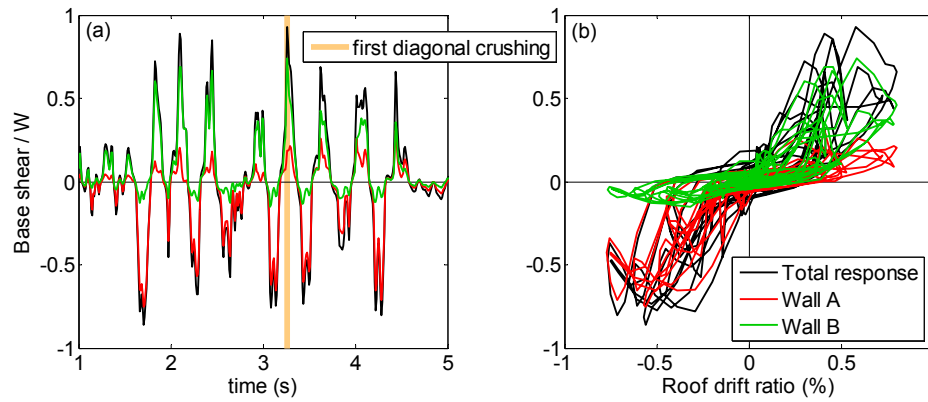


Figure 5.10 (a) Response history of normalized base shear force and (b) normalized base shear force versus roof drift ratio for the two T-section walls, as defined in Figure 5.1(a).

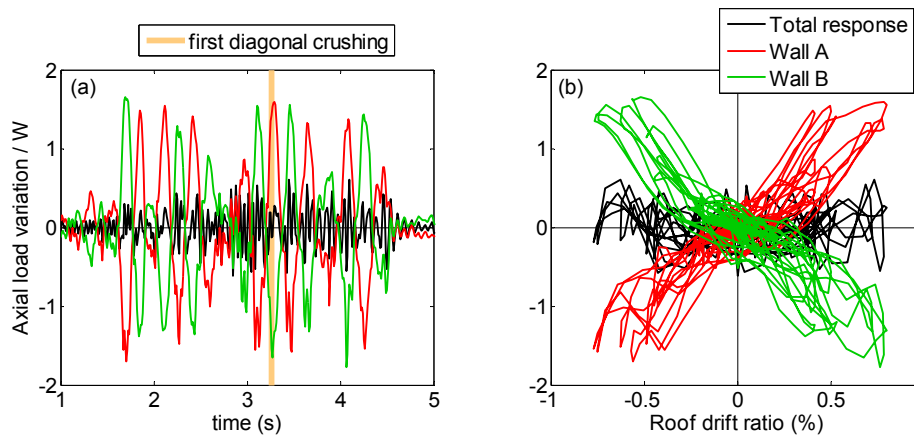


Figure 5.11 (a) Response history of axial load variation and (b) axial load variation versus roof drift ratio for the two T-section walls, as defined in Figure 5.1(a).

5.5 EFFECT OF CONCRETE TENSILE STRENGTH WITH HORIZONTAL ELEMENTS

As discussed in Section 2.5, modeling of the tension resistance of concrete in the horizontal direction and aggregate interlock affect the computed displacement level at onset of diagonal tension failure. A BTM with cracking and aggregate interlock (BTM-HT) as defined in Section 3.3 is used and compared to the response of the default BTM.

Table 5.1 lists the experimentally recorded and numerically computed structural periods for the default BTM and BTM-HT. As expected, the initial stiffness for the BTM-HT is greater than that of the default BTM. After the static load cycles, BTM-HT results in a larger period in the direction parallel to the flange and a smaller period in the direction parallel to the web. Figure 5.12 shows the base shear force and roof drift response histories. BTM-HT overestimated the peak roof displacement by 28% and 4% in the flange and web direction, respectively. However, the peak roof drift of the cycle at $t = 4$ sec is underestimated by 26%, possibly because failure was not computed in the cycle before. The maximum shear force is overestimated by 37% in the direction parallel to the web but shows good agreement parallel to the flange. BTM-HT computes the first softening of concrete diagonals at $t = 3.29$ sec. BTM-HT does not, however, compute diagonal crushing: the maximum compressive strain in the diagonals is 0.23% while the maximum tension strain in the horizontals is 0.5%.

For ground motion T6, the BTM-HT shows less agreement with the experimental results compared to the default BTM because aggregate interlock delays the development of large horizontal strains in BTM-HT, as discussed in Section 2.5. However, BTM-HT results in more accurate results for small displacements: when subjected to ground motion T5 (not shown in this report), the BTM-HT underestimates the peak roof drift parallel to the web by 26% while the regular BTM overestimates the peak roof drift parallel to the web by more than 200%. In the direction parallel to the flange, the two models BTM and BTM-HT exhibited very little difference because the flanges behave in a flexural manner that makes the effect of aggregate interlock less important, which is consistent with Section 3.3. The discrepancy is because the effects of aggregate interlock and concrete in the horizontal direction are important for small levels of lateral deformations before concrete tension softens significantly. At the larger roof drifts induced by ground motion T6, the presence of distributed shear cracking and the formation of a dominant crack result in the reduction of aggregate interlock forces and contribution of concrete in the horizontal direction.

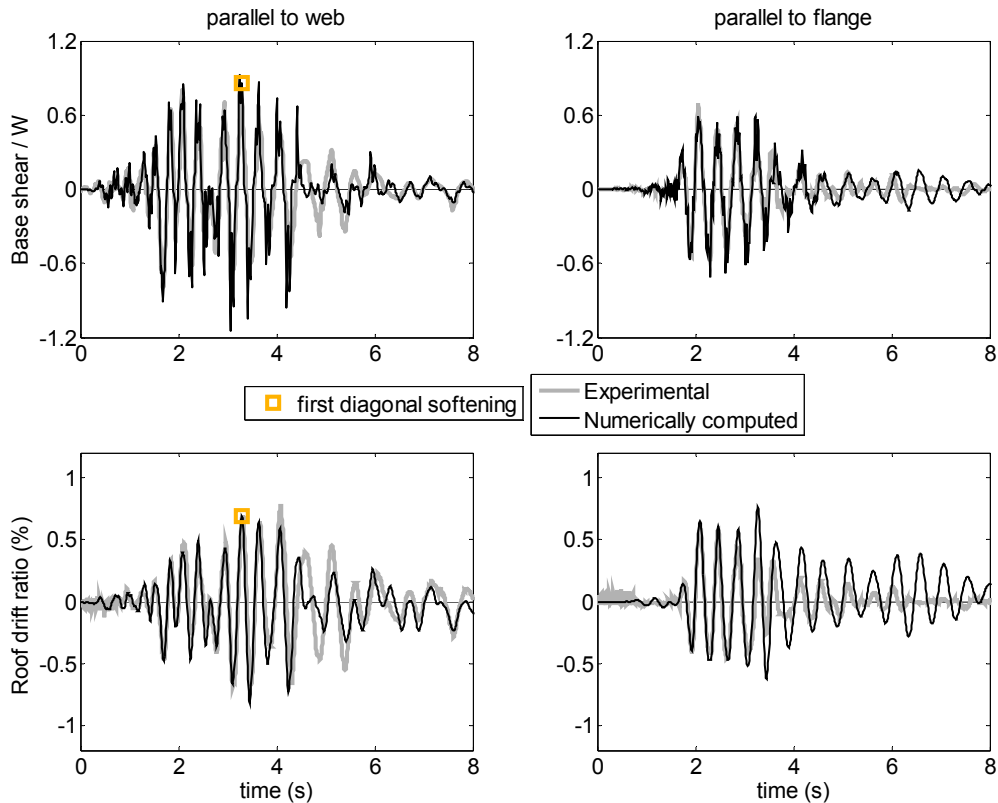


Figure 5.12 Experimentally measured and numerically computed base shear force and roof drift response histories of BTM-HT during ground motion T6.

5.6 EFFECT OF MESH REFINEMENT

In this section, the mesh size of the bottom story of the BTM is refined so that the element size is reduced to half its original value. The resultant model is termed BTM-fineMesh. Figure 5.13 shows the refined mesh for the bottom story: the original mesh layout is shown in black while the additional elements are shown in orange, and additional nodes are added at the element intersections. The BTM-fineMesh has twenty-one vertical lines in each of the flanges and nine vertical lines in each of the two parts of the web with a total of fifty-eight vertical lines at the base. The elements at the intersection between the flange and the web represent a cross-sectional area of $6 \text{ cm} \times 6 \text{ cm}$ and the corresponding steel as described in Detail 1 of Figure 5.1. The vertical lines at the ends of the flanges represent a cross-sectional area of $13 \text{ cm} \times 6 \text{ cm}$ and the corresponding steel as described in Details 2 and 3 of Figure 5.1; other vertical lines in the flanges represent a cross-sectional area of $7.11 \text{ cm} \times 6 \text{ cm}$ and the corresponding steel area. In the web, the two vertical lines immediately adjacent to the coupling beam represents a cross-sectional area of $6 \text{ cm} \times 6 \text{ cm}$ and the corresponding steel as described in Details 4 and 5 of Figure 5.1, while the remaining cross-sectional area is represented equally among the vertical lines representing the web. The mesh of the coupling beam is also refined, with four pairs of crossing diagonal elements; diagonals have a concrete area of $8.4 \text{ cm} \times 6 \text{ cm}$ and diagonal steel reinforcement is represented in the elements along the main (corner-to-corner) diagonals. Material properties for the BTM-fineMesh are the same as that in the BTM except for the changes due to mesh objectivity as described in Sections 2.2 and 2.3.

Figure 5.14 shows the base shear and roof drift ratio time history experimentally recorded and numerically computed using BTM-fineMesh during ground motion T6. The maximum roof drift ratio calculated by the BTM-fineMesh has less than a 1% difference than that calculated with the BTM for both principal horizontal directions. However, BTM-fineMesh computes first diagonal softening at $t = 1.7$ sec, which is much earlier than BTM. However, both BTM and BTM-fineMesh compute first diagonal crushing and the horizontal elements exceeding 1.5% strain in tension at $t = 3.3$ sec, as shown in Figure 5.15 for BTM-fineMesh. The diagonal crushing of concrete occurs in the wall adjacent to the coupling beam, below the bottom corner of the coupling beam where compression is transferred to the wall; this computed failure is consistent with the damage shown in Figure 5.3(b) in the wall near the coupling beam. As in the BTM, BTM-fineMesh computes a nominally elastic response of the coupling beams, which is in good agreement with the observed lack of damage in the coupling beams.

The similar responses and failure modes of the BTM and BTM-fineMesh demonstrates the mesh objectivity of the model a consistent diagonal angle. The BTM-fineMesh is able to compute more localized strains and failures, as shown in Figure 5.15, and will be used in the next section to model fracture of the horizontal steel.

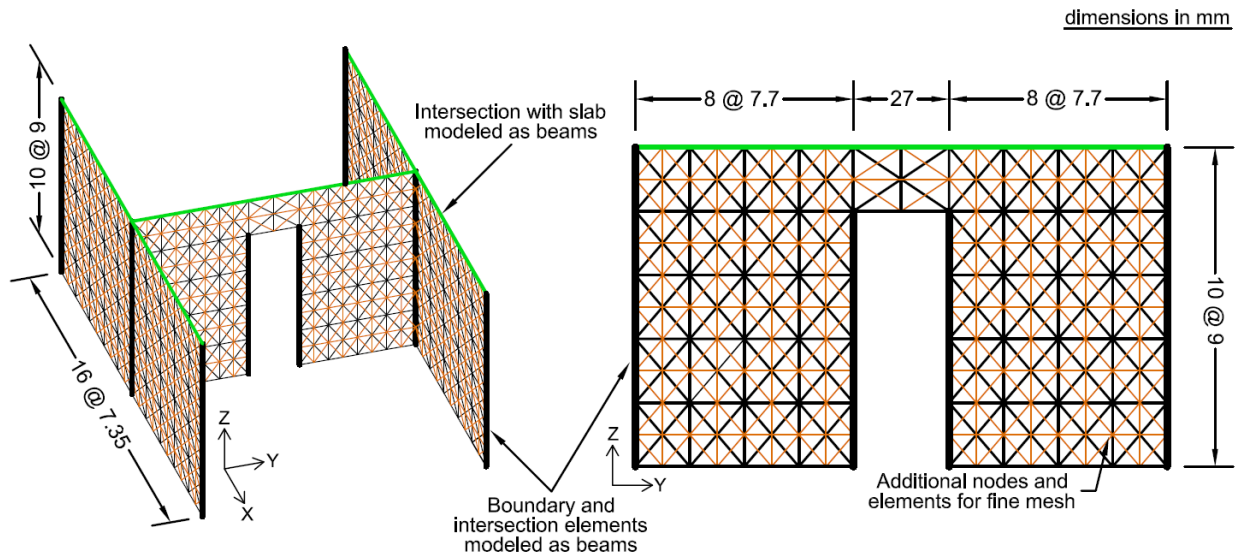


Figure 5.13 BTM with mesh refinement in the bottom story (BTM-fineMesh); the additional elements of BTM-fineMesh are shown in orange over the original BTM mesh (shown in black).

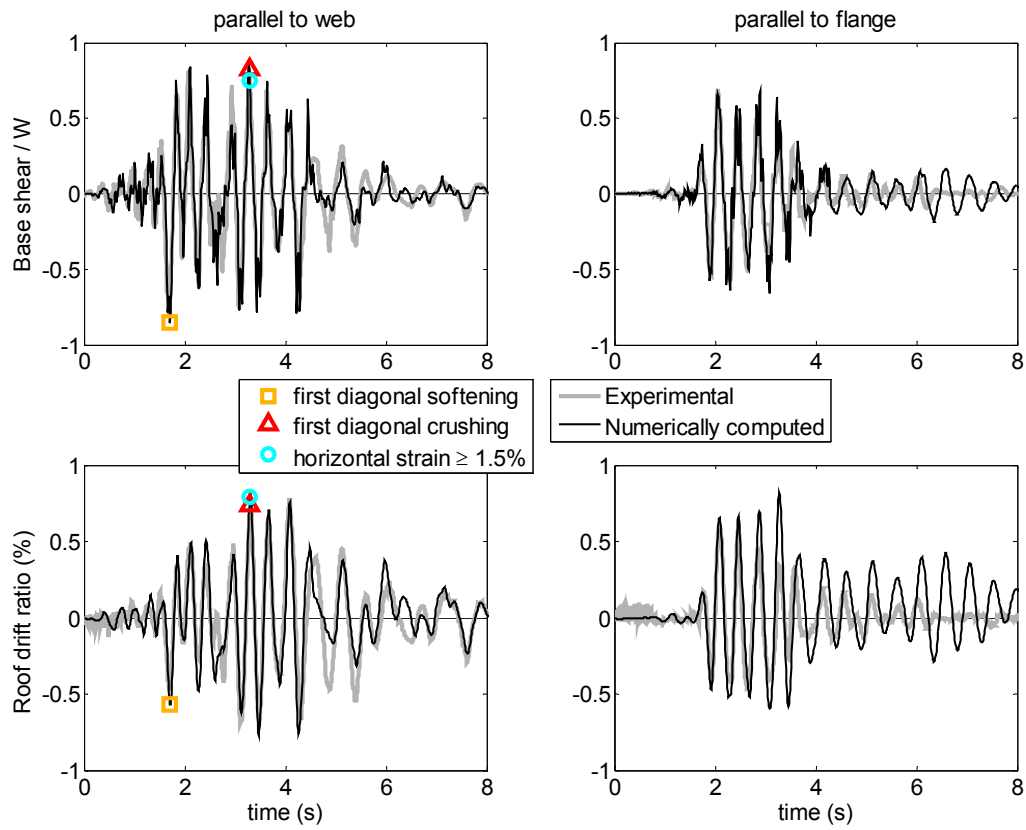


Figure 5.14 Experimentally measured and numerically computed response time histories during ground motion T6 using BTM-fineMesh (BTM with mesh refinement in the bottom story).

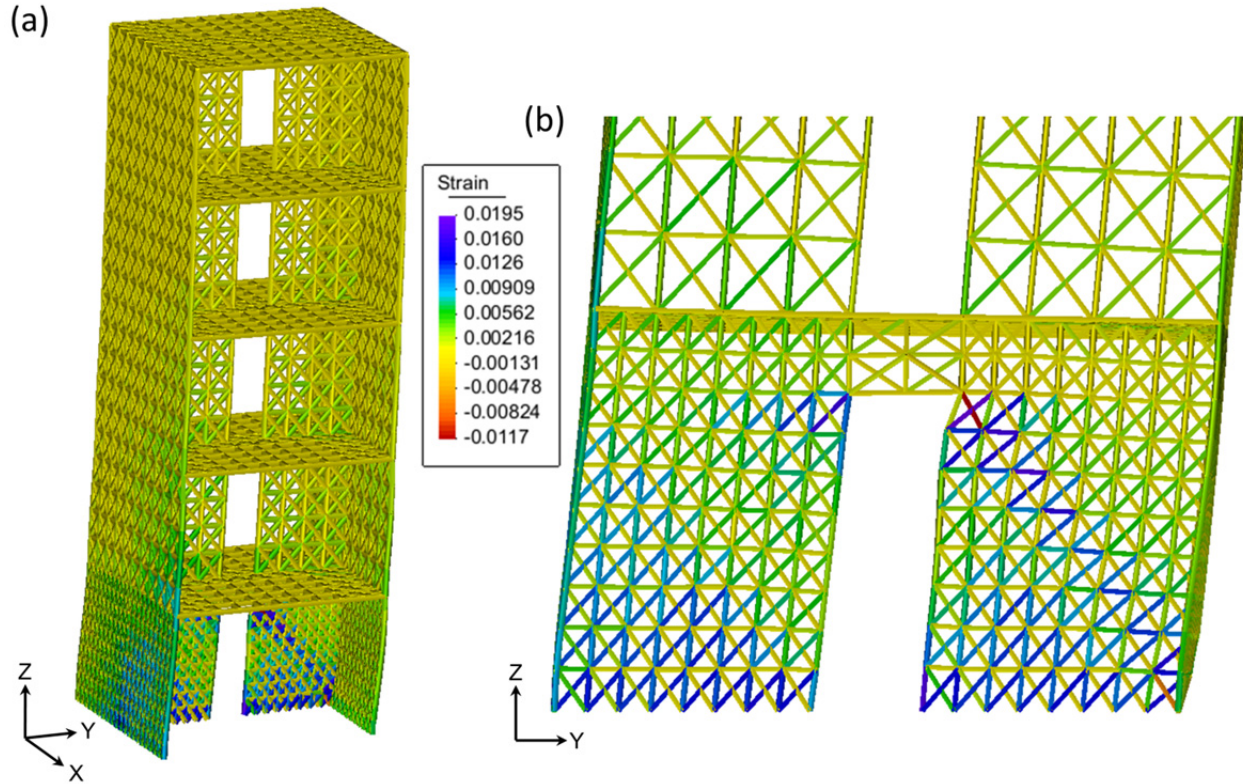


Figure 5.15 Numerically computed strain contour at $t = 3.3$ sec (a) global view and (b) zoom at the web of the bottom story for BTM-fineMesh (BTM with mesh refinement in the bottom story).

5.7 EFFECT OF BAR FRACTURE

In previous sections, the BTM and BTM-fineMesh computed a diagonal tension failure in Wall B of the specimen during ground motion T6. However, despite the large strains calculated (greater than 1.5%, the reported failure strain for the 3-mm-diameter steel used for the horizontal reinforcement), the steel material used in those models do not include the effects of fracture and do not account for the loss of strength in the horizontal elements due to fracture. In this section, the parallel GMP steel material model is altered by the authors to model fracture of the 3-mm-diameter steel reinforcement in the horizontal direction. The model is termed BTM-fineFrac.

The effect of fracture is accounted for in the steel material model as follows: after reaching the ultimate strain ϵ_u in tension, the strength of the steel material degrades with tangent modulus equal (in absolute values) to the initial stiffness (see Figure 5.16) and reaches zero stress at the strain of ϵ_r . The degrading modulus is defined to be the same as the initial stiffness to prevent numerical problems. As indicated in Figure 5.16, exceedance of the ultimate strain ϵ_u results in isotropic softening, i.e., a degradation of both the tensile and compressive strength of the reinforcement.

Figure 5.17 shows the computed base shear force and roof drift ratio response histories computed using BTM-fineFrac and the GMP material model with fracture. Up to $t = 3.3$ sec—the instance of horizontal bar fracture—the computed response is identical to that of BTM-fineMesh. Figure 5.18 shows the strain contour and deformed shapes of BTM-fineFrac at $t = 3.27$ sec and

3.31 sec before and after fracture occurs. At $t = 3.27$ sec, the part of Wall B near the coupling beam shows both the tension strains forming in the horizontals and the near-crushing state of the diagonal element below the coupling beam; see Figure 5.18(b). At $t = 3.31$ sec, the diagonal element below the coupling beam has crushed, and the diagonal tension failure forms, see Figure 5.18(c). Note that the horizontal elements in which the diagonal tension failure forms is not the same elements that had greater than 0.8% tensile strain at $t = 3.27$ sec; this is because the diagonal crushing and subsequent loss of strength in the diagonal element forces the model to use an alternate load path, causing the diagonal tension failure shown in Figure 5.18(c).

By $t = 3.31$ sec, all of the horizontal bars along the main diagonal have fractured, and Wall B has lost more than 55% of lateral load capacity. In comparison to BTM-fineMesh, which did not model the fracture, BTM-fineFrac computes 50% less base shear in Wall B and 68% more base shear in Wall A during the cycles after $t = 3.31$ sec. The peak horizontal strain calculated for BTM-fineFrac is 8.4%, compared to the 1.9% computed by BTM-fineMesh. While both of the models did not compute the diagonal failure in Wall A as shown in the experimental response in Figure 5.3, BTM-fineFrac computes up to 0.9% horizontal strain in Wall A when the roof drift is in the positive y -direction (the direction that causes tension forces in Wall A).

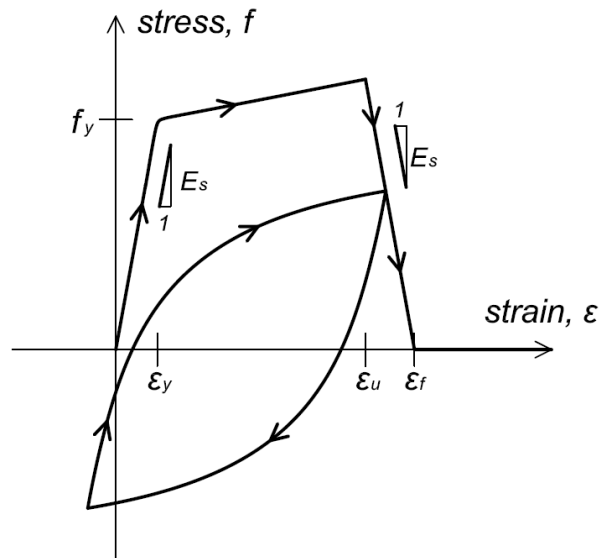


Figure 5.16 Uniaxial stress-strain behavior for the steel material model including the effect of rupture.

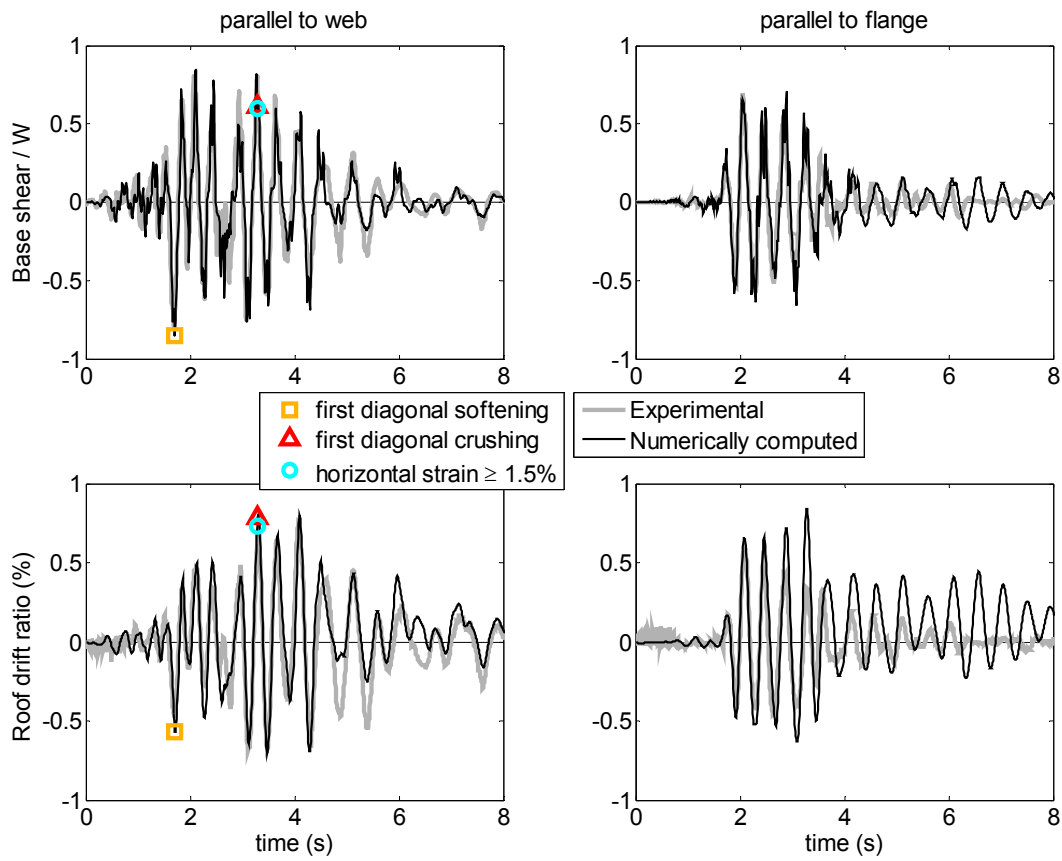


Figure 5.17 Experimentally measured and numerically computed response time histories for ground motion T6 using BTM-fineFrac (BTM with mesh refinement and bar fracture).

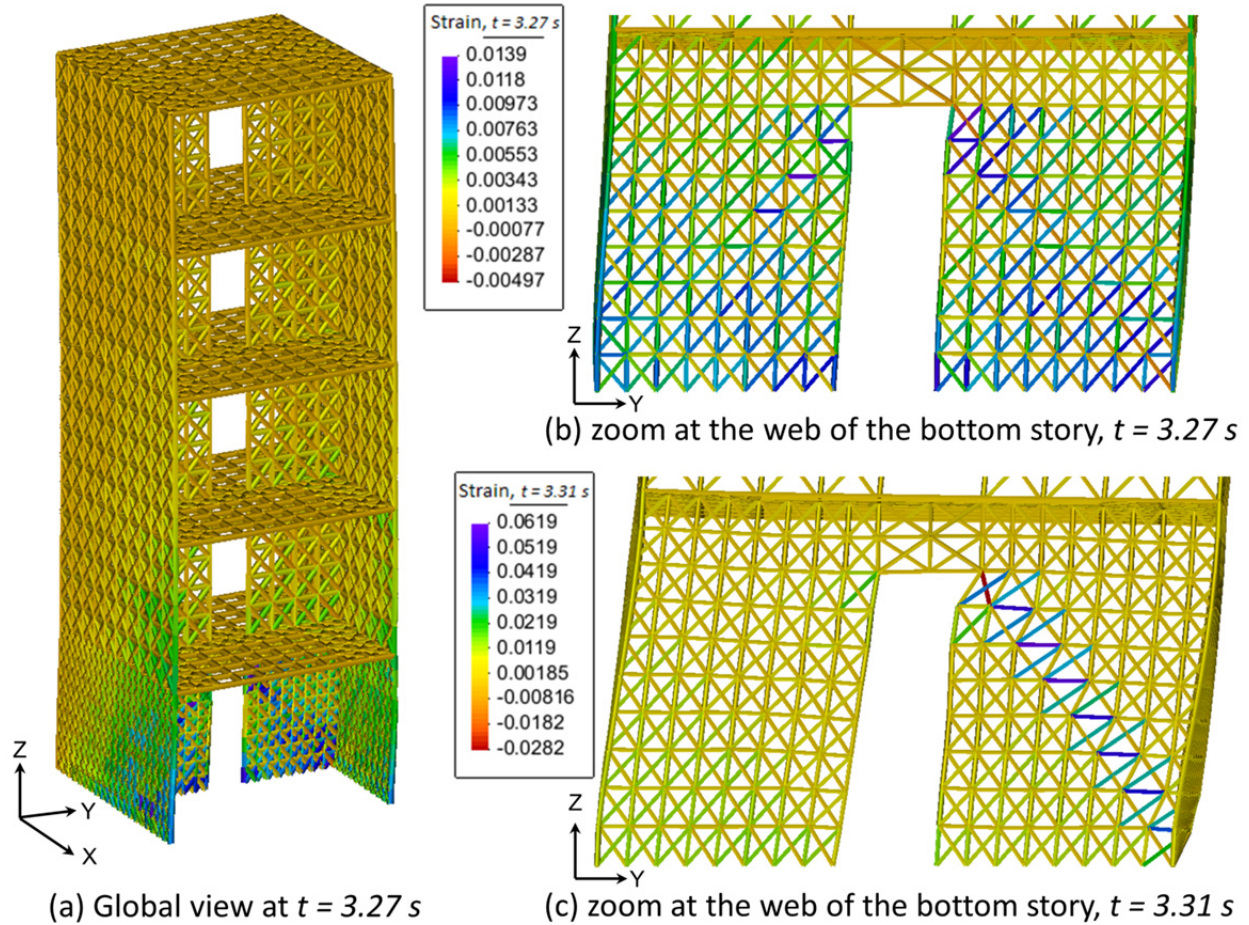


Figure 5.18 (a) Global view and (b) zoom at the web of the bottom story of the computed strain contour immediately before diagonal crushing and bar fracture at $t = 3.29$ sec, and (c) zoom at the web of the bottom story after diagonal crushing and bar fracture at $t = 3.31$ sec (magnification factor = 10).

6 Conclusions

In this report, the beam-truss model (BTM), first developed in Lu and Panagiotou [2014], is improved to better compute the behavior of planar and non-planar reinforced concrete (RC) walls, including the effect of flexure-shear interaction and diagonal shear failures. The main changes include: (1) for vertical lines that are not at the ends of a wall segment, the elements are pinned in the plane of the wall segment, (2) the diagonal angle, which is determined based on the shear demand and geometry of the model, and (3) concrete tension in the horizontal elements is ignored. The BTM methodology is extended to model slabs and coupling beams.

Six static cyclic uniaxially loaded planar and non-planar wall specimens, two static cyclic multiaxially loaded non-planar wall specimens, one static cyclically loaded two bay slab-column specimen, and one 5-story coupled wall and slab system subject to triaxial ground motions were studied and used to validate the proposed beam-truss modelling approach. The main conclusions drawn are:

1. The beam-truss modeling approach gives good results for planar walls with boundary elements. Three of the planar walls studied failed with diagonal crushing of concrete; one of these walls that failed with diagonal crushing was followed by localization of horizontal tension strains over a diagonal band spanning the length of the wall (termed diagonal tension failure). Both types of computed diagonal failures (compression and tension) were in good agreement with the experimental results in terms of failure type and drift ratio of failure. For planar walls with boundary elements longer than 10% of the wall length, boundary elements should be modeled with more than one vertical line.
2. Non-planar walls with I-, U-, and T-shaped sections are considered in this report. The I- and U-section walls failed due to diagonal crushing of concrete, which are in excellent agreement with the experimental results. The T-section walls had flexural-based failures that were not modeled in the BTM. Two non-planar specimens had multiaxial loading and the computed response in the two main directions were in excellent agreement with the experimentally measured response, while the level of agreement in the diagonal and skew directions was decent. In the diagonal and skew directions, the BTM tends to underestimate the strength of the specimen.
3. The dynamically loaded 5-story coupled wall specimen was in good overall agreement with the experimental response, showing that the BTM can be used for dynamic loading. The BTM computed diagonal tension failure in one of the two walls and fracture of the horizontal bars (which were non-ductile) were modeled

in the BTM. The computed failure mode is in good agreement with the experimentally measured response.

The case studies investigated the effect of certain modeling choices of the BTM. The main conclusions regarding these modeling choices are:

1. Elements with in-plane flexural rigidity can be used to effectively model the flexural behavior of the boundary elements of walls. This can reduce the number of vertical lines needed in a BTM. For specimens that experience localization of horizontal strains in a diagonal band (diagonal tension failure), elements with in-plane flexural rigidity should not be used for the vertical lines that are not at the ends of the wall segment because the flexural rigidity influences the computed failure mode.
2. Modeling of tensile strength of the concrete in the horizontal elements only has an important effect for walls that are shear critical (not studied herein), walls with low transverse steel ratio, or walls that exhibit distributed shear cracking. For walls that develop their nominal flexural strength, ignoring the tension strength of concrete in the horizontal direction leads to good agreement with both the failure point and the peak strength of the experimentally tested walls; however, doing so makes the model more flexible in the elastic range compared to the experimental specimen.
3. The diagonal angle of the BTM can significantly affect the computed response. The diagonal angle should be determined based on the shear force demand, the amount of shear reinforcement, and the geometry of the wall. A smaller angle may result in underestimation of lateral strength and a premature or spurious diagonal tension failure, while a larger angle may cause earlier crushing of the concrete in the diagonal direction.

In conclusion, this report improves upon the beam-truss model and serves as a comprehensive validation of the model for planar and non-planar RC walls with different failure modes. The model captures the effects of flexure-shear interaction and shear failures with good accuracy. In addition, an experimentally tested coupled wall-beam-slab system subjected to triaxial ground motions was studied to validate the BTM for coupled walls and for use under dynamic base excitation.

REFERENCES

- American Concrete Institute Committee 318 (ACI 318). (2011). *Building Code Requirements for Structural Concrete (ACI 318-11) and Commentary*, Farmington Hills, MI.
- Beyer K., Dazio A., Priestley M.J.N. (2008). Quasi-static cyclic tests of two U-shaped reinforced concrete walls, *J. Earthq. Eng.*, 12(7): 1023–1053.
- Brueggen B.L. (2009). *Performance of T-Shaped Reinforced Concrete Structural Walls under Multi-Directional Loading*, Ph.D. dissertation, University of Minnesota, Minneapolis, MN, 498 pgs.
- Coelho E., Fischinger M., Campos Costa A., Falcao Silva M. J., Kante, P. (2006). Shaking table tests on thick lightly reinforced H-shaped structural wall, *Proceedings, First European Conference on Earthquake Engineering and Seismology*, Geneva, Switzerland.
- ConcreteBeta Material. OpenseesWiki. http://opensees.berkeley.edu/wiki/index.php/ConcreteBeta_Material, Accessed Oct. 30, 2014.
- Dazio A., Beyer K., Bachmann, H. (2009a). Quasi-static cyclic tests and plastic hinge analysis of RC structural walls, *Eng. Struct.*, 31(7): 1556–1571.
- Dazio A., Beyer K., Braune F., Fritsche S., Mittaz X. (2009b). Das Mw=6.3 Erdbeben von L'Aquila am 6. April 2009, *Report of SGEB-Erkundungsmission vom*, April 15–18. 150 pgs.
- Hines E.M., Seible, F. (2004). Web crushing capacity of hollow rectangular bridge piers, *ACI Struct. J.*, 101(4): 569–579.
- Hughes T.J. (2012). *The Finite Element Method: Linear Static and Dynamic Finite Element Analysis*, Courier Dover Publications, New York.
- Ile N., Reynouard J.M., Georgin J.F. (2002). Non-linear response and modeling of RC walls subjected to seismic loading, *ASET J. Earthq. Tech.*, 39(1–2): 1–19.
- Jiang H., Kurama Y.C. (2010). Analytical modeling of medium-rise reinforced concrete shear walls, *ACI Struct. J.*, 107(4): 400–410.
- Kante P. (2005). *Potresna Ranljivost Armiranobetonskih Sten*, Ph.D. dissertation, University of Ljubljana, Ljubljana, Slovenia, 376 pgs.
- Kolozvari K.I. (2013). *Analytical Modeling of Cyclic Shear – Flexure Interaction in Reinforced Concrete Structural Walls*, Ph.D. dissertation, University of California, Los Angeles, CA.
- Kotronis P., Mazars J., Nguyen X. H., Ile N., Reynouard J. M., Bisch P., Coin, A. (2009). The seismic behavior of reinforced concrete structural walls: experiments and modeling, in: *The 1755 Lisbon Earthquake: Revisited* (pp. 363–376). Springer, Netherlands.
- Lu Y., Panagiotou M. (2014). Three-dimensional nonlinear cyclic beam-truss model for reinforced concrete non-planar walls, ASCE, *J. Struct. Eng.*, doi: 10.1061/(ASCE)ST.1943-541X.0000852.
- Maffei J., Yuen N. (2007). Seismic performance and design requirements for high-rise buildings, *Structure Magazine*, 28–32.
- Mander J., Priestley M., Park R. (1988). Theoretical stress-strain model for confined concrete, ASCE, *J. Struct. Eng.*, 114(8): 1804–1826.
- McKenna F., Fenves G.L., Scott M.H. (2000). Open System for Earthquake Engineering Simulation (OpenSees) version 2.4.3 [Software]. Available from <http://opensees.berkeley.edu/>.
- Mestyaneck J.M. (1986). *The Earthquake Resistance of Reinforced Concrete Structural Walls of Limited Ductility*, Master of Engineering thesis, University of Canterbury, Christchurch, New Zealand. 213 pgs.
- Moharrami M., Koutromanos I., Panagiotou M., Girgin S.C. (2014). Analysis of shear-dominated RC columns using the nonlinear truss analogy, *Earthq. Eng. Struct. Dyn.*, doi: 10.1002/eqe.2480.

- Oesterle R.G., Aristizabal-Ochoa J.D., Fiorato A.E., Russell H.G., Corley W. G. (1979). *Earthquake Resistant Structural Walls—Test of Isolated Walls—Phase II*, Report to the National Science Foundation, Construction Technology Laboratories, Portland Cement Association, Skokie, IL.
- Oesterle R.G., Fiorato A.E., Johal L.S., Carpenter L.S., Russell H.G., Corley W.G. (1976). *Earthquake-Resistant Structural Walls—Tests of Isolated Walls*, Report to the National Science Foundation, Construction Technology Laboratories, Portland Cement Association, Skokie, IL.
- Palermo D., Vecchio F.J. (2002). Behavior of three-dimensional reinforced concrete shear walls, *ACI Struct. J.*, 99(1): 81–89.
- Palermo D., Vecchio F.J. (2007). Simulation of cyclically loaded concrete structures based on the finite-element method, *J. Struct. Eng.*, 133(5): 728–738.
- Panagiotou M., Restrepo J.I., Schoettler M., Kim G. (2012). Nonlinear cyclic truss model for reinforced concrete walls, *ACI Struct. J.*, 109(2): 205–214.
- Park, R. Paulay, T. (1975). *Reinforced Concrete Structures*, John Wiley & Sons, Inc., New York.
- Paulay T., Priestley, M.J.N. (1992). *Seismic Design of Reinforced Concrete and Masonry Buildings*, John Wiley & Sons, Inc., New York.
- Robertson I.N. (1990). *Seismic Response of Connections Ii Indeterminate Flat-Slab Subassemblies*, Ph.D. dissertation, Rice University, Houston, Texas. 284 pgs.
- Sittipunt C., Wood, S.L. (1993). Finite element analysis of reinforced concrete shear walls, *Civil Engineering Studies, Structural Research Series No. 584*, University of Illinois, Urbana, Champaign, Urbana, IL.
- Thomsen J.H., Wallace J.W. (1995). Displacement-based design for reinforced concrete structural walls: an experimental investigation of walls for rectangular and T-shaped cross-sections, *Rep. No. CU/CEE-95-06*, Clarkson University., Potsdam, NY.
- Vecchio F.J., Collins M.P. (1986). The modified compression-field theory for reinforced concrete elements subjected to shear, *ACI J. Proc.*, 83(2): 219–231.

Appendix A Computed Strain Contours and Deflected Shapes for Case Studies with Static Loading

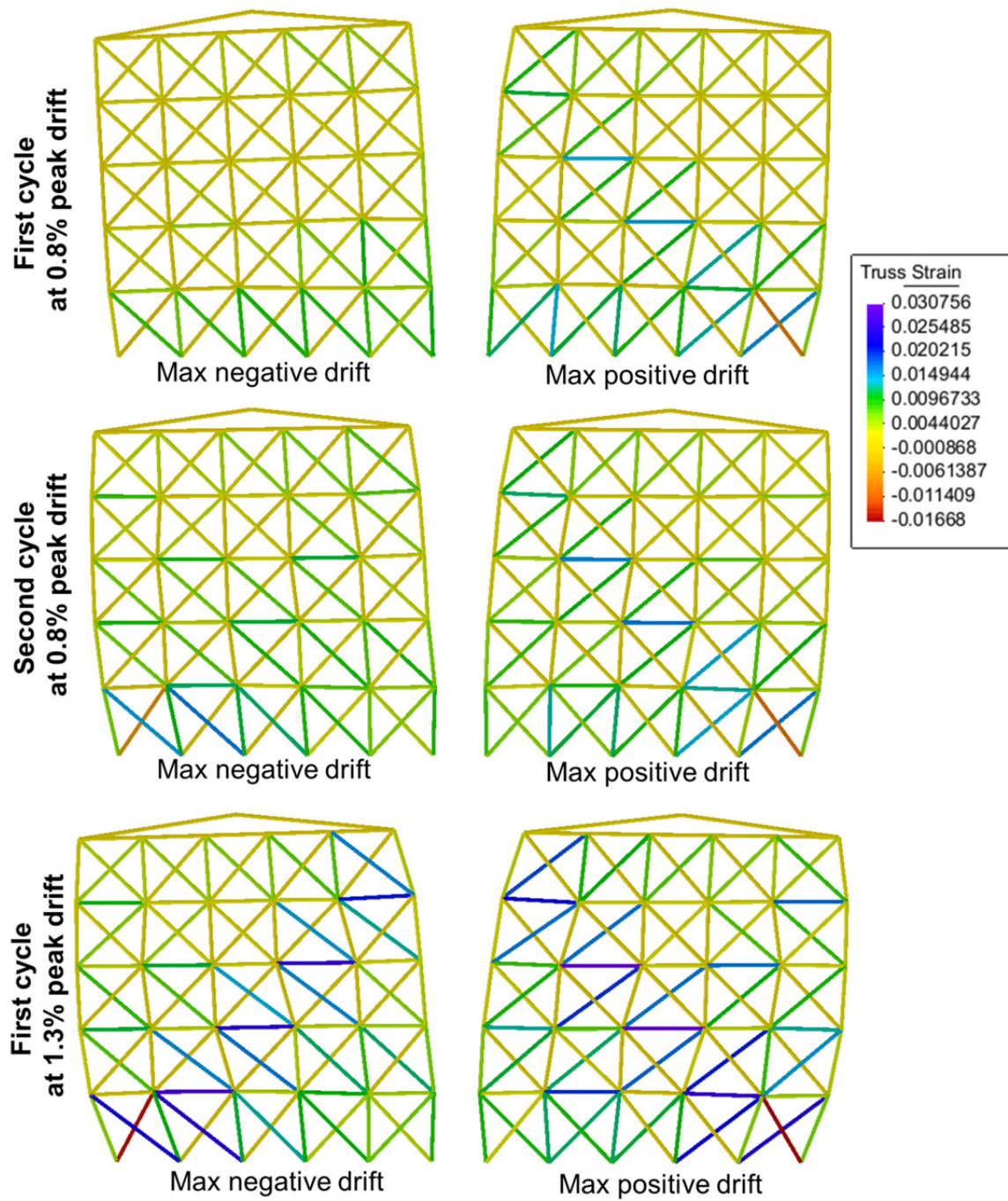


Figure A1.1 Strain contour and displaced shape (magnification factor = 10) for specimen Unit 1.0 at selected drift ratios. Triangular elements at the top of the wall model the loading beam.

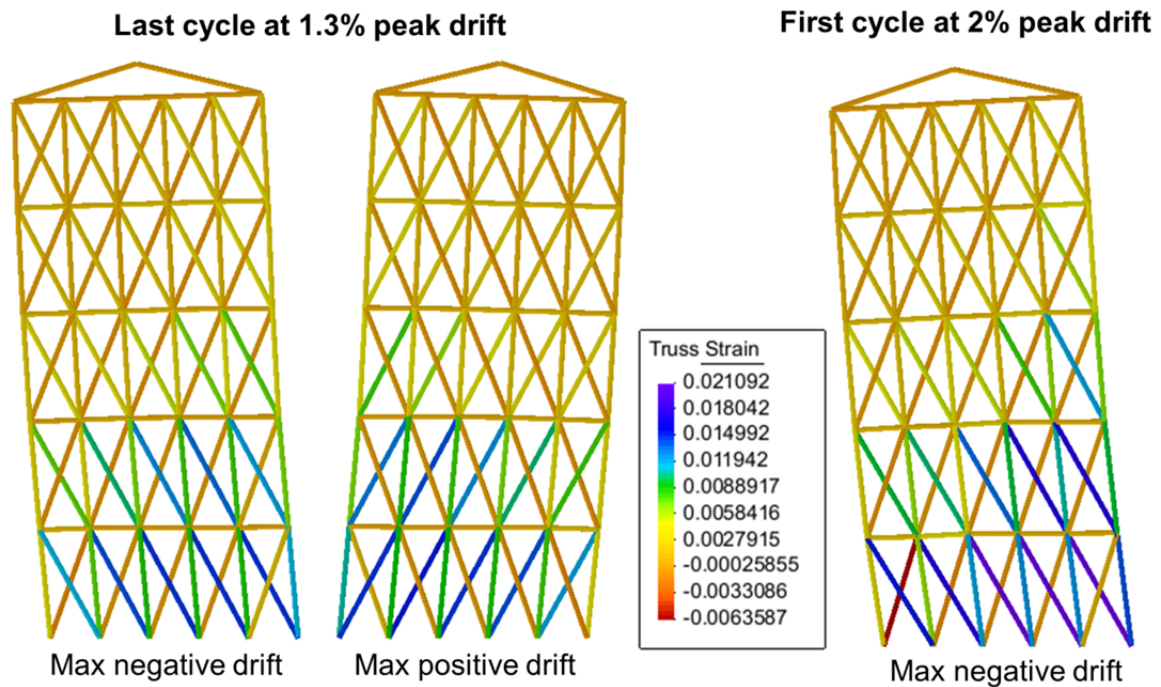


Figure A1.2 Strain contour and displaced shape (magnification factor = 5) for specimen Unit 2.0 at selected drift ratios. Triangular elements at the top of the wall model the loading beam.

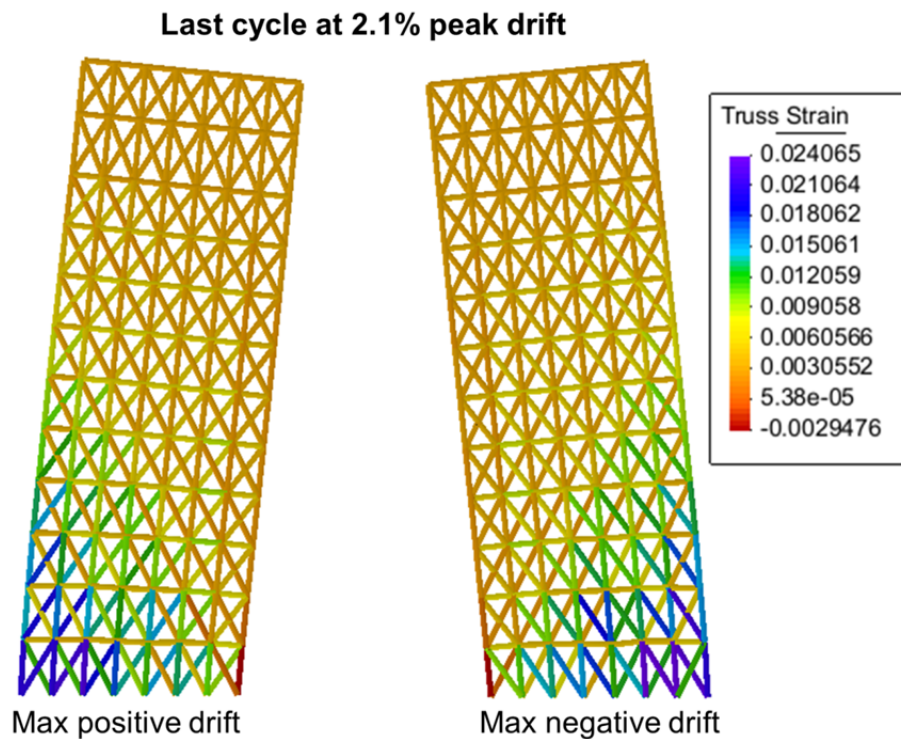


Figure A1.3 Strain contour and displaced shape (magnification factor = 5) for specimen WSH6 at selected drift ratios.

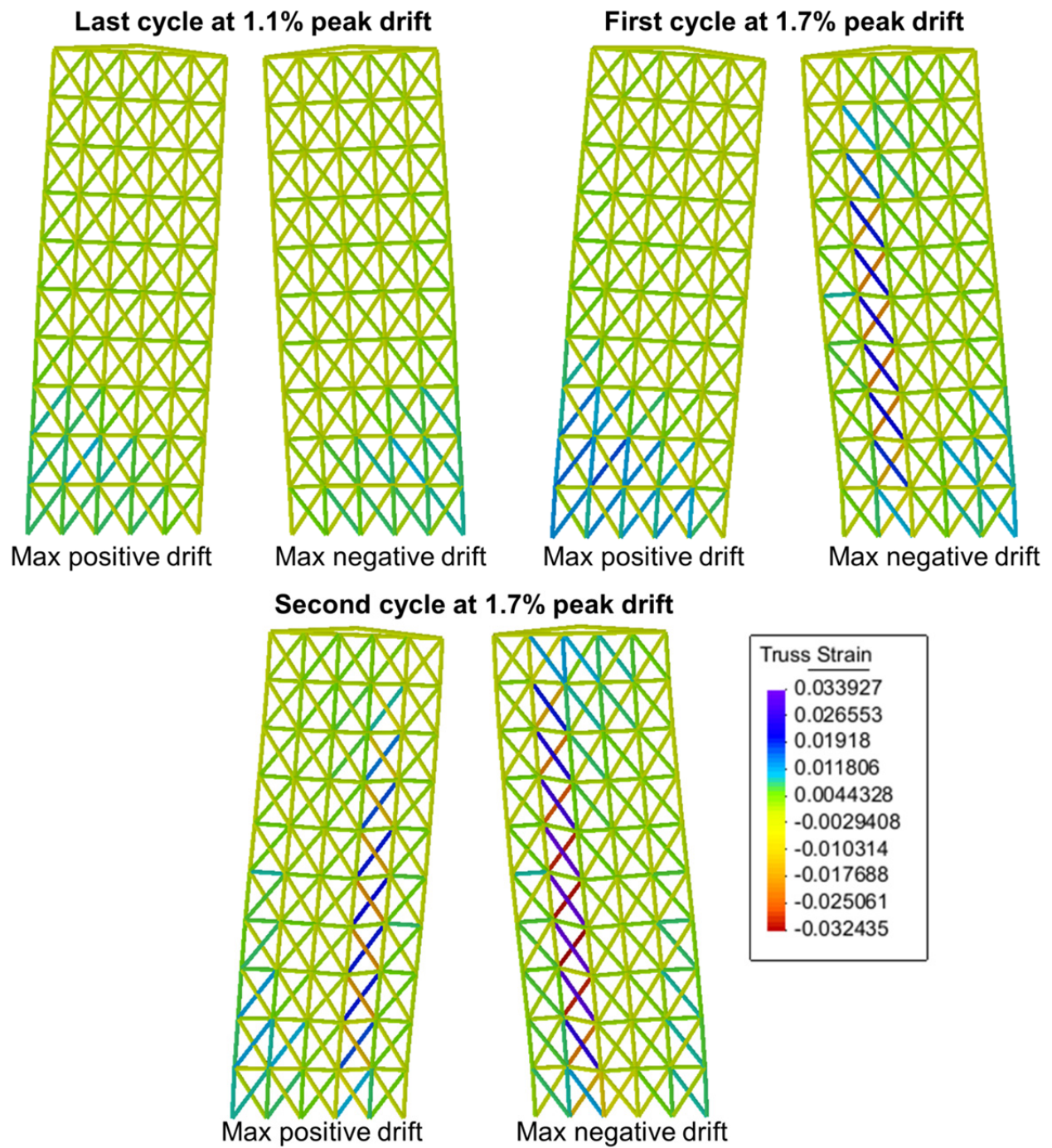


Figure A1.4 Strain contour and displaced shape (magnification factor = 5) for specimen B6 at selected drift ratios. Triangular elements at the top of the wall model the loading beam.

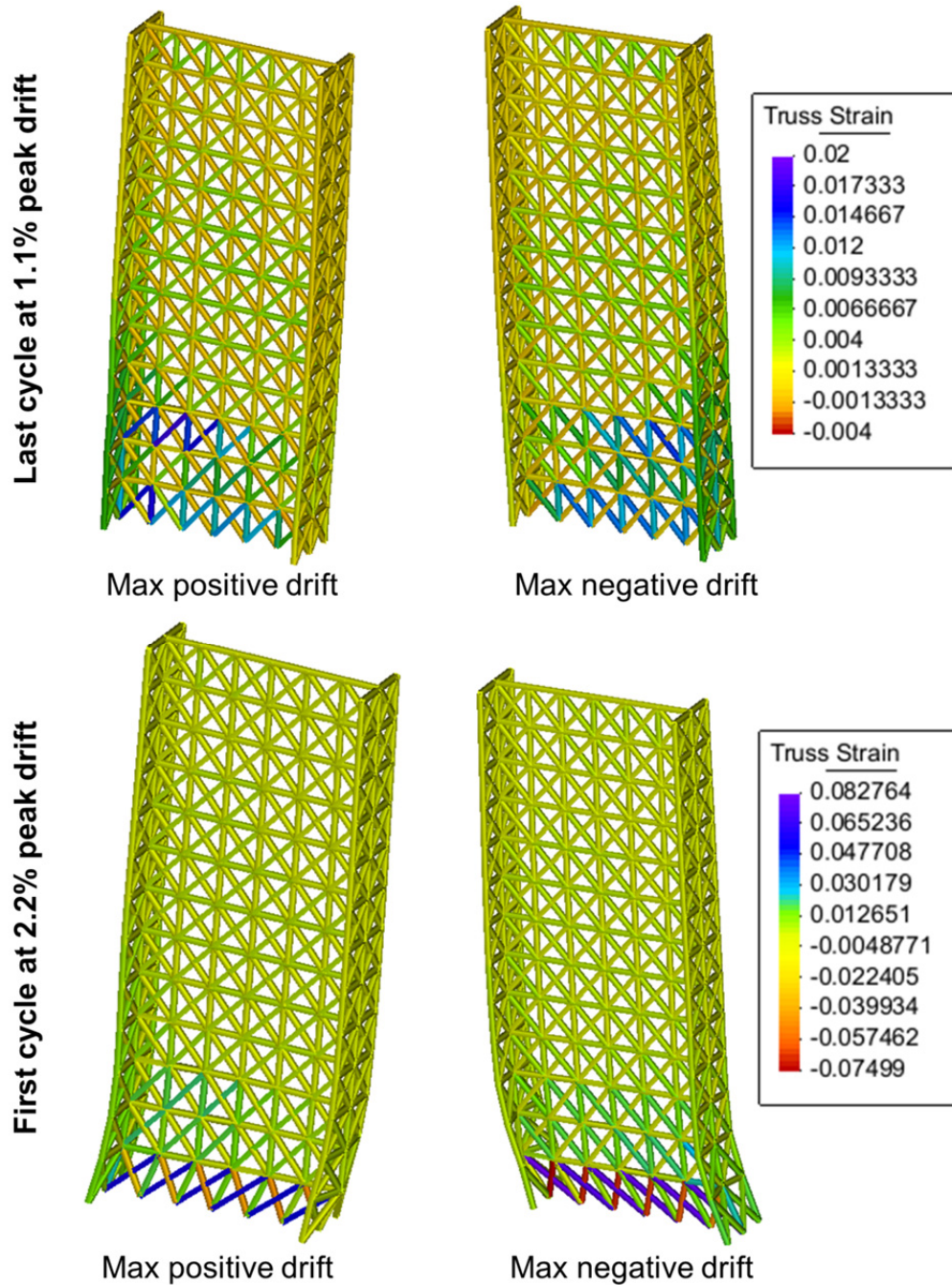


Figure A1.5 Strain contour and displaced shape (magnification factor = 5) for specimen F1 at selected drift ratios.

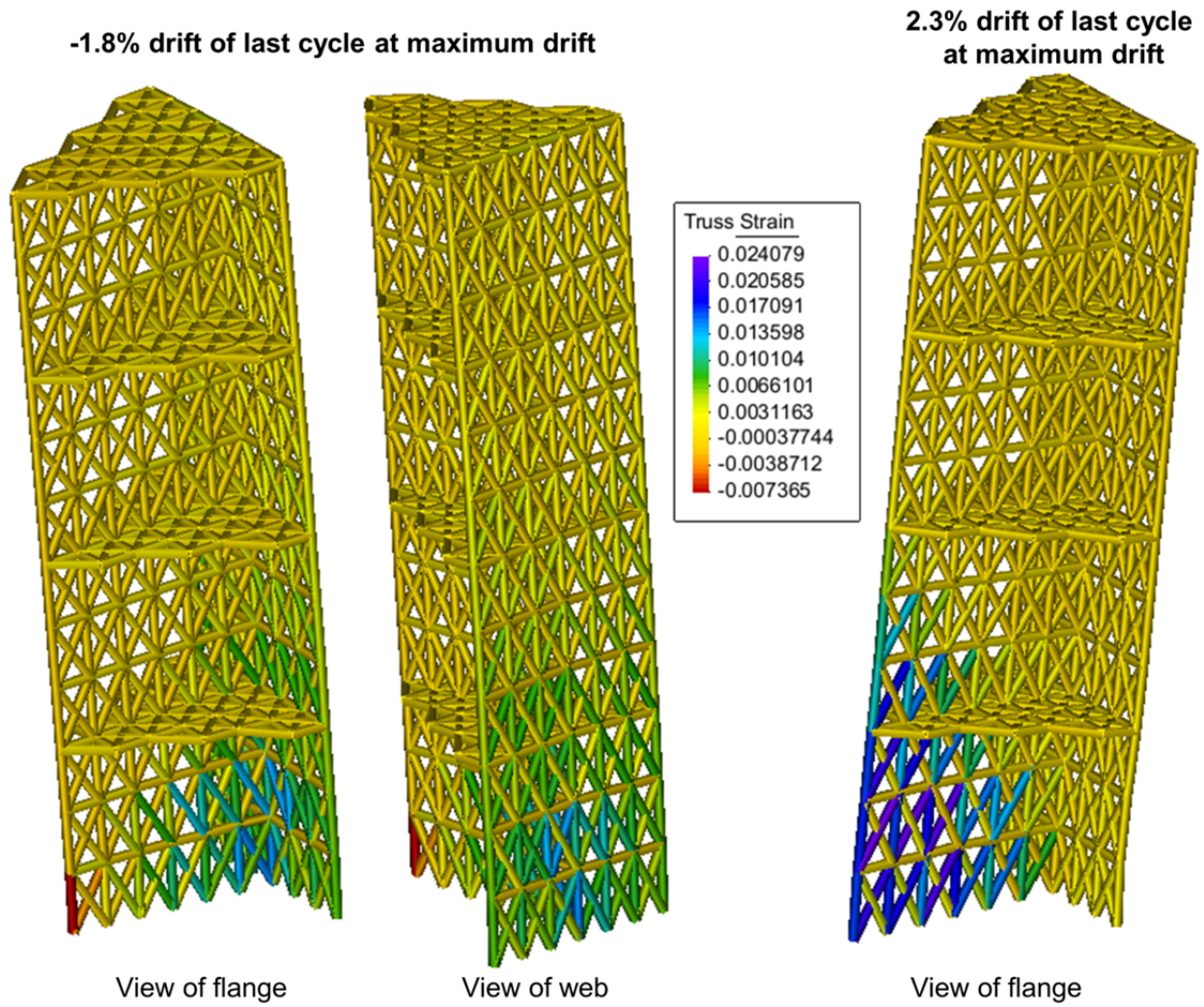


Figure A1.6 Strain contour and displaced shape (magnification factor = 5) for specimen TW2 at selected drift ratios.

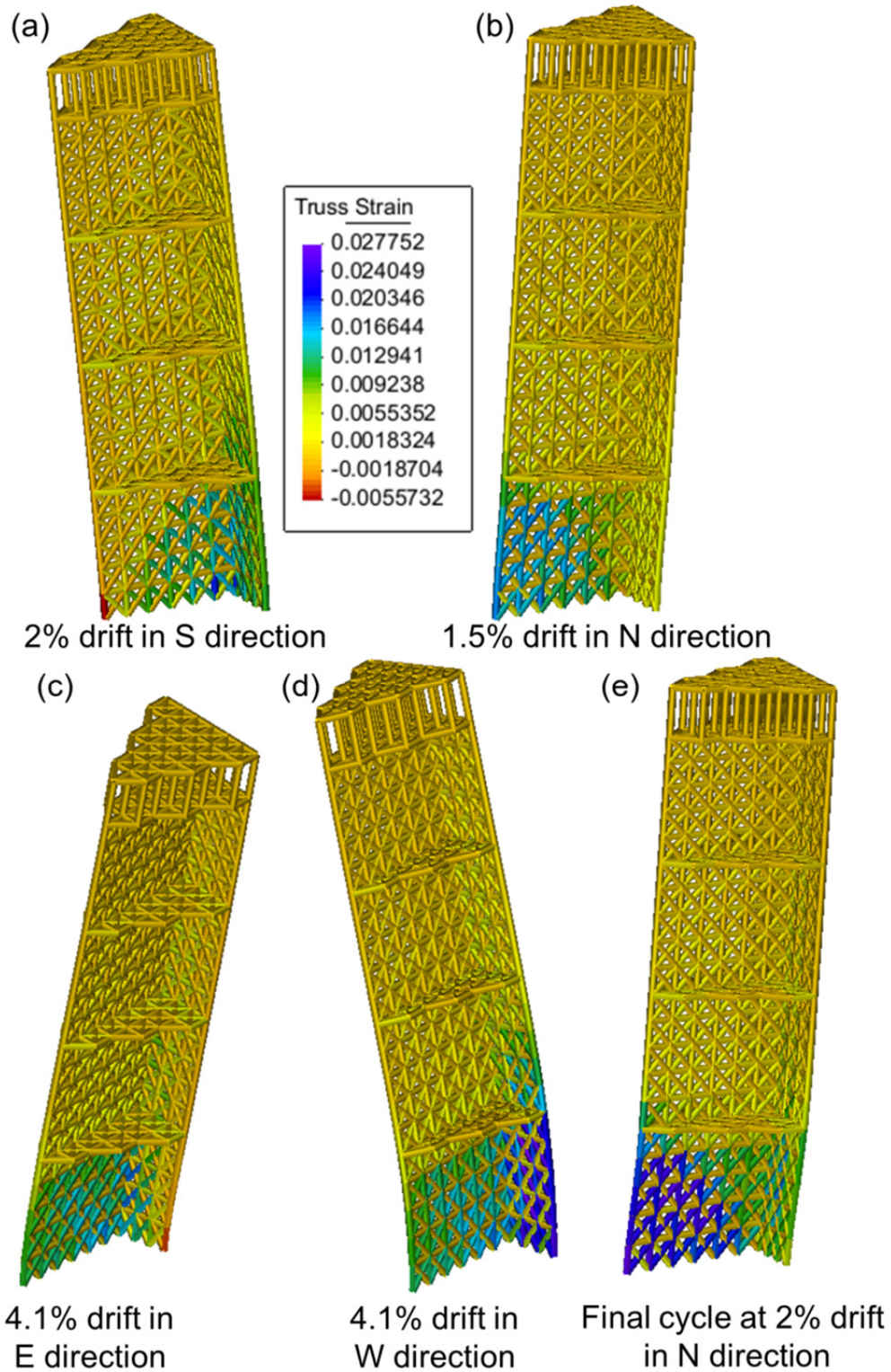


Figure A1.7 Strain contour and displaced shape (magnification factor = 5) for specimen NTW1 at selected drift ratios. Note: strain contours (a) through (e) are shown in the order which the specimen reaches each drift.

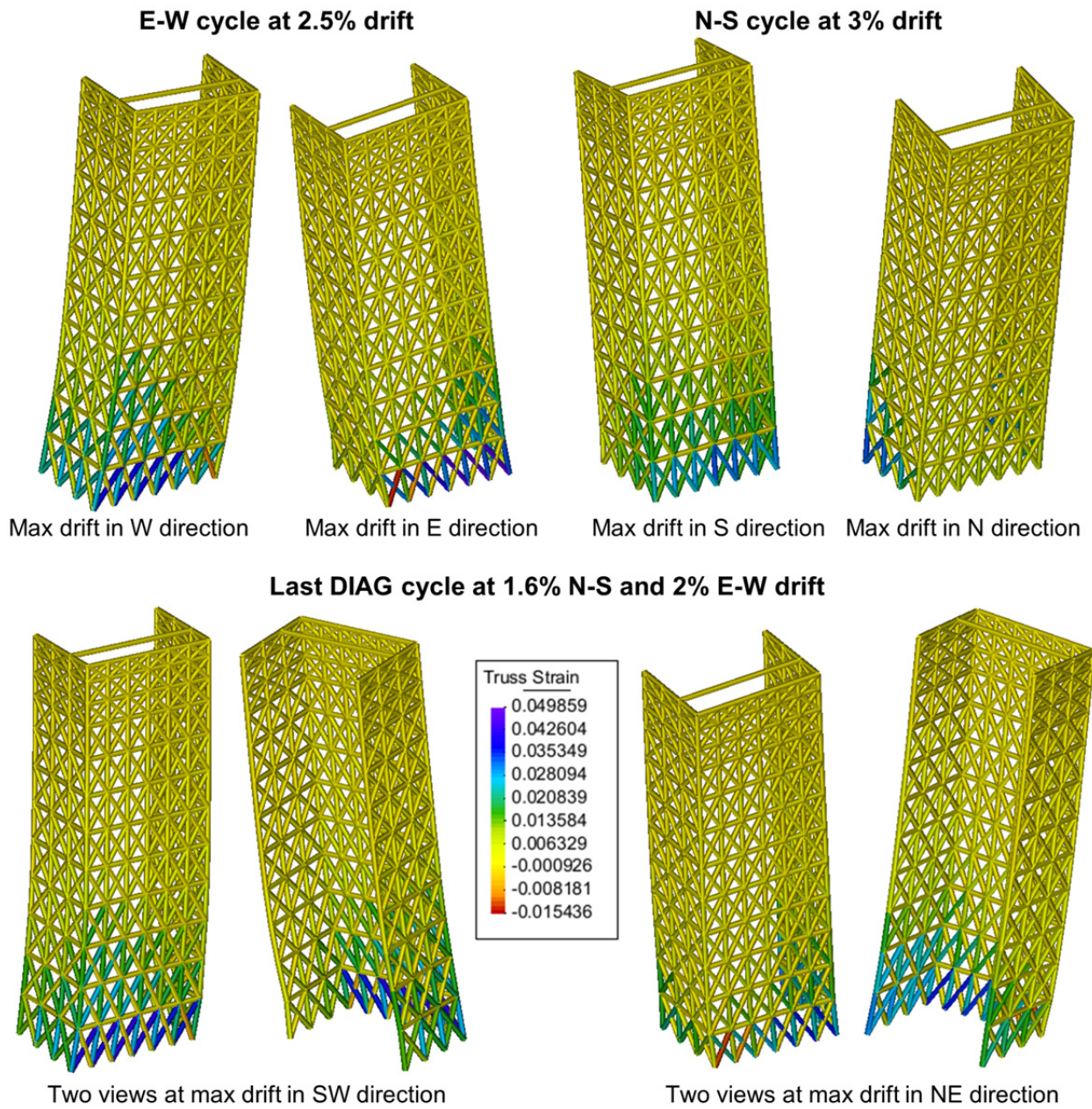


Figure A1.8 Strain contour and displaced shape (magnification factor = 5) for specimen TUB at selected drift ratios.

PEER REPORTS

PEER reports are available as a free PDF download from http://peer.berkeley.edu/publications/peer_reports_complete.html. Printed hard copies of PEER reports can be ordered directly from our printer by following the instructions at http://peer.berkeley.edu/publications/peer_reports.html. For other related questions about the PEER Report Series, contact the Pacific Earthquake Engineering Research Center, 325 Davis Hall mail code 1792, Berkeley, CA 94720. Tel.: (510) 642-3437; Fax: (510) 665-1655; Email: peer_editor@berkeley.edu

- PEER 2014/18** *Three-Dimensional Beam-Truss Model for Reinforced Concrete Walls and Slabs Subjected to Cyclic Static or Dynamic Loading.* Yuan Lu, Marios Panagiotou, and Ioannis Koutromanos. December 2014.
- PEER 2014/17** *PEER NGA-East Database.* Christine A. Goulet, Tadahiro Kishida, Timothy D. Ancheta, Chris H. Cramer, Robert B. Darragh, Walter J. Silva, Youssef M.A. Hashash, Joseph Harmon, Jonathan P. Stewart, Katie E. Wooddell, and Robert R. Youngs. October 2014.
- PEER 2014/16** *Guidelines for Performing Hazard-Consistent One-Dimensional Ground Response Analysis for Ground Motion Prediction.* Jonathan P. Stewart, Kioumars Afshari, and Youssef M.A. Hashash. October 2014.
- PEER 2014/15** *NGA-East Regionalization Report: Comparison of Four Crustal Regions within Central and Eastern North America using Waveform Modeling and 5%-Damped Pseudo-Spectral Acceleration Response.* Jennifer Dreiling, Marius P. Isken, Walter D. Mooney, Martin C. Chapman, and Richard W. Godbee. October 2014.
- PEER 2014/14** *Scaling Relations between Seismic Moment and Rupture Area of Earthquakes in Stable Continental Regions.* Paul Somerville. August 2014.
- PEER 2014/13** *PEER Preliminary Notes and Observations on the August 24, 2014, South Napa Earthquake.* Grace S. Kang (Editor), Stephen A. Mahin (Editors). September 2014.
- PEER 2014/12** *Reference-Rock Site Conditions for Central and Eastern North America: Part II – Attenuation (Kappa) Definition.* Kenneth W. Campbell, Youssef M.A. Hashash, Byungmin Kim, Albert R. Kottke, Ellen M. Rathje, Walter J. Silva, and Jonathan P. Stewart. August 2014.
- PEER 2014/11** *Reference-Rock Site Conditions for Central and Eastern North America: Part I - Velocity Definition.* Youssef M.A. Hashash, Albert R. Kottke, Jonathan P. Stewart, Kenneth W. Campbell, Byungmin Kim, Ellen M. Rathje, Walter J. Silva, Sissy Nikolaou, and Cheryl Moss. August 2014.
- PEER 2014/10** *Evaluation of Collapse and Non-Collapse of Parallel Bridges Affected by Liquefaction and Lateral Spreading.* Benjamin Turner, Scott J. Brandenburg, and Jonathan P. Stewart. August 2014.
- PEER 2014/09** *PEER Arizona Strong-Motion Database and GMPEs Evaluation.* Tadahiro Kishida, Robert E. Kayen, Olga-Joan Ktenidou, Walter J. Silva, Robert B. Darragh, and Jennie Watson-Lamprey. June 2014.
- PEER 2014/08** *Unbonded Pretensioned Bridge Columns with Rocking Detail.* Jeffrey A. Schaefer, Bryan Kennedy, Marc O. Eberhard, John F. Stanton. June 2014.
- PEER 2014/07** *Northridge 20 Symposium Summary Report: Impacts, Outcomes, and Next Steps.* May 2014.
- PEER 2014/06** *Report of the Tenth Planning Meeting of NEES/E-Defense Collaborative Research on Earthquake Engineering.* December 2013.
- PEER 2014/05** *Seismic Velocity Site Characterization of Thirty-One Chilean Seismometer Stations by Spectral Analysis of Surface Wave Dispersion.* Robert Kayen, Brad D. Carkin, Skye Corbet, Camilo Pinilla, Allan Ng, Edward Gorbis, and Christine Truong. April 2014.
- PEER 2014/04** *Effect of Vertical Acceleration on Shear Strength of Reinforced Concrete Columns.* Hyerin Lee and Khalid M. Mosalam. April 2014.
- PEER 2014/03** *Retest of Thirty-Year-Old Neoprene Isolation Bearings.* James M. Kelly and Niel C. Van Engelen. March 2014.
- PEER 2014/02** *Theoretical Development of Hybrid Simulation Applied to Plate Structures.* Ahmed A. Bakhty, Khalid M. Mosalam, and Sanjay Govindjee. January 2014.
- PEER 2014/01** *Performance-Based Seismic Assessment of Skewed Bridges.* Peyman Kaviani, Farzin Zareian, and Ertugrul Taciroglu. January 2014.
- PEER 2013/26** *Urban Earthquake Engineering. Proceedings of the U.S.-Iran Seismic Workshop.* December 2013.
- PEER 2013/25** *Earthquake Engineering for Resilient Communities: 2013 PEER Internship Program Research Report Collection.* Heidi Tremayne (Editor), Stephen A. Mahin (Editor), Jorge Archbold Monterossa, Matt Brosman, Shelly Dean,

Katherine deLaveaga, Curtis Fong, Donovan Holder, Rakeeb Khan, Elizabeth Jachens, David Lam, Daniela Martinez Lopez, Mara Minner, Geffen Oren, Julia Pavicic, Melissa Quinonez, Lorena Rodriguez, Sean Salazar, Kelli Slaven, Vivian Steyert, Jenny Taing, and Salvador Tena. December 2013.

- PEER 2013/24** *NGA-West2 Ground Motion Prediction Equations for Vertical Ground Motions.* September 2013.
- PEER 2013/23** *Coordinated Planning and Preparedness for Fire Following Major Earthquakes.* Charles Scawthorn. November 2013.
- PEER 2013/22** *GEM-PEER Task 3 Project: Selection of a Global Set of Ground Motion Prediction Equations.* Jonathan P. Stewart, John Douglas, Mohammad B. Javanbarg, Carola Di Alessandro, Yousef Bozorgnia, Norman A. Abrahamson, David M. Boore, Kenneth W. Campbell, Elise Delavaud, Mustafa Erdik and Peter J. Stafford. December 2013.
- PEER 2013/21** *Seismic Design and Performance of Bridges with Columns on Rocking Foundations.* Grigorios Antonellis and Marios Panagiotou. September 2013.
- PEER 2013/20** *Experimental and Analytical Studies on the Seismic Behavior of Conventional and Hybrid Braced Frames.* Jiun-Wei Lai and Stephen A. Mahin. September 2013.
- PEER 2013/19** *Toward Resilient Communities: A Performance-Based Engineering Framework for Design and Evaluation of the Built Environment.* Michael William Mieler, Bozidar Stojadinovic, Robert J. Budnitz, Stephen A. Mahin and Mary C. Comerio. September 2013.
- PEER 2013/18** *Identification of Site Parameters that Improve Predictions of Site Amplification.* Ellen M. Rathje and Sara Navidi. July 2013.
- PEER 2013/17** *Response Spectrum Analysis of Concrete Gravity Dams Including Dam-Water-Foundation Interaction.* Arnkjell Lokke and Anil K. Chopra. July 2013.
- PEER 2013/16** *Effect of hoop reinforcement spacing on the cyclic response of large reinforced concrete special moment frame beams.* Marios Panagiotou, Tea Visnjic, Grigorios Antonellis, Panagiotis Galanis, and Jack P. Moehle. June 2013.
- PEER 2013/15** *A Probabilistic Framework to Include the Effects of Near-Fault Directivity in Seismic Hazard Assessment.* Shrey Kumar Shahi, Jack W. Baker. October 2013.
- PEER 2013/14** *Hanging-Wall Scaling using Finite-Fault Simulations.* Jennifer L. Donahue and Norman A. Abrahamson. September 2013.
- PEER 2013/13** *Semi-Empirical Nonlinear Site Amplification and its Application in NEHRP Site Factors.* Jonathan P. Stewart and Emel Seyhan. November 2013.
- PEER 2013/12** *Nonlinear Horizontal Site Response for the NGA-West2 Project.* Ronnie Kamai, Norman A. Abramson, Walter J. Silva. May 2013.
- PEER 2013/11** *Epistemic Uncertainty for NGA-West2 Models.* Linda Al Atik and Robert R. Youngs. May 2013.
- PEER 2013/10** *NGA-West 2 Models for Ground-Motion Directionality.* Shrey K. Shahi and Jack W. Baker. May 2013.
- PEER 2013/09** *Final Report of the NGA-West2 Directivity Working Group.* Paul Spudich, Jeffrey R. Bayless, Jack W. Baker, Brian S.J. Chiou, Badie Rowshandel, Shrey Shahi, and Paul Somerville. May 2013.
- PEER 2013/08** *NGA-West2 Model for Estimating Average Horizontal Values of Pseudo-Absolute Spectral Accelerations Generated by Crustal Earthquakes.* I. M. Idriss. May 2013.
- PEER 2013/07** *Update of the Chiou and Youngs NGA Ground Motion Model for Average Horizontal Component of Peak Ground Motion and Response Spectra.* Brian Chiou and Robert Youngs. May 2013.
- PEER 2013/06** *NGA-West2 Campbell-Bozorgnia Ground Motion Model for the Horizontal Components of PGA, PGV, and 5%-Damped Elastic Pseudo-Acceleration Response Spectra for Periods Ranging from 0.01 to 10 sec.* Kenneth W. Campbell and Yousef Bozorgnia. May 2013.
- PEER 2013/05** *NGA-West 2 Equations for Predicting Response Spectral Accelerations for Shallow Crustal Earthquakes.* David M. Boore, Jonathan P. Stewart, Emel Seyhan, Gail M. Atkinson. May 2013.
- PEER 2013/04** *Update of the AS08 Ground-Motion Prediction Equations Based on the NGA-West2 Data Set.* Norman Abrahamson, Walter Silva, and Ronnie Kamai. May 2013.
- PEER 2013/03** *PEER NGA-West2 Database.* Timothy D. Ancheta, Robert B. Darragh, Jonathan P. Stewart, Emel Seyhan, Walter J. Silva, Brian S.J. Chiou, Katie E. Wooddell, Robert W. Graves, Albert R. Kottke, David M. Boore, Tadahiro Kishida, and Jennifer L. Donahue. May 2013.
- PEER 2013/02** *Hybrid Simulation of the Seismic Response of Squat Reinforced Concrete Shear Walls.* Catherine A. Whyte and Bozidar Stojadinovic. May 2013.
- PEER 2013/01** *Housing Recovery in Chile: A Qualitative Mid-program Review.* Mary C. Comerio. February 2013.

- PEER 2012/08** *Guidelines for Estimation of Shear Wave Velocity.* Bernard R. Wair, Jason T. DeJong, and Thomas Shantz. December 2012.
- PEER 2012/07** *Earthquake Engineering for Resilient Communities: 2012 PEER Internship Program Research Report Collection.* Heidi Tremayne (Editor), Stephen A. Mahin (Editor), Collin Anderson, Dustin Cook, Michael Erceg, Carlos Esparza, Jose Jimenez, Dorian Krausz, Andrew Lo, Stephanie Lopez, Nicole McCurdy, Paul Shipman, Alexander Strum, Eduardo Vega. December 2012.
- PEER 2012/06** *Fragilities for Precarious Rocks at Yucca Mountain.* Matthew D. Purvance, Rasool Anooshehpour, and James N. Brune. December 2012.
- PEER 2012/05** *Development of Simplified Analysis Procedure for Piles in Laterally Spreading Layered Soils.* Christopher R. McGann, Pedro Arduino, and Peter Mackenzie-Helnwein. December 2012.
- PEER 2012/04** *Unbonded Pre-Tensioned Columns for Bridges in Seismic Regions.* Phillip M. Davis, Todd M. Janes, Marc O. Eberhard, and John F. Stanton. December 2012.
- PEER 2012/03** *Experimental and Analytical Studies on Reinforced Concrete Buildings with Seismically Vulnerable Beam-Column Joints.* Sangjoon Park and Khalid M. Mosalam. October 2012.
- PEER 2012/02** *Seismic Performance of Reinforced Concrete Bridges Allowed to Uplift during Multi-Directional Excitation.* Andres Oscar Espinoza and Stephen A. Mahin. July 2012.
- PEER 2012/01** *Spectral Damping Scaling Factors for Shallow Crustal Earthquakes in Active Tectonic Regions.* Sanaz Rezaeian, Yousef Bozorgnia, I. M. Idriss, Kenneth Campbell, Norman Abrahamson, and Walter Silva. July 2012.
- PEER 2011/10** *Earthquake Engineering for Resilient Communities: 2011 PEER Internship Program Research Report Collection.* Eds. Heidi Faison and Stephen A. Mahin. December 2011.
- PEER 2011/09** *Calibration of Semi-Stochastic Procedure for Simulating High-Frequency Ground Motions.* Jonathan P. Stewart, Emel Seyhan, and Robert W. Graves. December 2011.
- PEER 2011/08** *Water Supply in regard to Fire Following Earthquake.* Charles Scawthorn. November 2011.
- PEER 2011/07** *Seismic Risk Management in Urban Areas. Proceedings of a U.S.-Iran-Turkey Seismic Workshop.* September 2011.
- PEER 2011/06** *The Use of Base Isolation Systems to Achieve Complex Seismic Performance Objectives.* Troy A. Morgan and Stephen A. Mahin. July 2011.
- PEER 2011/05** *Case Studies of the Seismic Performance of Tall Buildings Designed by Alternative Means.* Task 12 Report for the Tall Buildings Initiative. Jack Moehle, Yousef Bozorgnia, Nirmal Jayaram, Pierson Jones, Mohsen Rahnama, Nilesh Shome, Zeynep Tuna, John Wallace, Tony Yang, and Farzin Zareian. July 2011.
- PEER 2011/04** *Recommended Design Practice for Pile Foundations in Laterally Spreading Ground.* Scott A. Ashford, Ross W. Boulanger, and Scott J. Brandenburg. June 2011.
- PEER 2011/03** *New Ground Motion Selection Procedures and Selected Motions for the PEER Transportation Research Program.* Jack W. Baker, Ting Lin, Shrey K. Shahi, and Nirmal Jayaram. March 2011.
- PEER 2011/02** *A Bayesian Network Methodology for Infrastructure Seismic Risk Assessment and Decision Support.* Michelle T. Bensi, Armen Der Kiureghian, and Daniel Straub. March 2011.
- PEER 2011/01** *Demand Fragility Surfaces for Bridges in Liquefied and Laterally Spreading Ground.* Scott J. Brandenburg, Jian Zhang, Pirooz Kashighandi, Yili Huo, and Minxing Zhao. March 2011.
- PEER 2010/05** *Guidelines for Performance-Based Seismic Design of Tall Buildings.* Developed by the Tall Buildings Initiative. November 2010.
- PEER 2010/04** *Application Guide for the Design of Flexible and Rigid Bus Connections between Substation Equipment Subjected to Earthquakes.* Jean-Bernard Dastous and Armen Der Kiureghian. September 2010.
- PEER 2010/03** *Shear Wave Velocity as a Statistical Function of Standard Penetration Test Resistance and Vertical Effective Stress at Caltrans Bridge Sites.* Scott J. Brandenburg, Naresh Bellana, and Thomas Shantz. June 2010.
- PEER 2010/02** *Stochastic Modeling and Simulation of Ground Motions for Performance-Based Earthquake Engineering.* Sanaz Rezaeian and Armen Der Kiureghian. June 2010.
- PEER 2010/01** *Structural Response and Cost Characterization of Bridge Construction Using Seismic Performance Enhancement Strategies.* Ady Aviram, Božidar Stojadinović, Gustavo J. Parra-Montesinos, and Kevin R. Mackie. March 2010.
- PEER 2009/03** *The Integration of Experimental and Simulation Data in the Study of Reinforced Concrete Bridge Systems Including Soil-Foundation-Structure Interaction.* Matthew Dryden and Gregory L. Fenves. November 2009.
- PEER 2009/02** *Improving Earthquake Mitigation through Innovations and Applications in Seismic Science, Engineering, Communication, and Response. Proceedings of a U.S.-Iran Seismic Workshop.* October 2009.

- PEER 2009/01** *Evaluation of Ground Motion Selection and Modification Methods: Predicting Median Interstory Drift Response of Buildings.* Curt B. Haselton, Ed. June 2009.
- PEER 2008/10** *Technical Manual for Strata.* Albert R. Kottke and Ellen M. Rathje. February 2009.
- PEER 2008/09** *NGA Model for Average Horizontal Component of Peak Ground Motion and Response Spectra.* Brian S.-J. Chiou and Robert R. Youngs. November 2008.
- PEER 2008/08** *Toward Earthquake-Resistant Design of Concentrically Braced Steel Structures.* Patxi Uriz and Stephen A. Mahin. November 2008.
- PEER 2008/07** *Using OpenSees for Performance-Based Evaluation of Bridges on Liquefiable Soils.* Stephen L. Kramer, Pedro Arduino, and HyungSuk Shin. November 2008.
- PEER 2008/06** *Shaking Table Tests and Numerical Investigation of Self-Centering Reinforced Concrete Bridge Columns.* Hyung IL Jeong, Junichi Sakai, and Stephen A. Mahin. September 2008.
- PEER 2008/05** *Performance-Based Earthquake Engineering Design Evaluation Procedure for Bridge Foundations Undergoing Liquefaction-Induced Lateral Ground Displacement.* Christian A. Ledezma and Jonathan D. Bray. August 2008.
- PEER 2008/04** *Benchmarking of Nonlinear Geotechnical Ground Response Analysis Procedures.* Jonathan P. Stewart, Annie On-Lei Kwok, Youssef M. A. Hashash, Neven Matasovic, Robert Pyke, Zhiliang Wang, and Zhaohui Yang. August 2008.
- PEER 2008/03** *Guidelines for Nonlinear Analysis of Bridge Structures in California.* Ady Aviram, Kevin R. Mackie, and Božidar Stojadinović. August 2008.
- PEER 2008/02** *Treatment of Uncertainties in Seismic-Risk Analysis of Transportation Systems.* Evangelos Stergiou and Anne S. Kiremidjian. July 2008.
- PEER 2008/01** *Seismic Performance Objectives for Tall Buildings.* William T. Holmes, Charles Kircher, William Petak, and Nabih Youssef. August 2008.
- PEER 2007/12** *An Assessment to Benchmark the Seismic Performance of a Code-Conforming Reinforced Concrete Moment-Frame Building.* Curt Haselton, Christine A. Goulet, Judith Mitrani-Reiser, James L. Beck, Gregory G. Deierlein, Keith A. Porter, Jonathan P. Stewart, and Ertugrul Taciroglu. August 2008.
- PEER 2007/11** *Bar Buckling in Reinforced Concrete Bridge Columns.* Wayne A. Brown, Dawn E. Lehman, and John F. Stanton. February 2008.
- PEER 2007/10** *Computational Modeling of Progressive Collapse in Reinforced Concrete Frame Structures.* Mohamed M. Talaat and Khalid M. Mosalam. May 2008.
- PEER 2007/09** *Integrated Probabilistic Performance-Based Evaluation of Benchmark Reinforced Concrete Bridges.* Kevin R. Mackie, John-Michael Wong, and Božidar Stojadinović. January 2008.
- PEER 2007/08** *Assessing Seismic Collapse Safety of Modern Reinforced Concrete Moment-Frame Buildings.* Curt B. Haselton and Gregory G. Deierlein. February 2008.
- PEER 2007/07** *Performance Modeling Strategies for Modern Reinforced Concrete Bridge Columns.* Michael P. Berry and Marc O. Eberhard. April 2008.
- PEER 2007/06** *Development of Improved Procedures for Seismic Design of Buried and Partially Buried Structures.* Linda Al Atik and Nicholas Sitar. June 2007.
- PEER 2007/05** *Uncertainty and Correlation in Seismic Risk Assessment of Transportation Systems.* Renee G. Lee and Anne S. Kiremidjian. July 2007.
- PEER 2007/04** *Numerical Models for Analysis and Performance-Based Design of Shallow Foundations Subjected to Seismic Loading.* Sivapalan Gajan, Tara C. Hutchinson, Bruce L. Kutter, Prishati Raychowdhury, José A. Ugalde, and Jonathan P. Stewart. May 2008.
- PEER 2007/03** *Beam-Column Element Model Calibrated for Predicting Flexural Response Leading to Global Collapse of RC Frame Buildings.* Curt B. Haselton, Abbie B. Liel, Sarah Taylor Lange, and Gregory G. Deierlein. May 2008.
- PEER 2007/02** *Campbell-Bozorgnia NGA Ground Motion Relations for the Geometric Mean Horizontal Component of Peak and Spectral Ground Motion Parameters.* Kenneth W. Campbell and Yousef Bozorgnia. May 2007.
- PEER 2007/01** *Boore-Atkinson NGA Ground Motion Relations for the Geometric Mean Horizontal Component of Peak and Spectral Ground Motion Parameters.* David M. Boore and Gail M. Atkinson. May 2007.
- PEER 2006/12** *Societal Implications of Performance-Based Earthquake Engineering.* Peter J. May. May 2007.
- PEER 2006/11** *Probabilistic Seismic Demand Analysis Using Advanced Ground Motion Intensity Measures, Attenuation Relationships, and Near-Fault Effects.* Polsak Tothong and C. Allin Cornell. March 2007.

- PEER 2006/10** *Application of the PEER PBEE Methodology to the I-880 Viaduct.* Sashi Kunnath. February 2007.
- PEER 2006/09** *Quantifying Economic Losses from Travel Forgone Following a Large Metropolitan Earthquake.* James Moore, Sungbin Cho, Yue Yue Fan, and Stuart Werner. November 2006.
- PEER 2006/08** *Vector-Valued Ground Motion Intensity Measures for Probabilistic Seismic Demand Analysis.* Jack W. Baker and C. Allin Cornell. October 2006.
- PEER 2006/07** *Analytical Modeling of Reinforced Concrete Walls for Predicting Flexural and Coupled–Shear-Flexural Responses.* Kutay Orakcal, Leonardo M. Massone, and John W. Wallace. October 2006.
- PEER 2006/06** *Nonlinear Analysis of a Soil-Drilled Pier System under Static and Dynamic Axial Loading.* Gang Wang and Nicholas Sitar. November 2006.
- PEER 2006/05** *Advanced Seismic Assessment Guidelines.* Paolo Bazzurro, C. Allin Cornell, Charles Menun, Maziar Motahari, and Nicolas Luco. September 2006.
- PEER 2006/04** *Probabilistic Seismic Evaluation of Reinforced Concrete Structural Components and Systems.* Tae Hyung Lee and Khalid M. Mosalam. August 2006.
- PEER 2006/03** *Performance of Lifelines Subjected to Lateral Spreading.* Scott A. Ashford and Teerawat Juirnarongrit. July 2006.
- PEER 2006/02** *Pacific Earthquake Engineering Research Center Highway Demonstration Project.* Anne Kiremidjian, James Moore, Yue Yue Fan, Nesrin Basoz, Ozgur Yazali, and Meredith Williams. April 2006.
- PEER 2006/01** *Bracing Berkeley. A Guide to Seismic Safety on the UC Berkeley Campus.* Mary C. Comerio, Stephen Tobriner, and Ariane Fehrenkamp. January 2006.
- PEER 2005/16** *Seismic Response and Reliability of Electrical Substation Equipment and Systems.* Junho Song, Armen Der Kiureghian, and Jerome L. Sackman. April 2006.
- PEER 2005/15** *CPT-Based Probabilistic Assessment of Seismic Soil Liquefaction Initiation.* R. E. S. Moss, R. B. Seed, R. E. Kayen, J. P. Stewart, and A. Der Kiureghian. April 2006.
- PEER 2005/14** *Workshop on Modeling of Nonlinear Cyclic Load-Deformation Behavior of Shallow Foundations.* Bruce L. Kutter, Geoffrey Martin, Tara Hutchinson, Chad Harden, Sivapalan Gajan, and Justin Phalen. March 2006.
- PEER 2005/13** *Stochastic Characterization and Decision Bases under Time-Dependent Aftershock Risk in Performance-Based Earthquake Engineering.* Gee Liek Yeo and C. Allin Cornell. July 2005.
- PEER 2005/12** *PEER Testbed Study on a Laboratory Building: Exercising Seismic Performance Assessment.* Mary C. Comerio, editor. November 2005.
- PEER 2005/11** *Van Nuys Hotel Building Testbed Report: Exercising Seismic Performance Assessment.* Helmut Krawinkler, editor. October 2005.
- PEER 2005/10** *First NEES/E-Defense Workshop on Collapse Simulation of Reinforced Concrete Building Structures.* September 2005.
- PEER 2005/09** *Test Applications of Advanced Seismic Assessment Guidelines.* Joe Maffei, Karl Telleen, Danya Mohr, William Holmes, and Yuki Nakayama. August 2006.
- PEER 2005/08** *Damage Accumulation in Lightly Confined Reinforced Concrete Bridge Columns.* R. Tyler Ranf, Jared M. Nelson, Zach Price, Marc O. Eberhard, and John F. Stanton. April 2006.
- PEER 2005/07** *Experimental and Analytical Studies on the Seismic Response of Freestanding and Anchored Laboratory Equipment.* Dimitrios Konstantinidis and Nicos Makris. January 2005.
- PEER 2005/06** *Global Collapse of Frame Structures under Seismic Excitations.* Luis F. Ibarra and Helmut Krawinkler. September 2005.
- PEER 2005/05** *Performance Characterization of Bench- and Shelf-Mounted Equipment.* Samit Ray Chaudhuri and Tara C. Hutchinson. May 2006.
- PEER 2005/04** *Numerical Modeling of the Nonlinear Cyclic Response of Shallow Foundations.* Chad Harden, Tara Hutchinson, Geoffrey R. Martin, and Bruce L. Kutter. August 2005.
- PEER 2005/03** *A Taxonomy of Building Components for Performance-Based Earthquake Engineering.* Keith A. Porter. September 2005.
- PEER 2005/02** *Fragility Basis for California Highway Overpass Bridge Seismic Decision Making.* Kevin R. Mackie and Božidar Stojadinović. June 2005.
- PEER 2005/01** *Empirical Characterization of Site Conditions on Strong Ground Motion.* Jonathan P. Stewart, Yoojoong Choi, and Robert W. Graves. June 2005.

- PEER 2004/09** *Electrical Substation Equipment Interaction: Experimental Rigid Conductor Studies.* Christopher Stearns and André Filiatrault. February 2005.
- PEER 2004/08** *Seismic Qualification and Fragility Testing of Line Break 550-kV Disconnect Switches.* Shakhzod M. Takhirov, Gregory L. Fenves, and Eric Fujisaki. January 2005.
- PEER 2004/07** *Ground Motions for Earthquake Simulator Qualification of Electrical Substation Equipment.* Shakhzod M. Takhirov, Gregory L. Fenves, Eric Fujisaki, and Don Clyde. January 2005.
- PEER 2004/06** *Performance-Based Regulation and Regulatory Regimes.* Peter J. May and Chris Koski. September 2004.
- PEER 2004/05** *Performance-Based Seismic Design Concepts and Implementation: Proceedings of an International Workshop.* Peter Fajfar and Helmut Krawinkler, editors. September 2004.
- PEER 2004/04** *Seismic Performance of an Instrumented Tilt-up Wall Building.* James C. Anderson and Vitelmo V. Bertero. July 2004.
- PEER 2004/03** *Evaluation and Application of Concrete Tilt-up Assessment Methodologies.* Timothy Graf and James O. Malley. October 2004.
- PEER 2004/02** *Analytical Investigations of New Methods for Reducing Residual Displacements of Reinforced Concrete Bridge Columns.* Junichi Sakai and Stephen A. Mahin. August 2004.
- PEER 2004/01** *Seismic Performance of Masonry Buildings and Design Implications.* Kerri Anne Taeko Tokoro, James C. Anderson, and Vitelmo V. Bertero. February 2004.
- PEER 2003/18** *Performance Models for Flexural Damage in Reinforced Concrete Columns.* Michael Berry and Marc Eberhard. August 2003.
- PEER 2003/17** *Predicting Earthquake Damage in Older Reinforced Concrete Beam-Column Joints.* Catherine Pagni and Laura Lowes. October 2004.
- PEER 2003/16** *Seismic Demands for Performance-Based Design of Bridges.* Kevin Mackie and Božidar Stojadinović. August 2003.
- PEER 2003/15** *Seismic Demands for Nondeteriorating Frame Structures and Their Dependence on Ground Motions.* Ricardo Antonio Medina and Helmut Krawinkler. May 2004.
- PEER 2003/14** *Finite Element Reliability and Sensitivity Methods for Performance-Based Earthquake Engineering.* Terje Haukaas and Armen Der Kiureghian. April 2004.
- PEER 2003/13** *Effects of Connection Hysteretic Degradation on the Seismic Behavior of Steel Moment-Resisting Frames.* Janise E. Rodgers and Stephen A. Mahin. March 2004.
- PEER 2003/12** *Implementation Manual for the Seismic Protection of Laboratory Contents: Format and Case Studies.* William T. Holmes and Mary C. Comerio. October 2003.
- PEER 2003/11** *Fifth U.S.-Japan Workshop on Performance-Based Earthquake Engineering Methodology for Reinforced Concrete Building Structures.* February 2004.
- PEER 2003/10** *A Beam-Column Joint Model for Simulating the Earthquake Response of Reinforced Concrete Frames.* Laura N. Lowes, Nilanjan Mitra, and Arash Altoontash. February 2004.
- PEER 2003/09** *Sequencing Repairs after an Earthquake: An Economic Approach.* Marco Casari and Simon J. Wilkie. April 2004.
- PEER 2003/08** *A Technical Framework for Probability-Based Demand and Capacity Factor Design (DCFD) Seismic Formats.* Fatemeh Jalayer and C. Allin Cornell. November 2003.
- PEER 2003/07** *Uncertainty Specification and Propagation for Loss Estimation Using FOSM Methods.* Jack W. Baker and C. Allin Cornell. September 2003.
- PEER 2003/06** *Performance of Circular Reinforced Concrete Bridge Columns under Bidirectional Earthquake Loading.* Mahmoud M. Hachem, Stephen A. Mahin, and Jack P. Moehle. February 2003.
- PEER 2003/05** *Response Assessment for Building-Specific Loss Estimation.* Eduardo Miranda and Shahram Taghavi. September 2003.
- PEER 2003/04** *Experimental Assessment of Columns with Short Lap Splices Subjected to Cyclic Loads.* Murat Melek, John W. Wallace, and Joel Conte. April 2003.
- PEER 2003/03** *Probabilistic Response Assessment for Building-Specific Loss Estimation.* Eduardo Miranda and Hesameddin Aslani. September 2003.
- PEER 2003/02** *Software Framework for Collaborative Development of Nonlinear Dynamic Analysis Program.* Jun Peng and Kincho H. Law. September 2003.

- PEER 2003/01** *Shake Table Tests and Analytical Studies on the Gravity Load Collapse of Reinforced Concrete Frames.* Kenneth John Elwood and Jack P. Moehle. November 2003.
- PEER 2002/24** *Performance of Beam to Column Bridge Joints Subjected to a Large Velocity Pulse.* Natalie Gibson, André Filiatrault, and Scott A. Ashford. April 2002.
- PEER 2002/23** *Effects of Large Velocity Pulses on Reinforced Concrete Bridge Columns.* Greg L. Orozco and Scott A. Ashford. April 2002.
- PEER 2002/22** *Characterization of Large Velocity Pulses for Laboratory Testing.* Kenneth E. Cox and Scott A. Ashford. April 2002.
- PEER 2002/21** *Fourth U.S.-Japan Workshop on Performance-Based Earthquake Engineering Methodology for Reinforced Concrete Building Structures.* December 2002.
- PEER 2002/20** *Barriers to Adoption and Implementation of PBEE Innovations.* Peter J. May. August 2002.
- PEER 2002/19** *Economic-Engineered Integrated Models for Earthquakes: Socioeconomic Impacts.* Peter Gordon, James E. Moore II, and Harry W. Richardson. July 2002.
- PEER 2002/18** *Assessment of Reinforced Concrete Building Exterior Joints with Substandard Details.* Chris P. Pantelides, Jon Hansen, Justin Nadauld, and Lawrence D. Reaveley. May 2002.
- PEER 2002/17** *Structural Characterization and Seismic Response Analysis of a Highway Overcrossing Equipped with Elastomeric Bearings and Fluid Dampers: A Case Study.* Nicos Makris and Jian Zhang. November 2002.
- PEER 2002/16** *Estimation of Uncertainty in Geotechnical Properties for Performance-Based Earthquake Engineering.* Allen L. Jones, Steven L. Kramer, and Pedro Arduino. December 2002.
- PEER 2002/15** *Seismic Behavior of Bridge Columns Subjected to Various Loading Patterns.* Asadollah Esmaeily-Gh. and Yan Xiao. December 2002.
- PEER 2002/14** *Inelastic Seismic Response of Extended Pile Shaft Supported Bridge Structures.* T.C. Hutchinson, R.W. Boulanger, Y.H. Chai, and I.M. Idriss. December 2002.
- PEER 2002/13** *Probabilistic Models and Fragility Estimates for Bridge Components and Systems.* Paolo Gardoni, Armen Der Kiureghian, and Khalid M. Mosalam. June 2002.
- PEER 2002/12** *Effects of Fault Dip and Slip Rake on Near-Source Ground Motions: Why Chi-Chi Was a Relatively Mild M7.6 Earthquake.* Brad T. Aagaard, John F. Hall, and Thomas H. Heaton. December 2002.
- PEER 2002/11** *Analytical and Experimental Study of Fiber-Reinforced Strip Isolators.* James M. Kelly and Shakhzod M. Takhirov. September 2002.
- PEER 2002/10** *Centrifuge Modeling of Settlement and Lateral Spreading with Comparisons to Numerical Analyses.* Sivapalan Gajan and Bruce L. Kutter. January 2003.
- PEER 2002/09** *Documentation and Analysis of Field Case Histories of Seismic Compression during the 1994 Northridge, California, Earthquake.* Jonathan P. Stewart, Patrick M. Smith, Daniel H. Whang, and Jonathan D. Bray. October 2002.
- PEER 2002/08** *Component Testing, Stability Analysis and Characterization of Buckling-Restrained Unbonded Braces™.* Cameron Black, Nicos Makris, and Ian Aiken. September 2002.
- PEER 2002/07** *Seismic Performance of Pile-Wharf Connections.* Charles W. Roeder, Robert Graff, Jennifer Soderstrom, and Jun Han Yoo. December 2001.
- PEER 2002/06** *The Use of Benefit-Cost Analysis for Evaluation of Performance-Based Earthquake Engineering Decisions.* Richard O. Zerbe and Anthony Falit-Baiamonte. September 2001.
- PEER 2002/05** *Guidelines, Specifications, and Seismic Performance Characterization of Nonstructural Building Components and Equipment.* André Filiatrault, Constantin Christopoulos, and Christopher Stearns. September 2001.
- PEER 2002/04** *Consortium of Organizations for Strong-Motion Observation Systems and the Pacific Earthquake Engineering Research Center Lifelines Program: Invited Workshop on Archiving and Web Dissemination of Geotechnical Data, 4–5 October 2001.* September 2002.
- PEER 2002/03** *Investigation of Sensitivity of Building Loss Estimates to Major Uncertain Variables for the Van Nuys Testbed.* Keith A. Porter, James L. Beck, and Rustem V. Shaikhutdinov. August 2002.
- PEER 2002/02** *The Third U.S.-Japan Workshop on Performance-Based Earthquake Engineering Methodology for Reinforced Concrete Building Structures.* July 2002.
- PEER 2002/01** *Nonstructural Loss Estimation: The UC Berkeley Case Study.* Mary C. Comerio and John C. Stallmeyer. December 2001.

- PEER 2001/16** *Statistics of SDF-System Estimate of Roof Displacement for Pushover Analysis of Buildings.* Anil K. Chopra, Rakesh K. Goel, and Chatpan Chintanapakdee. December 2001.
- PEER 2001/15** *Damage to Bridges during the 2001 Nisqually Earthquake.* R. Tyler Ranf, Marc O. Eberhard, and Michael P. Berry. November 2001.
- PEER 2001/14** *Rocking Response of Equipment Anchored to a Base Foundation.* Nicos Makris and Cameron J. Black. September 2001.
- PEER 2001/13** *Modeling Soil Liquefaction Hazards for Performance-Based Earthquake Engineering.* Steven L. Kramer and Ahmed-W. Elgamal. February 2001.
- PEER 2001/12** *Development of Geotechnical Capabilities in OpenSees.* Boris Jeremić. September 2001.
- PEER 2001/11** *Analytical and Experimental Study of Fiber-Reinforced Elastomeric Isolators.* James M. Kelly and Shakhzod M. Takhirov. September 2001.
- PEER 2001/10** *Amplification Factors for Spectral Acceleration in Active Regions.* Jonathan P. Stewart, Andrew H. Liu, Yoojoong Choi, and Mehmet B. Baturay. December 2001.
- PEER 2001/09** *Ground Motion Evaluation Procedures for Performance-Based Design.* Jonathan P. Stewart, Shyh-Jeng Chiou, Jonathan D. Bray, Robert W. Graves, Paul G. Somerville, and Norman A. Abrahamson. September 2001.
- PEER 2001/08** *Experimental and Computational Evaluation of Reinforced Concrete Bridge Beam-Column Connections for Seismic Performance.* Clay J. Naito, Jack P. Moehle, and Khalid M. Mosalam. November 2001.
- PEER 2001/07** *The Rocking Spectrum and the Shortcomings of Design Guidelines.* Nicos Makris and Dimitrios Konstantinidis. August 2001.
- PEER 2001/06** *Development of an Electrical Substation Equipment Performance Database for Evaluation of Equipment Fragilities.* Thalia Agnanos. April 1999.
- PEER 2001/05** *Stiffness Analysis of Fiber-Reinforced Elastomeric Isolators.* Hsiang-Chuan Tsai and James M. Kelly. May 2001.
- PEER 2001/04** *Organizational and Societal Considerations for Performance-Based Earthquake Engineering.* Peter J. May. April 2001.
- PEER 2001/03** *A Modal Pushover Analysis Procedure to Estimate Seismic Demands for Buildings: Theory and Preliminary Evaluation.* Anil K. Chopra and Rakesh K. Goel. January 2001.
- PEER 2001/02** *Seismic Response Analysis of Highway Overcrossings Including Soil-Structure Interaction.* Jian Zhang and Nicos Makris. March 2001.
- PEER 2001/01** *Experimental Study of Large Seismic Steel Beam-to-Column Connections.* Egor P. Popov and Shakhzod M. Takhirov. November 2000.
- PEER 2000/10** *The Second U.S.-Japan Workshop on Performance-Based Earthquake Engineering Methodology for Reinforced Concrete Building Structures.* March 2000.
- PEER 2000/09** *Structural Engineering Reconnaissance of the August 17, 1999 Earthquake: Kocaeli (Izmit), Turkey.* Halil Sezen, Kenneth J. Elwood, Andrew S. Whittaker, Khalid Mosalam, John J. Wallace, and John F. Stanton. December 2000.
- PEER 2000/08** *Behavior of Reinforced Concrete Bridge Columns Having Varying Aspect Ratios and Varying Lengths of Confinement.* Anthony J. Calderone, Dawn E. Lehman, and Jack P. Moehle. January 2001.
- PEER 2000/07** *Cover-Plate and Flange-Plate Reinforced Steel Moment-Resisting Connections.* Taejin Kim, Andrew S. Whittaker, Amir S. Gilani, Vitelmo V. Bertero, and Shakhzod M. Takhirov. September 2000.
- PEER 2000/06** *Seismic Evaluation and Analysis of 230-kV Disconnect Switches.* Amir S. J. Gilani, Andrew S. Whittaker, Gregory L. Fenves, Chun-Hao Chen, Henry Ho, and Eric Fujisaki. July 2000.
- PEER 2000/05** *Performance-Based Evaluation of Exterior Reinforced Concrete Building Joints for Seismic Excitation.* Chandra Clyde, Chris P. Pantelides, and Lawrence D. Reaveley. July 2000.
- PEER 2000/04** *An Evaluation of Seismic Energy Demand: An Attenuation Approach.* Chung-Che Chou and Chia-Ming Uang. July 1999.
- PEER 2000/03** *Framing Earthquake Retrofitting Decisions: The Case of Hillside Homes in Los Angeles.* Detlof von Winterfeldt, Nels Roselund, and Alicia Kitsuse. March 2000.
- PEER 2000/02** *U.S.-Japan Workshop on the Effects of Near-Field Earthquake Shaking.* Andrew Whittaker, ed. July 2000.
- PEER 2000/01** *Further Studies on Seismic Interaction in Interconnected Electrical Substation Equipment.* Armen Der Kiureghian, Kee-Jeung Hong, and Jerome L. Sackman. November 1999.

- PEER 1999/14** *Seismic Evaluation and Retrofit of 230-kV Porcelain Transformer Bushings.* Amir S. Gilani, Andrew S. Whittaker, Gregory L. Fenves, and Eric Fujisaki. December 1999.
- PEER 1999/13** *Building Vulnerability Studies: Modeling and Evaluation of Tilt-up and Steel Reinforced Concrete Buildings.* John W. Wallace, Jonathan P. Stewart, and Andrew S. Whittaker, editors. December 1999.
- PEER 1999/12** *Rehabilitation of Nonductile RC Frame Building Using Encasement Plates and Energy-Dissipating Devices.* Mehrdad Sasani, Vitelmo V. Bertero, James C. Anderson. December 1999.
- PEER 1999/11** *Performance Evaluation Database for Concrete Bridge Components and Systems under Simulated Seismic Loads.* Yael D. Hose and Frieder Seible. November 1999.
- PEER 1999/10** *U.S.-Japan Workshop on Performance-Based Earthquake Engineering Methodology for Reinforced Concrete Building Structures.* December 1999.
- PEER 1999/09** *Performance Improvement of Long Period Building Structures Subjected to Severe Pulse-Type Ground Motions.* James C. Anderson, Vitelmo V. Bertero, and Raul Bertero. October 1999.
- PEER 1999/08** *Envelopes for Seismic Response Vectors.* Charles Menun and Armen Der Kiureghian. July 1999.
- PEER 1999/07** *Documentation of Strengths and Weaknesses of Current Computer Analysis Methods for Seismic Performance of Reinforced Concrete Members.* William F. Cofer. November 1999.
- PEER 1999/06** *Rocking Response and Overturning of Anchored Equipment under Seismic Excitations.* Nicos Makris and Jian Zhang. November 1999.
- PEER 1999/05** *Seismic Evaluation of 550 kV Porcelain Transformer Bushings.* Amir S. Gilani, Andrew S. Whittaker, Gregory L. Fenves, and Eric Fujisaki. October 1999.
- PEER 1999/04** *Adoption and Enforcement of Earthquake Risk-Reduction Measures.* Peter J. May, Raymond J. Burby, T. Jens Feeley, and Robert Wood.
- PEER 1999/03** *Task 3 Characterization of Site Response General Site Categories.* Adrian Rodriguez-Marek, Jonathan D. Bray, and Norman Abrahamson. February 1999.
- PEER 1999/02** *Capacity-Demand-Diagram Methods for Estimating Seismic Deformation of Inelastic Structures: SDF Systems.* Anil K. Chopra and Rakesh Goel. April 1999.
- PEER 1999/01** *Interaction in Interconnected Electrical Substation Equipment Subjected to Earthquake Ground Motions.* Armen Der Kiureghian, Jerome L. Sackman, and Kee-Jeung Hong. February 1999.
- PEER 1998/08** *Behavior and Failure Analysis of a Multiple-Frame Highway Bridge in the 1994 Northridge Earthquake.* Gregory L. Fenves and Michael Ellery. December 1998.
- PEER 1998/07** *Empirical Evaluation of Inertial Soil-Structure Interaction Effects.* Jonathan P. Stewart, Raymond B. Seed, and Gregory L. Fenves. November 1998.
- PEER 1998/06** *Effect of Damping Mechanisms on the Response of Seismic Isolated Structures.* Nicos Makris and Shih-Po Chang. November 1998.
- PEER 1998/05** *Rocking Response and Overturning of Equipment under Horizontal Pulse-Type Motions.* Nicos Makris and Yiannis Roussos. October 1998.
- PEER 1998/04** *Pacific Earthquake Engineering Research Invitational Workshop Proceedings, May 14–15, 1998: Defining the Links between Planning, Policy Analysis, Economics and Earthquake Engineering.* Mary Comerio and Peter Gordon. September 1998.
- PEER 1998/03** *Repair/Upgrade Procedures for Welded Beam to Column Connections.* James C. Anderson and Xiaojing Duan. May 1998.
- PEER 1998/02** *Seismic Evaluation of 196 kV Porcelain Transformer Bushings.* Amir S. Gilani, Juan W. Chavez, Gregory L. Fenves, and Andrew S. Whittaker. May 1998.
- PEER 1998/01** *Seismic Performance of Well-Confined Concrete Bridge Columns.* Dawn E. Lehman and Jack P. Moehle. December 2000.

ONLINE PEER REPORTS

The following PEER reports are available by Internet only at http://peer.berkeley.edu/publications/peer_reports_complete.html.

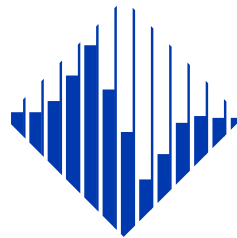
- PEER 2012/103** *Performance-Based Seismic Demand Assessment of Concentrically Braced Steel Frame Buildings*. Chui-Hsin Chen and Stephen A. Mahin. December 2012.
- PEER 2012/102** *Procedure to Restart an Interrupted Hybrid Simulation: Addendum to PEER Report 2010/103*. Vesna Terzic and Božidar Stojadinovic. October 2012.
- PEER 2012/101** *Mechanics of Fiber Reinforced Bearings*. James M. Kelly and Andrea Calabrese. February 2012.
- PEER 2011/107** *Nonlinear Site Response and Seismic Compression at Vertical Array Strongly Shaken by 2007 Niigata-ken Chuetsu-oki Earthquake*. Eric Yee, Jonathan P. Stewart, and Kohji Tokimatsu. December 2011.
- PEER 2011/106** *Self Compacting Hybrid Fiber Reinforced Concrete Composites for Bridge Columns*. Pardeep Kumar, Gabriel Jen, William Trono, Marios Panagiotou, and Claudia Ostertag. September 2011.
- PEER 2011/105** *Stochastic Dynamic Analysis of Bridges Subjected to Spatially Varying Ground Motions*. Katerina Konakli and Armen Der Kiureghian. August 2011.
- PEER 2011/104** *Design and Instrumentation of the 2010 E-Defense Four-Story Reinforced Concrete and Post-Tensioned Concrete Buildings*. Takuya Nagae, Kenichi Tahara, Taizo Matsumori, Hitoshi Shiohara, Toshimi Kabeyasawa, Susumu Kono, Minehiro Nishiyama (Japanese Research Team) and John Wallace, Wassim Ghannoum, Jack Moehle, Richard Sause, Wesley Keller, Zeynep Tuna (U.S. Research Team). June 2011.
- PEER 2011/103** *In-Situ Monitoring of the Force Output of Fluid Dampers: Experimental Investigation*. Dimitrios Konstantinidis, James M. Kelly, and Nicos Makris. April 2011.
- PEER 2011/102** *Ground-motion prediction equations 1964 - 2010*. John Douglas. April 2011.
- PEER 2011/101** *Report of the Eighth Planning Meeting of NEES/E-Defense Collaborative Research on Earthquake Engineering*. Convened by the Hyogo Earthquake Engineering Research Center (NIED), NEES Consortium, Inc. February 2011.
- PEER 2010/111** *Modeling and Acceptance Criteria for Seismic Design and Analysis of Tall Buildings*. Task 7 Report for the Tall Buildings Initiative - Published jointly by the Applied Technology Council. October 2010.
- PEER 2010/110** *Seismic Performance Assessment and Probabilistic Repair Cost Analysis of Precast Concrete Cladding Systems for Multistory Buildings*. Jeffrey P. Hunt and Božidar Stojadinovic. November 2010.
- PEER 2010/109** *Report of the Seventh Joint Planning Meeting of NEES/E-Defense Collaboration on Earthquake Engineering. Held at the E-Defense, Miki, and Shin-Kobe, Japan, September 18–19, 2009*. August 2010.
- PEER 2010/108** *Probabilistic Tsunami Hazard in California*. Hong Kie Thio, Paul Somerville, and Jascha Polet, preparers. October 2010.
- PEER 2010/107** *Performance and Reliability of Exposed Column Base Plate Connections for Steel Moment-Resisting Frames*. Ady Aviram, Božidar Stojadinovic, and Armen Der Kiureghian. August 2010.
- PEER 2010/106** *Verification of Probabilistic Seismic Hazard Analysis Computer Programs*. Patricia Thomas, Ivan Wong, and Norman Abrahamson. May 2010.
- PEER 2010/105** *Structural Engineering Reconnaissance of the April 6, 2009, Abruzzo, Italy, Earthquake, and Lessons Learned*. M. Selim Günay and Khalid M. Mosalam. April 2010.
- PEER 2010/104** *Simulating the Inelastic Seismic Behavior of Steel Braced Frames, Including the Effects of Low-Cycle Fatigue*. Yuli Huang and Stephen A. Mahin. April 2010.
- PEER 2010/103** *Post-Earthquake Traffic Capacity of Modern Bridges in California*. Vesna Terzic and Božidar Stojadinović. March 2010.
- PEER 2010/102** *Analysis of Cumulative Absolute Velocity (CAV) and JMA Instrumental Seismic Intensity (I_{JMA}) Using the PEER-NGA Strong Motion Database*. Kenneth W. Campbell and Yousef Bozorgnia. February 2010.
- PEER 2010/101** *Rocking Response of Bridges on Shallow Foundations*. Jose A. Ugalde, Bruce L. Kutter, and Boris Jeremic. April 2010.
- PEER 2009/109** *Simulation and Performance-Based Earthquake Engineering Assessment of Self-Centering Post-Tensioned Concrete Bridge Systems*. Won K. Lee and Sarah L. Billington. December 2009.
- PEER 2009/108** *PEER Lifelines Geotechnical Virtual Data Center*. J. Carl Stepp, Daniel J. Ponti, Loren L. Turner, Jennifer N. Swift, Sean Devlin, Yang Zhu, Jean Benoit, and John Bobbitt. September 2009.
- PEER 2009/107** *Experimental and Computational Evaluation of Current and Innovative In-Span Hinge Details in Reinforced Concrete Box-Girder Bridges: Part 2: Post-Test Analysis and Design Recommendations*. Matias A. Hube and Khalid M. Mosalam. December 2009.

- PEER 2009/106** *Shear Strength Models of Exterior Beam-Column Joints without Transverse Reinforcement.* Sangjoon Park and Khalid M. Mosalam. November 2009.
- PEER 2009/105** *Reduced Uncertainty of Ground Motion Prediction Equations through Bayesian Variance Analysis.* Robb Eric S. Moss. November 2009.
- PEER 2009/104** *Advanced Implementation of Hybrid Simulation.* Andreas H. Schellenberg, Stephen A. Mahin, Gregory L. Fenves. November 2009.
- PEER 2009/103** *Performance Evaluation of Innovative Steel Braced Frames.* T. Y. Yang, Jack P. Moehle, and Božidar Stojadinovic. August 2009.
- PEER 2009/102** *Reinvestigation of Liquefaction and Nonliquefaction Case Histories from the 1976 Tangshan Earthquake.* Robb Eric Moss, Robert E. Kayen, Liyuan Tong, Songyu Liu, Guojun Cai, and Jiaer Wu. August 2009.
- PEER 2009/101** *Report of the First Joint Planning Meeting for the Second Phase of NEES/E-Defense Collaborative Research on Earthquake Engineering.* Stephen A. Mahin et al. July 2009.
- PEER 2008/104** *Experimental and Analytical Study of the Seismic Performance of Retaining Structures.* Linda Al Atik and Nicholas Sitar. January 2009.
- PEER 2008/103** *Experimental and Computational Evaluation of Current and Innovative In-Span Hinge Details in Reinforced Concrete Box-Girder Bridges. Part 1: Experimental Findings and Pre-Test Analysis.* Matias A. Hube and Khalid M. Mosalam. January 2009.
- PEER 2008/102** *Modeling of Unreinforced Masonry Infill Walls Considering In-Plane and Out-of-Plane Interaction.* Stephen Kadysiewski and Khalid M. Mosalam. January 2009.
- PEER 2008/101** *Seismic Performance Objectives for Tall Buildings.* William T. Holmes, Charles Kircher, William Petak, and Nabih Youssef. August 2008.
- PEER 2007/101** *Generalized Hybrid Simulation Framework for Structural Systems Subjected to Seismic Loading.* Tarek Elkhoraibi and Khalid M. Mosalam. July 2007.
- PEER 2007/100** *Seismic Evaluation of Reinforced Concrete Buildings Including Effects of Masonry Infill Walls.* Alidad Hashemi and Khalid M. Mosalam. July 2007.

The Pacific Earthquake Engineering Research Center (PEER) is a multi-institutional research and education center with headquarters at the University of California, Berkeley. Investigators from over 20 universities, several consulting companies, and researchers at various state and federal government agencies contribute to research programs focused on performance-based earthquake engineering.

These research programs aim to identify and reduce the risks from major earthquakes to life safety and to the economy by including research in a wide variety of disciplines including structural and geotechnical engineering, geology/seismology, lifelines, transportation, architecture, economics, risk management, and public policy.

PEER is supported by federal, state, local, and regional agencies, together with industry partners.



PEER Core Institutions:
University of California, Berkeley (Lead Institution)
California Institute of Technology
Oregon State University
Stanford University
University of California, Davis
University of California, Irvine
University of California, Los Angeles
University of California, San Diego
University of Southern California
University of Washington

PEER reports can be ordered at http://peer.berkeley.edu/publications/peer_reports.html or by contacting

Pacific Earthquake Engineering Research Center
University of California, Berkeley
325 Davis Hall, mail code 1792
Berkeley, CA 94720-1792
Tel: 510-642-3437
Fax: 510-642-1655
Email: peer_editor@berkeley.edu

ISSN 1547-0587X